

CHARLES UNIVERSITY
FACULTY OF MATHEMATICS AND PHYSICS

DOCTORAL THESIS

2024

YADU RAM PANTHI

Charles University

Faculty of Mathematics and Physics

DOCTORAL THESIS

2024

Yadu Ram Panthi



**FACULTY
OF MATHEMATICS
AND PHYSICS**
Charles University

DOCTORAL THESIS

Yadu Ram Panthi

**Transient optical and electrical phenomena in organic
semiconductors: Insights into fundamental photophysics,
resistive switching, and emulation of synaptic plasticity**

Institute of Macromolecular Chemistry, CAS

Department of Polymers for Electronics and Photonics

Supervisor of the doctoral thesis: RNDr. Jiří Pflieger, CSc.

Study programme: Biophysics, chemical and
Macromolecular Physics

Prague 2024

I declare that I carried out this doctoral thesis independently, and only with the cited sources, literature, and other professional sources.

I understand that my work relates to the rights and obligations under the Act No. 121/2000 Coll., the Copyright Act, as amended, in particular the fact that the Charles University has the right to conclude a license agreement on the use of this work as a school work pursuant to Section 60 paragraph 1 of the Copyright Act.

In date.....

.....

Author's signature

"मेरो प्रिय परिवार, विशेष गरी मेरो आमाबुबा, जसको माया र समर्थनले यो सम्भव बनायो... "

Acknowledgements

I am profoundly grateful to everyone who has supported me in the completion of my PhD studies and this thesis. This journey has been extraordinary, and I am very thankful for the assistance and encouragement I have received.

At the outset, I would like to express my deepest gratitude to my supervisor, Dr. Jiri Pflieger. His exceptional mentorship, expertise, and consistent support have been indispensable throughout my entire PhD journey. His insightful guidance and encouragement have been instrumental in shaping this research and motivating me to strive for excellence.

Furthermore, I extend my sincere appreciation to Dr. Tuhin Khan, Dr. David Rais, Dr. Bartosz Paruzel, Dr. Francesco Piana, Dr. Udit Acharya, Ambika Pandey, Muhammed Arshad Thottappali, and other seniors/ peers both within and outside my department/institute for their guidance and experimental assistance. Administrative support from Mgr. Dagmar Zádřapová and the Euraxess team were of immense value.

I am immensely grateful to the Institute of Macromolecular Chemistry, CAS, and the Faculty of Mathematics and Physics, Charles University for the academic environment and resources essential for conducting this research. I also appreciate the organizers/ management committee of the UNESCO/IUPAC Postgraduate Course for considering my participation, which served as a crucial bridge for my doctoral studies and other participants who were very good friends of mine. Moreover, I extend my appreciation to my teachers at Dadra Primary School, Deepak Secondary School, Tri-Chandra, and Amrit campus, Tribhuvan University, who have shaped my academic journey from childhood.

Last but certainly not least, I want to extend my heartfelt appreciation to my parents, Chiranjivee Panthi and Durpata Panthi, and all family members. Their boundless love, unwavering faith in my abilities, and consistent encouragement have been the driving force behind my academic endeavors. Their sacrifices and understanding in my life are immeasurable. Moreover, I am extremely grateful for the support and encouragement provided by my beloved partner, Ambika Pandey, who always stayed beside me and encouraged me to overcome challenges.

I also thank the members of my communities, volunteering organizations I have been part of, and all my supportive friends. I express my sincere thanks to everyone who has contributed to my research activities and this thesis.

Title: Transient Optical and Electrical Phenomena in Organic Semiconductors: Insights into Fundamental Photophysics, Resistive Switching, and Emulation of Synaptic Plasticity

Author: Yadu Ram Panthi

Department / Institute: Institute of Macromolecular Chemistry, CAS

Supervisor of the doctoral thesis: RNDr. Jiří Pflieger, CSc., Department of polymer for electronics and photonics, Institute of Macromolecular Chemistry, CAS

Abstract: The growing demand for flexible and cost-effective printable optoelectronic devices can be fulfilled by employing organic semiconductors, comprising either polymers or low molecular weight organic molecules with π -Conjugated electron system. This thesis is focused on the experimental study of the photophysical and charge-transport properties of these materials, in particular, phenomena related to a transient state after photoexcitation or charge transfer, with the aim to understand the underlying processes important for their functionality in various devices in organic electronics, particularly in field effect transistors (OFETs) and memristors, and to optimize their performance. We also demonstrate the potential of exciton management in organic semiconductors that can be exploited in organic photovoltaics.

Using transient optical absorption spectroscopy, we show that thiophene-diketopyrrolopyrrole (TDPP) derivatives exhibit structure-dependent excited state evolution leading to an effective generation of triplets, possibly through singlet fission, and the impact of thermal effects in pump-probe laser spectroscopy measurements on obtained data. Additionally, we found that TDPP-based polymer mixed with perylene, or polymethacrylamide with carbazole side groups are capable of exhibiting electronic memory and synapse-mimicking functionalities. Furthermore, the impact of mobile electric dipoles present in polymer dielectrics on hysteresis in current-voltage characteristics of OFETs has been elucidated, with the possibility of controlling these effects by crosslinking or surface passivation.

Keywords: Organic semiconductors, π -conjugated molecules, exciton management, charge transport, OFET, memristor

Název práce: Transientní optické a elektrické jevy v organických polovodičích: fotofyzikální procesy, odporové spínání a emulace synaptické plasticity

Author: Yadu Ram Panthi

Katedra/Ústav: Oddělení polymerů pro elektroniku a fotoniku, Ústav makromolekulární chemie, AV ČR

Vedoucí doktorské práce: RNDr. Jiří Pflieger, CSc., Ústav makromolekulární chemie, AV ČR

Abstract: Rostoucí potřeba flexibilních a cenově efektivních tisknutelných optoelektronických zařízení vede k vývoji nových organických polovodičů, které zahrnují především polymery a nízkomolekulární organické látky s π -konjugovaným elektronovým systémem. Tato práce je zaměřena na experimentální studium fotofyzikálních a elektronových transportních vlastností těchto materiálů, zejména na jevy spojené s transientními stavy po fotoexcitaci organického polovodiče nebo přenosu náboje. Cílem je porozumět základním procesům v těchto látkách, které jsou důležité pro jejich funkčnost v různých elektronických zařízeních v organické elektronice, zejména v organických tranzistorech řízeným elektrickým polem (OFET) a memristorech, a optimalizovat jejich vlastnosti. Dále je práce věnována fotofyzikálním procesům, které v organických polovodičích vedou k transformaci excitonů. Tyto procesy, zejména proces štěpení singletních excitonů na excitony tripletní, lze využít v organických fotovoltaických člancích.

Pomocí transientní optické absorpční spektroskopie jsme ukázali, že thiophenové deriváty diketopyrrolopyrrolu (TDPP) vykazují efektivní transformaci singletních excitovaných stavů na tripletní, pravděpodobně mechanismem prostřednictvím singletového štěpení, které je však silně závislé na vzájemném uspořádání molekul a tím na struktuře organické látky v pevné fázi. Ukázali jsme též, jak výsledky transientní optické absorpční spektroskopie mohou být ovlivněny tepelnými efekty. Zjistili jsme, že vrstvy polymeru na bázi TDPP smíchaného s deriváty perylenu a polymethakrylamid s karbazolovými postranními skupinami jsou vykazují změny odporu v závislosti na prošlém náboji. Tyto vlastnosti, typické pro memristor, umožnily napodobit synaptickou plasticitu typickou pro biologické neuronové synapse. Objasnili jsme též vliv mobilních dipólů přítomných v polymerním dielektriku na hysterezi volt-ampérových charakteristik tranzistorů OFET, přičemž byla ukázána možnost ovlivnění těchto efektů zesíťováním polymeru nebo povrchovou pasivací.

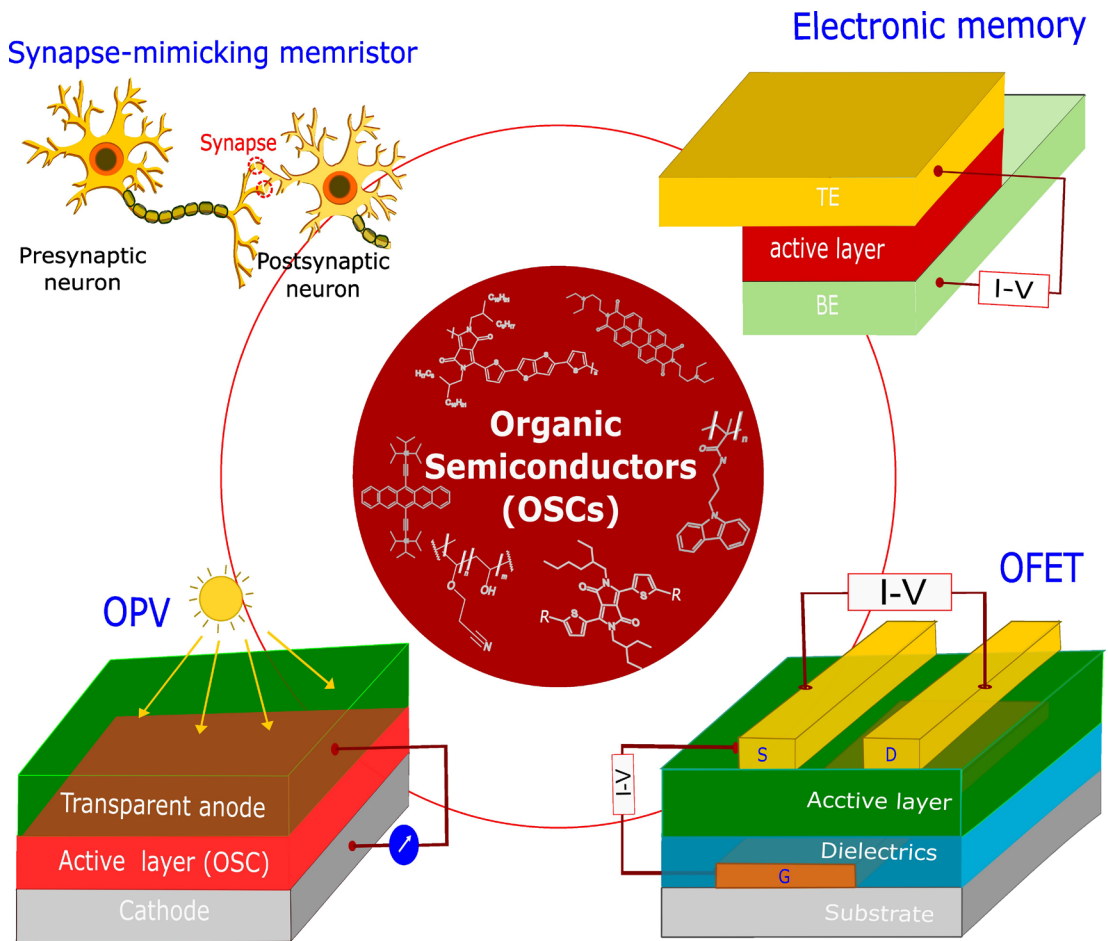
Klíčová slova: Organické polovodiče, π -konjugované molekuly, exciton, transport náboje, OFET, memristor

Content

1. Introduction.....	1
1.1 Current state of the art	4
1.2 Optoelectronic devices: charge generation and transport.....	6
1.2.1 Organic semiconductors (OSCs).....	6
1.2.2 Free charge carrier generation in OSCs	8
1.2.3 Charge transport (CT)	11
1.3 Photophysics in OSCs	15
1.3.1 Excited-state transitions	16
1.3.2 Relaxation processes: radiative vs. non-radiative	17
1.3.3 Photon conversion.....	18
1.4 Dipolar relaxations in macromolecular systems.....	19
1.5 Operation mechanisms of electronic devices under study.....	22
1.5.1 Memristor.....	22
1.5.2 Organic field-effect transistors (OFETs).....	31
2. Materials and Methods.....	33
2.1 Materials.....	34
2.1.1 π -Conjugated small molecules	34
2.1.2 Semiconducting polymers	35
2.1.3 Polymer dielectrics, crosslinkers and passivators	36
2.2 Device preparation	37
2.2.1 Preparation of active layers	37
2.2.2 Device fabrication	39
2.2.3 Device characterization.....	41
3. Results and Discussion.....	48
3.1 Photophysics of TDPP derivatives: Insights into ultrafast processes.....	49
3.1.1 Overview of the study	50
3.1.2 Results and discussion.....	51
3.1.3 Summary	55
3.2 Organic memristors: Electronic memory and emulation of synaptic plasticity	56
3.2.1 Overview of the study	57
3.2.2 Results and discussion.....	57
3.2.3 Summary	73
3.3 Role of dipolar polarization and interface optimization on performance of OFETs.....	75
3.3.1 Overview of the study	76

3.3.2 Results and discussion.....	77
3.3.3 Summary	81
4. Conclusions.....	82
Bibliography	83
List of Abbreviations	96
List of Figures	98
List of contributions at the international conferences.....	101
Attachments.....	103

1. Introduction



Organic semiconductors (OSCs) are primarily derivatives of unsaturated hydrocarbons, in which the π -conjugated electronic system makes their band gap narrower and valence electrons more delocalized. The combination of their semiconducting nature with the chemical and mechanical properties of plastics makes them suitable for flexible optoelectronics.[1,2] The discovery of electrical conductivity in polymers, previously considered as insulators, marked a groundbreaking development that established a new research field. In 2000, recognizing their work on conjugated polymers and the enhanced conductivity of these polymers achieved through doping, Alan J. Heeger, Alan G. McDiarmid, and Hideki Shirakawa were awarded the Nobel Prize in Chemistry.[3] This breakthrough raised the research and commercial interest in this field, leading to applications of conjugated OSCs in several technologies, like organic light-emitting diodes (OLEDs),[3,4] displays,[5,6] organic photovoltaics (OPVs),[7] organic field effect transistors (OFETs),[8] batteries, supercapacitors, and sensors. In addition to these traditional electronic devices, the research moved recently forward also to novel perspectives, for example, organic memory devices and memristive systems.[9–14]

The primary target of organic electronics is not to replace silicon-based technologies, known for superior operational speed and durability. It should be focused more on low-cost, scalable, and flexible applications like large-area displays or energy harvesting and storage. The scalability, achieved through reduced device thickness and cost-effective roll-to-roll printing, is a primary concern for these semiconductors. Although some thin film silicon-based technologies also recently occurred, using classical inorganic semiconductors (ISCs) technologies for preparing such devices is nearly impossible. The commercial progress in this field is evident through the production of smart electronics such as smartphones, or ultra-high flexible OLED displays (Fig. 1.1A-B), including LG's 42-inch flexible display and 88-inch or larger 8 K TV displays available in the 2023 market, featuring wider viewing angles and exceptional contrast levels.[6] Chan Il Park et al.,[15] introduced a fundamental matrix design even for a 77-inch OLED display. Additionally, advanced devices such as thin notebooks, e-papers, digital cameras, and roofs covered with OPV flexible panels have garnered significant consumer attention.[2] These advancements demonstrate the increasing viability of OSCs in many practical applications. While it took long decades of research and development, and substantial investments to bring

OSCs to the market, challenges for scientists and industry still persist, like their chemical and structural stability, particularly under high current densities or UV illumination, at elevated temperatures, or in achieving reproducible parameters.

The field of OSCs includes a diverse range of materials, broadly classified as small molecules or oligomers, typically processed through sublimation in a vacuum, and polymers, usually processed using wet chemical techniques.[19] Envisioned as a cost-effective alternative to their inorganic counterparts, π -conjugated OSCs, characterized by a sequence of alternating single and double bonds, facilitating electron delocalization, are extensively studied for optoelectronic applications. These materials, including molecular crystals, disordered molecular materials, and conjugated polymers, offer opportunities to tailor the structural-property relationship to meet the electrical and optical requirements of the device.[1,20,21] Over six

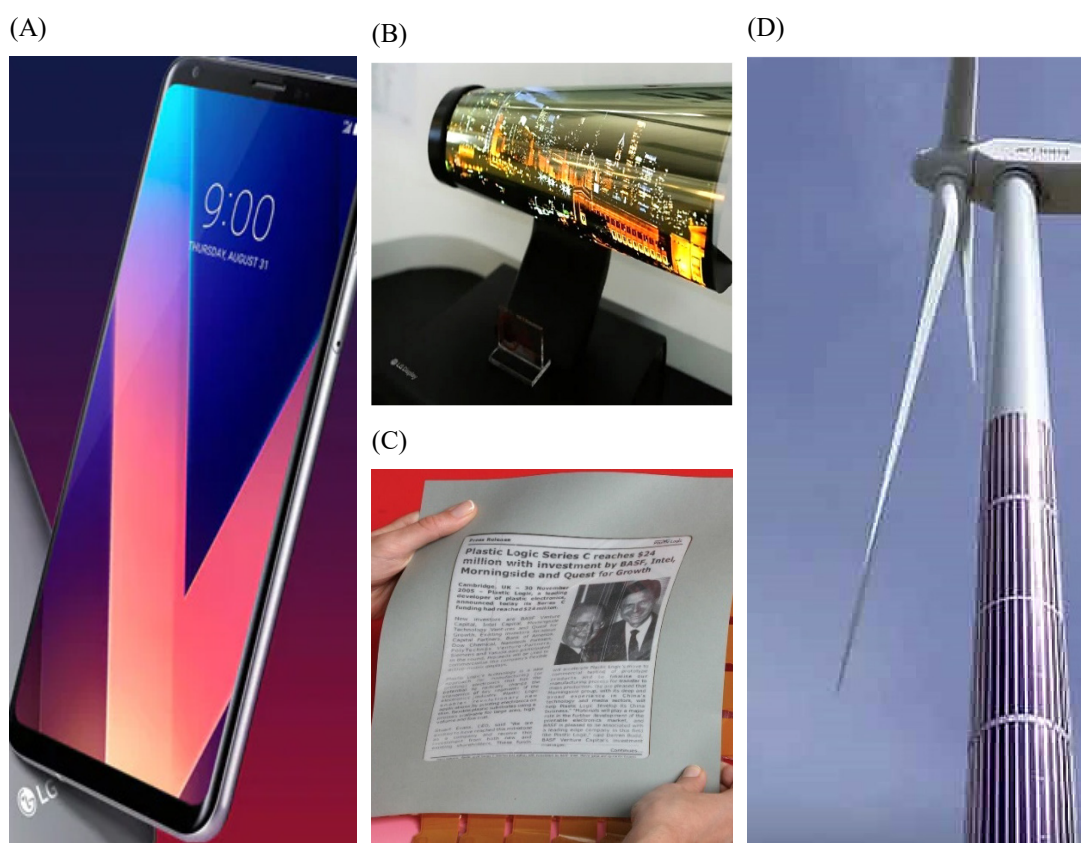


Figure 1.1: Photographs of A) LG's smartphone,[6] B) 18-inch rollable OLED display,[16] C) flexible electrophoretic display using OFETs backplates, fabricated by a company Plastic Logic,[17] and D) rollable OPVs on a wind turbine tower to enhance efficiency.[18]

decades, the field of organic optoelectronics has witnessed the synthesis of new and optimized materials and devices with unipolar or ambipolar charge transport (CT) properties and tuned absorption and emission spectra.[19,22–25]

This thesis delves into the detailed study of electronic processes in organic semiconductors with a focus on transient electrical and optical phenomena. The choice of a broad area of materials, including small molecules, polymers, and their composites, and their study in the context of different device structures and characterization techniques, extends effort towards potential commercialization. Within the scope of this thesis, particular emphasis is placed on phenomena related to solar cells, memristors, and OFETs. In the introduction, we first provide an overview of the main theoretical background related to the underlying phenomena.

1.1 Current state of the art

The origin of OSCs traces back to the 1950s, pioneered by H. Inokuchi and his coworkers who discovered organic semiconductors.[26–28] Despite this early start, it took another 6 decades for these materials to become commercially viable, eventually reaching a market size of \$81.5 billion in 2022, with a projected 20 % growth by 2032.[29] This transformation from inorganic to organic semiconductor technology has significantly impacted various aspects of daily life, including OLEDs, smartphones, solar cells, digital radio-frequency identification (RFID), and e-paper, with a clear movement towards possible exploitation for artificial intelligence (AI) systems. In-depth studies of the electronic properties of OSCs continue in parallel with their commercialization.

OPV's study began in the 1950s, initially exploring organic dyes and later polymers like poly(sulfur nitride) and polyacetylene in the 1980s.[30] The first functional OPVs and OLEDs were reported in 1986 and 1987, respectively, by CW Tang and SV Slyke at Eastman Kodak, laying milestones for OSC. It initiated intensive research showing good perspectives for commercialization.[3] The 2000's Nobel Prize in conducting polymers[3] further accelerated research and device engineering, leading to scalable and flexible electronics using polymeric materials. Various electrically conducting polymers, such as polythiophene, polyphenylene sulfide, and polypyrrole, were identified, fostering material innovations post-2000.[20,31,32]

Despite these advancements, successful commercialization took nearly half a century from the first experiments with organic semiconductors to materialize this research.

Despite technological limitations such as lower efficiency and durability, significant research progress in OPVs brought their efficiency already to 19.31 % as of 2023 (Fig. 1.2B). This efficiency is close to that of polycrystalline silicon solar cells or almost double compared to amorphous silicon photovoltaics.[17,33]. The study of the excited state dynamics using ultrafast laser systems is crucial for understanding fundamental processes in photovoltaics cells from light absorption to the generation of electricity. The development of femtosecond (fs) time-scale light pulses enabled the probing of ultrafast excited-state dynamics in real-time contributing to design of efficient solar cells.

(A)



(B)

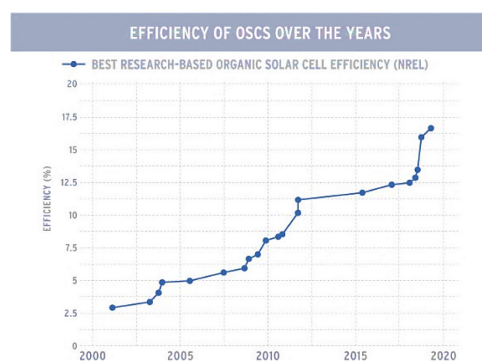


Figure 1.2: A) A sample of thin film solar cells and B) the trend of increase in OSC efficiency with the development of non-fullerene acceptors.[17]

Besides photovoltaics, other electronic components, mainly OLEDs, OFETs, and sensors, came into the focus of organic electronics, too. Recently, organic memristors have been developed, with hysteresis in their non-linear current-voltage characteristics and multi-state conductivity, that can be used in memory devices. [34,35] Though their concept emerged already in the 1960s, significant attention was drawn once its theoretical background was established by Chua in 1971, and the first working prototype was realization at HP Labs in 2008.[36] Memory effects in polymer thin films were reported first on PVK in 1976,[37] followed by novel materials like MoS₂,[38,39] other polymers,[40,41] and their composites,[42] and used for resistive switching, non-volatile memory, and neuronal emulation. Although the incorporation of memristors in various electronic devices like smartphones was projected by the

journal IEEE Spectrum for 2024,[43] challenges like reproducibility and volatility hinder their massive commercialization. Nevertheless, the production pathway toward 16 GB storage capacity has been already demonstrated.[44] The research progress in materials, switching mechanisms, and their integration into electronic circuits is sparking significant interest in industrial production.[45–47] The hybrid production using organic-inorganic frameworks followed by its standalone market can upscale neuromorphic computing and machine learning through the operation of neural networks, a technology in a post-CMOS era of computing.[48–50]

OFETs have been under study since the early 1980s, with marked advancements in polymeric FETs in the 1990s.[51] The first polymer OFET prototype was made with polythiophene by A. Tsunara et al. in 1986, reaching charge carrier mobility of $\sim 10^{-5} \text{ cm}^2 \text{ V}^{-1} \text{ S}^{-1}$. [52] A significant milestone was achieved in 2012 when an 8-bit microprocessor containing 3000 OFETs was printed on a flexible plastic substrate, moving OFETs from laboratory curiosity to a commercially viable technology.[53] In the last decade, significant improvement of the charge carrier mobility allowed their extended use in electronic chips.

As OSC-based technology integrates into the technological landscape, a comprehensive exploration of its working principles becomes imperative. Improvements in lifetime, reproducibility, and optimization of operation parameters are necessary. A profound understanding of intrinsic CT mechanisms, including factors like energetic disorders and polarization effects, is important to address these challenges.

1.2 Optoelectronic devices: charge generation and transport

1.2.1 Organic semiconductors (OSCs)

In OSCs, weak van der Waals forces govern molecular bonding, resulting in electron localization on individual molecules.[54] The binding energies in OSCs are approximately 8 times lower ($< 10 \text{ kcal mol}^{-1}$) than in crystalline Si (c-Si), leading to considerable differences in mechanical and optoelectronic properties.[55] In hydrocarbons OSCs, molecular orbitals form through a linear combination of atomic orbitals, typically after sp^2 hybridization.[56] The mutually interacting remaining p_z orbitals are responsible for electron-delocalization in a conjugated system (Fig. 1.3A). Driven by Pauli exclusion principle, molecular orbitals are formed by the mutual

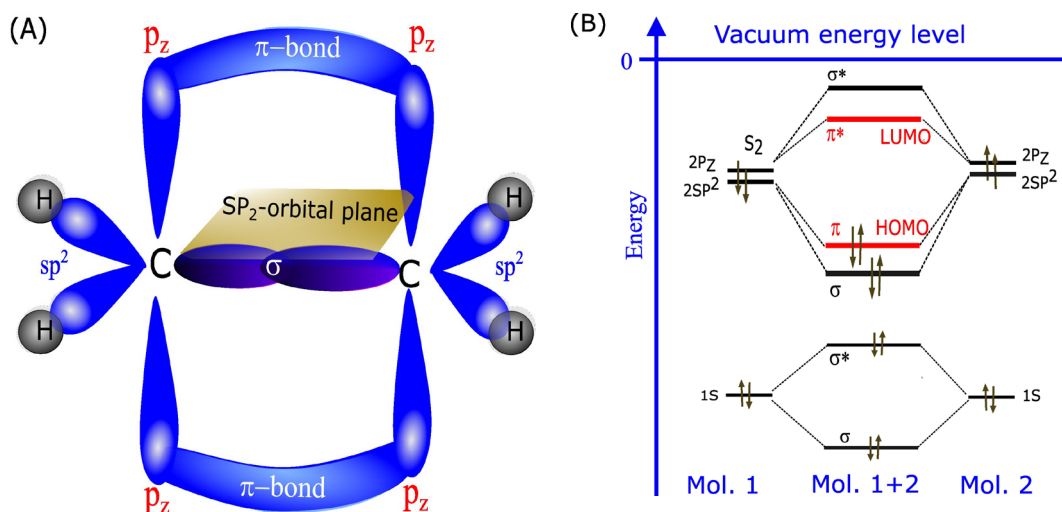


Figure 1.3: A) Illustration of bond formation in an ethylene molecule depicting the combination of atomic orbitals (σ - and π - bonds), and B) transformation of atomic orbitals into molecular orbitals, showing the band-gap.[56]

displacement of energy levels of atomic orbitals into two different energy values, above and below the original position (Fig. 1.3B). Electrons reside in a lower molecular orbital (bonding orbital) providing stability. With additional energy, electrons can be excited into higher energy levels (antibonding orbitals), such as the highest occupied molecular orbital (HOMO) and lowest unoccupied molecular orbital (LUMO) form frontier molecular orbitals separated by energy bandgap, E_g .

As depicted in Fig. 1.3A, the head-to-head overlap of sp^2 hybridized orbitals create strong covalent bonds (σ -bonds), whereas the side-by-side overlap of p_z - orbitals form weaker π -bond orbitals, which are perpendicular to the sp^2 orbital plane. The sequence of alternating σ and $\sigma + \pi$ - bonds facilitates electrons delocalization within a molecule or molecular segment via resonance forming a π -conjugated system.[57] This helps to reduce the bandgap and enables π - π interactions between the molecules causing improved molecular stacking in the solid-state.

Further narrowing of the bandgap can be achieved in organic molecules containing alternating donor (D)-acceptor (A) groups. They feature alternating sequences of electron-rich and electron-deficient moieties that help to extend the electron delocalization via the reorganization of individual energy levels (Fig. 1.4A, B).[58] Varying sequences of D-A units can also alter the HOMO/LUMO energy level, and allow thus tailoring of either hole or electron-transporting material. (Fig. 1.4C).[59] Such systems with different light-absorbing chromophores and

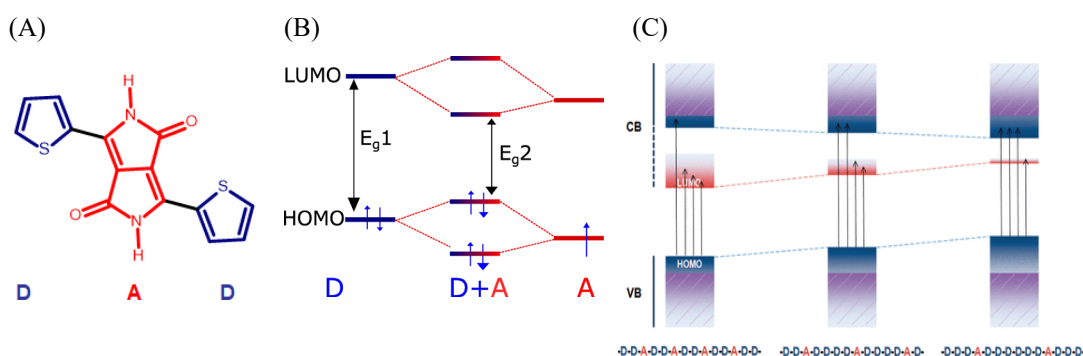


Figure 1.4: A) Chemical structure of bis (thiophene) diketopyrrolopyrrole (TDPP) indicating a donor (D) and an acceptor (A) moieties by blue and red color, respectively, and B) schematic representation of bandgap lowering in a π -conjugated D-A system via the interaction of corresponding molecular orbitals.[58], C) schematic representation of bandgap reduction by lowering/ broadening of LUMO by increasing sequence of D-A units, creating an extensive array of π -orbitals and electron delocalization along the backbone.[57]

multiple absorption/emission bands provide suitable applications for photovoltaic and electrochromic devices.[57,60] π -Conjugated small molecules, often form ordered structures or crystalline domains with reduced static disorder, facilitating good intermolecular charge transport. However, their thin film preparation by solution processing is often challenging due to limited solubility. Side-chain alkylation might solve the problem in some extent but it can change the electronic properties of the molecule, too. Highly homogeneous uniform layers of low-molecular-weight materials can be prepared through physical vapor deposition (PVD). However, thus obtained thin films might be still amorphous or semi-crystalline/polycrystalline bringing more pronounced energy disorder.[40,61]

1.2.2 Free charge carrier generation in OSCs

At room temperature, the concentration of free charge carriers in OSCs at thermal equilibrium is usually very low. In their undoped state, OSCs behave as insulators unless charge carriers are injected either from electrodes or generated within the bulk through optical/thermal excitation or by doping.[24]

1.2.2.1 Photogenerated carriers

Energy harvesting from sunlight relies on the efficiency of free charge carriers photogeneration. Compared to silicon, OSCs possess a higher extinction coefficient, essential for efficient light absorption. However, direct photogeneration of charge carriers in organic compounds faces obstacles as they tend to form electrostatically bound excitons (electron-hole pair) due to lower dielectric constants, typically ranging between 3 and 5. To overcome this hurdle, a bilayer system or heterojunction of donor and acceptor molecules has been established. Excitons, formed at the point of generation, must reach the junction within their lifetime. Upon reaching the junction the excitons can dissociate to individual free carriers, electrons, and holes, subsequently collected at respective electrodes. In OPVs, transport of photo-induced exciton is diffusion controlled, with mobility described as $\mu = eD/kT$, where D is the diffusion constant, k is the Boltzmann constant, and T is the temperature. Increasing the diffusion coefficient, D , or exciton lifetime is crucial to prevent the recombination before charge separation at the donor-acceptor interface.[19]

Prolonged exciton lifetime is desired highlighting the importance of materials capable of triplet exciton formation by an efficient intersystem crossing (ISC). Therefore, a deep understanding of light-matter interactions is vital for optimizing material properties in solar energy conversion.

1.2.2.2 Injection from electrodes

For injection-operated electronic devices, the injection efficiency is primarily governed by the contact resistance, affected mainly by the Schottky barrier (ϕ_B), which depends on the energy difference between the electrode work function and the energy

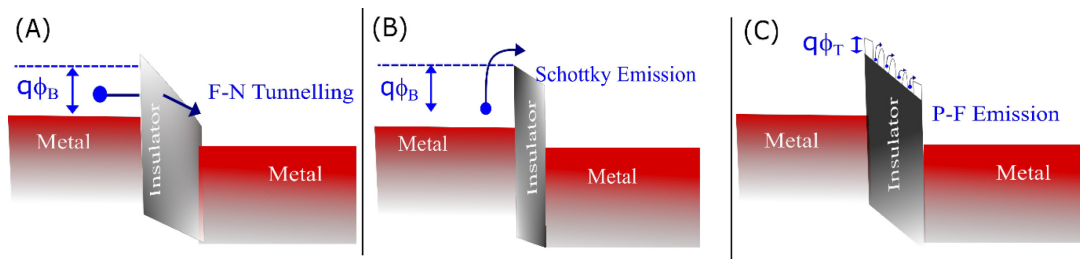


Figure 1.5: Schematic energy band diagram illustrating charge injection via A) F-N tunneling, B) R- S thermionic emission, and C) P-F emission in MIM structures.[62]

of HOMO or LUMO level of the organic layer.[4] This barrier can be manipulated by altering the interface via physisorption or chemisorption.[63] A low barrier (< 0.3 eV) results in an Ohmic contact, while a barrier exceeding this value limits the device's performance. Nevertheless, even high energy can be overcome via a field-enhanced thermionic emission or quantum-mechanical tunneling.[64,65] Among them, Fowler-Nordheim (F-N) tunneling occurs when the electric field is strong enough to allow tunneling of electrons through the energy barrier, while Richardson-Schottky (R-S) thermionic injection involves injecting thermally excited charge carriers from the Fermi level of an electrode to the transporting energy level of OSC (Fig. 1.5B). On the other hand, Poole-Frenkel (P-F) emission (Fig. 1.5C) is a trap-assisted injection process, observed in amorphous or polycrystalline OSCs where trapped charges get excited into the transporting energy level by the applied field, reducing the coulombic potential barrier.[66–68] This process elevates electrons from the Fermi level of an electrode to the DOS tail states (Fig. 1.6). Once carriers are raised/injected, they undergo polaronic hopping, i.e. a movement by thermally activated jumps between different sites, similar to diffusive random walk.[19,68,69]

1.2.2.3 Carrier generation via doping

Dopants, acting as guest molecules, broaden the GDOS (Fig. 1.6C). This broadening

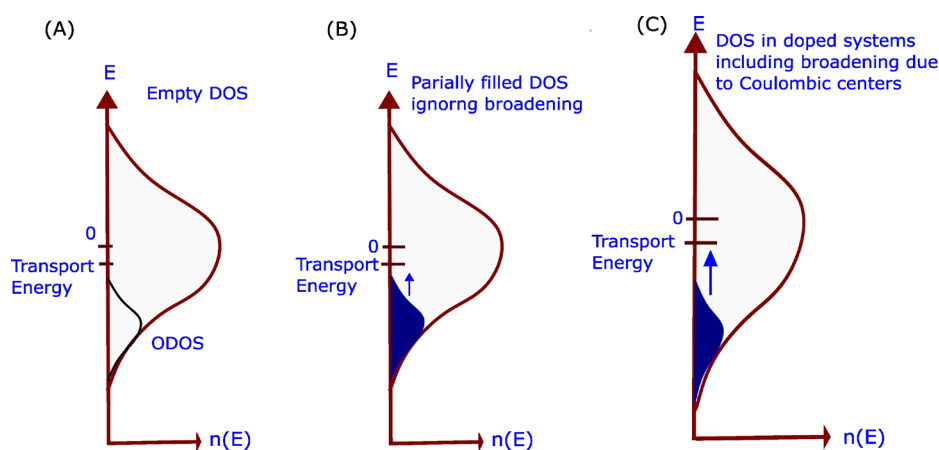


Figure 1.6: Schematic of the effect of DOS filling in the Gaussian distribution of the hopping states A) at low or no carriers at thermal equilibrium, B) in the presence of a space charge obeying F-D statistics, and assuming no alteration to the DOS and C) in the presence of a space charge assuming the broadening of the DOS due to the presence of counter ions.[69]

results from the mismatch of frontier molecular orbitals between guest and host molecules, depending on dopant concentration.[70] Some of the energy levels become localized and function as traps for charge carriers. However, in the case of intentional doping, free carriers can be generated when the energy levels are properly aligned.

In the case of p-type doping, dopant's LUMO aligns with the host's HOMO, producing free holes, while in n-type doping, the dopant's HOMO aligns with the host's LUMO, yielding free electrons (Fig. 1.7). If HOMO/LUMO energy levels lie outside the bandgap of the host, the dopants might act as scattering centers, which may also act as anti-traps by preventing trapping of charge in a localized level located nearby.[67] They are more detrimental in dynamic disorders scenarios. In the host-guest systems, dopant molecules often segregate on grain boundaries in polycrystalline hosts, contributing to energetic disorder and impeding overall transport.[71]

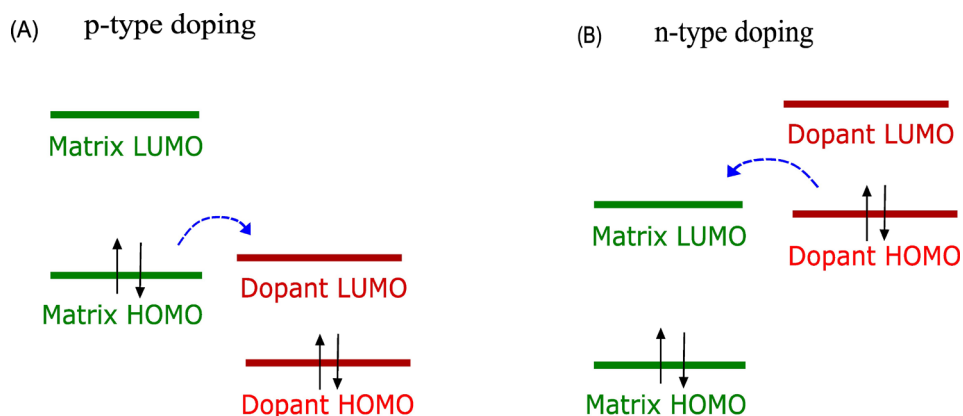


Figure 1.4: Schematics of A) p-type, and B) n-type doping of OSCs.

1.2.3 Charge transport (CT)

Unlike their inorganic counterparts, where charge carrier mobility is governed by band transport through crystal lattices, OSCs exhibit incoherent hopping CT. Weak Van der Waals interactions lead to transport, closely linked to localization within the molecules/crystal lattices,[72] and subjected to static and dynamic disorder, thus lowering the carrier mobility to $\sim 10^{-7} - 10^1 \text{ cm}^2 \text{ V}^{-1} \text{ s}^{-1}$. The interaction of localized charges with molecular vibrations forms the self-localized polarons, and their transport is described by polaronic band theory.[55] In ideally disorder-free crystalline structures, such as single crystals, band-like transport is also observed.[69] However,

diverse structures and various origins of carrier localization lead to numerous diverse theoretical models and make CT analysis in OSCs very challenging.

The conductivity, (σ) of OSC depends on concentration (n) and effective mobility (μ) of free charge carriers, $\sigma = en\mu$. [17] Due to low mobility and low thermal equilibrium concentration of charge carriers, the current in OSC is often controlled by space charge formed of injected charges.

1.2.3.1 Band-like transport

Band-like transport similar to the inorganic materials was observed in OSCs in single molecular crystals with only limited structural disorder. [73] Despite observing band-like transport, the mean free path of charge carriers remains comparable to intermolecular spacing, indicating only limited delocalization. [70] Due to weak intermolecular interactions organic solids are never entirely free of disorder. Band-like transport in OSCs is often explained by temperature-dependent mobility with an inverse relationship $\mu \sim T^{-\alpha}$. [74]

1.2.3.2 Hopping transport

The CT in OSCs operates at a molecular level, involving both intra- and intermolecular mechanisms. Intramolecular CT occurs through π -electrons within a single molecule, while intermolecular transport arises when two molecules come into close contact, facilitating hopping through the transfer integral of interacting molecular orbitals. [75] This hopping, non-coherent in nature, limits the charge transport, [66] that proceeds through localized states distributed in space and energy. The DOS is mostly modeled by a Gaussian Density-of-States (GDOS) distribution with an energetic width σ (Fig. 1.6). At room temperature, charge carriers relax below the center of GDOS at energy $E_{tr} = \frac{\sigma^2}{kT}$, known as ‘activation energy’. Upon application of an electric field or heat, carriers reach new quasi-equilibrium characterized with the transport energy level, E_{tr} and are capable of transportation. [76] In doped systems, DOS broadening occurs (Fig. 1.6C) due to the presence of ionized additives, resulting in lower activation energy and increased charge carrier mobility. [69] The polaronic hopping between localized states occurs when carriers superimpose with associated disorders. The superimposition arises from molecular reorganization due to electron-phonon

coupling, slowing down the transport rate. Miller and Abrahams[77] proposed a Gaussian Disorder Model (GDM) to calculate hopping rates v_{ij} between sites i and j for variable-range hopping in disordered OSCs, expressing the transfer rate as function of the distance r_{ij} between hopping sites and their energy levels E_i and E_j as:

$$v_{ij} = v_0 \exp(-2\gamma r_{ij}) \times \exp\left(-\left(\frac{E_i - E_j}{kT}\right)\right) \quad (1.1)$$

with γ is the inverse localization radius related to the electronic coupling between adjacent sites, and v_0 is a frequency factor.

1.2.3.3 Space charge-limited (SCL) current

Charge carriers, electrons and holes, injected from a cathode and anode, respectively, move to the counter electrode or recombine within the layer before they reach the counter electrodes.[82] However, if the injection rate between electrodes differs, or the organic material exhibits only unipolar charge transport properties, the current becomes injection-limited, resulting in a polarity-dependent current, controlled by the energy barrier at the interface.[78–81] In organic semiconductors, due to a usually low thermally generated free charge carrier concentration, the current is often space charge-limited.[65,66,76,78,82,83] Spatially nonhomogeneous field alters the current that can be expressed by the Mott-Gurney equation:[70]

$$J = \frac{9}{8} \mu \epsilon \epsilon_0 \frac{F^2}{d} = \frac{9}{8} \mu \epsilon \epsilon_0 \frac{V^2}{d^3} \quad (1.2)$$

The Mott-Gurney law can be derived by solving Poisson's equation, the continuity equation, and Einstein's relation.[84,85] Further modifications to the current occur if the charge carrier mobility, μ is field-dependent, described by P.N. Murgatroyd, introducing an additional exponential factor (Frenkel's field factor) as:

$$J = \frac{9}{8} \mu \epsilon \epsilon_0 \frac{V^2}{d^3} \exp\left(\frac{0.891}{kT} \left(\frac{e^3 V}{\pi \epsilon \epsilon_0 d}\right)^{1/2}\right) \quad (1.3)$$

1.2.1.1. Influence of localized trap states on CT

Trapping of charge carriers occurs in most OSCs. Trapping of charges decreases conductivity but after filling the tail-part of DOS by the space charge (Fig. 1.6), a steep increase in current occurs. In OSCs, the presence of a high concentration of disorders arises from various intrinsic and extrinsic factors. These disorders include dynamic (diagonal) such as thermal fluctuations of site energies due to the electron-phonon

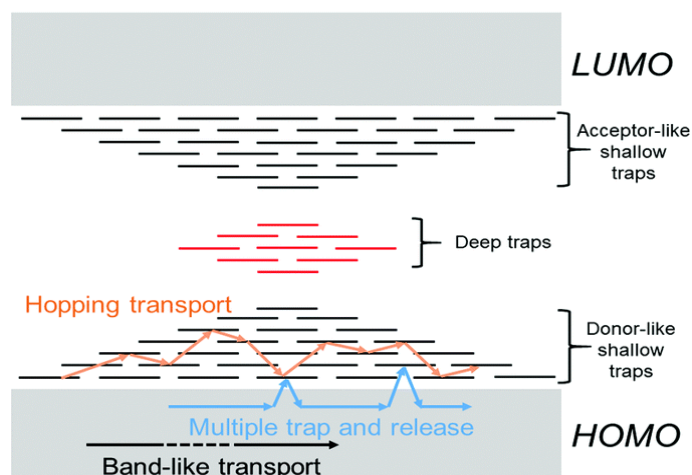


Figure 1.8: Schematic of spatial and energy diagram of an OSC containing localized trap states in the band gap. The trap DOS as shallow traps (black dash) and deep traps (red dash) lies in the band gap, close to the band edges and at center of bandgap, respectively. Blue arrows represent MTR of a charge between transporting level and trap DOS, while orange arrows indicate thermally-activated hopping transport between localized states.[70]

coupling and fluctuations of transfer integrals due to intermolecular interactions, or static (off-diagonal) factors from extrinsic sources, such as chemical impurities from synthetic remnants or chemical degradation, interfacial effects, or randomly oriented dipoles in the system.[70,71] External impurities from dopants, nanoparticles or water, oxygen, or bias stress also contribute to the formation of trap states. Working as defects, trap states strongly influence CT characteristics and have a profound impact on the performance of optoelectronic devices.[70,86]

Shallow trap DOS, located near band edges, require less energy and time for emptying compared to deep traps situated in the center of the bandgap (Fig. 1.8). Various spatial and energetic tools, such as electron force microscopy, scanning tunneling microscopy, thermo-stimulated current measurement, optical-detrapping, or calculation of electronic structures probe the presence and energetic distribution of trap DOS.[70,87] Concentration of traps can be controlled/minimized through careful film/crystal growth or device encapsulation, though complete elimination is not feasible.

When a low electric field is applied, carriers are predominantly trapped. The current density is reduced, altering the Mott and Gurney expression to be trap-controlled:

$$J = \frac{9}{8} \mu \theta \epsilon \epsilon_0 \frac{V^2}{d^3} \quad (1.4)$$

where θ is the proportion of free to total carrier concentration given by:[81]

$$\theta = \frac{n_f}{n_f + n_t} = \frac{N_c}{N_t} \exp\left(\frac{-E_t}{kT}\right) \quad (1.5)$$

here, n_f and n_t are the concentration of free and trapped carriers, respectively. When increasing applied voltage more traps become occupied. When reaching the trap-filled limit voltage, V_{TFL} , an abrupt increase in SCL current occurs is observed. An analysis of the SCL current dependencies on field and temperature can provide insight into trap level distribution in the energy.[12]

1.3 Photophysics in OSCs

Photoexcitation of OSC involves absorption of photon energy, which takes place mostly on a molecular level, followed by relaxation through the manifold of electronic and vibrational energy levels, and release of energy either through the light emission or through non-radiative processes to heat. In a solid state, Förster resonance or Dexter energy transfer can occur, or the excess energy can result in charge transfer, possibly making the free charge for transport. The interplay between various energy decay pathways is crucial for various applications; for example, in OLEDs and fluorescent probes, enhancing luminescence efficiency is vital, while in photovoltaics & photocatalysis, non-radiative processes prevail resulting in charge transfer.[88]

Understanding the physical processes of light absorption and emission is pivotal for optoelectronics. Contrary to the steady-state characterization methods that provide information on optical absorption and emission spectra, or absorption coefficient and fluorescence quantum yield, from which the electronic structure of OSC can be determined, time-resolved methods, like time-correlated single photon counting (TCSPC) and transient optical absorption spectroscopy (TAS), yield closer insight into the processes following photoexcitation. These tools are crucial for studying excited state phenomena such as energy migration, charge separation, photochemistry, isomerism, and intersystem crossing.[89] Upon interaction with electromagnetic radiation, molecules undergo electronic transitions to higher electronic energy states, forming neutral excitons considered as pairs of electrons and holes Coulombically bound together due to strong electrostatic attraction caused by the low dielectric constant of organic materials (~ 3). It makes OSCs different from inorganic

semiconductors like silicon where free charges are generated directly upon photon absorption.[90]

1.3.1 Excited-state transitions

Photophysical processes within a molecule are mostly discussed in the frame of a Jablonski diagram (Fig 1.9).[91] This diagram illustrates the transitions between electronic and vibrational states of a molecule. Upon absorption of photon, a molecule swiftly, within a femtosecond timescale, transitions to a higher electronic and vibrational state. This rapid process, described mostly within the Born-Oppenheimer approximation, is attributed to the significantly lower mass of electrons compared to the nucleus.[92]

After excitation to higher electronic and vibronic states, the molecule undergoes an internal conversion (IC) to the lowest vibronic level (V_0) of the first excited electronic S_1 state within hundreds of femtoseconds to a picosecond timescale, from where it relaxes radiatively by fluorescence or by nonradiative processes. Alternatively, the spin state multiplicity can be changed during the deexcitation process and the state of the molecule can transfer to one of the triplet states (T_n) via intersystem crossing (Fig. 1.9). The latter process, normally of very low probability, may be enhanced by spin-orbital coupling in heavy-atoms containing molecules or

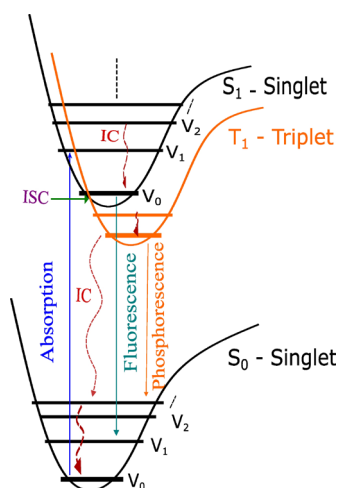


Figure 1.9: Jablonski energy diagram portraying various transitions occurring within a molecule's electronic and vibrational states manifold upon photoexcitation. Solid lines depict radiative transitions, while dashed lines represent non-radiative processes.

charge-transfer complexes that show a metal-to-ligand charge transfer. Triplets can be also generated via bimolecular processes like singlet fission (SF).

In the solid state, the excitation energy can move in the form of a neutral quasiparticle dubbed exciton. Exciton can be localized within a single molecule (Frenkel exciton), or on two adjacent molecules (charge-transfer exciton, or distributed across multiple molecules (Wannier exciton)).[17] In conjugated systems, the transition occurs mainly between π and π^* orbitals, while molecules or chromophores with free (non-bonding) electron pairs, such as carbonyl, nitro, or azo-groups, undergo a transition between n and π^* orbitals with lower transition energy.[90] For σ to σ^* transition to occur, light excitation with higher photon energy is required.

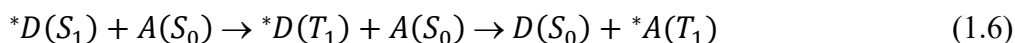
1.3.2 Relaxation processes: radiative vs. non-radiative

Fluorescence emission occurs when the singlet exciton relaxes directly back to its ground electronic state ($S_1 \rightarrow S_0$), emitting radiation with a lifetime of nanoseconds. Compared to absorption spectra, fluorescence emission spectra exhibit a redshift, known as 'Stokes shift' or Franck-Condon displacement.[1] In contrast, phosphorescence emission originates from the first triplet state ($T_1 \rightarrow S_0$), and it is characterized by a longer lifetime of 1 μ s - 10s of seconds. The formation of the triplet exciton involves ISC and spin-flips (Fig. 1.9), but it is less probable in common OSCs due to spin imparity and weak spin-orbit coupling.[93] Another form of phosphorescence emission can occur from dopants or trapping centers.[94] Phosphorescence decay is characterized by a slow rate due to the trapping of electrons to V_0 of excited triplet state, mediated by Russell-Saunders coupling.[17] If the molecule is in the excited triplet state with some surrounding temperature, thermally activated delayed fluorescence (TADF), might occur via reverse ISC into emitting a singlet (S_1) state, important in increasing OLEDs efficiency.[95,96] TADF has been studied in DPP-based molecules for light amplification and efficiency enhancement of EL.[97]

Non-radiative transition involves relaxation from S_1 or T_1 to the ground state through internal conversion, resulting in heat release and referred to as fluorescence quenching. Quenching mechanism is supported through static or dynamic processes, that are influenced by factors like temperature and molecular collisions.[98] Oxygen usually plays a role as a quencher of phosphorescence due to its triplet ground state. Moreover, the formation of physical or chemical dimers, such as in DPP–thiophene

derivatives, is often reported to facilitate this process.[88] Intramolecular and intermolecular energy and charge transfer are particularly important for understanding these photophysical processes.[99] Energy transfer, supported by the Förster or Dexter mechanism takes place in D-A molecular systems ($D^* + A \rightarrow D + A^*$) and has an impact on processes like photosynthesis and photovoltaics that requires generation of long-lived excitons. This bimolecular process is important in the systems where the direct transition from the singlet to triplet excited state is not efficient.[99]

As the absorption coefficient related to the transitions from S_0 to T_1 is very low since the process is spin-forbidden, we need to look for the systems that can constitute triplet formation through ISC or triplet energy transfer (TET). In the TET the energy transits from the donor to the acceptor as an allowed process without changing spin multiplicity. Once the donor is excited to its higher electronic state (singlet), it proceeds from S_1 to T_1 through ISC, within the donor's energy level followed by the TET to the acceptor moiety, as a coupled non-radiative process, bringing the acceptor to its triplet state represented by:



The energy transfer follows thermodynamic and quantum selection rules of spin and energy conservation.

1.3.3 Photon conversion

Photon conversion refers to an alteration in photon energy (wavelength) upon interaction with material. It can be up conversion or down conversion, represented by triplet fusion and singlet fission, respectively. Triplet fusion involves merging two low-energy photons/excitons (triplets) into one singlet, exhibiting the anti-Stoke's shift. In contrast, the down conversion generates two excitons (triplets) from a singlet.

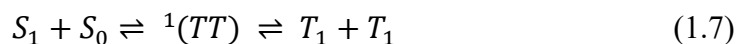
1.3.3.1 Triplet fusion (triplet-triplet annihilation)

Merging two triplets into a singlet is crucial in fluorescent or electroluminescent devices such as OLEDs, converting IR radiation into visible light.[100] At first, the sensitizer absorbs low-energy photons followed by the ISC to triplets, which are then transferred to annihilator by triplet-energy transfer (TET), followed by their fusing and formation of singlet (S_1). From the singlet state the fluorescence emission of higher-energy photons. For the process to be efficient, a sum of two triplets' energy must be

higher or equal to that of a singlet, i.e., $2T_1 \geq S_1$. DPP-based molecules have been studied as annihilators in triplet fusion process favored by their lower exchange energies.[101]

1.3.3.2 Singlet fission (SF)

SF is a photon down-conversion process wherein a singlet exciton excited by a high-energy photon splits spontaneously into two lower-energy triplet excitons. First observed in 1965 in anthracene crystals,[102] SF has brought significant interest in energy transfer processes, important for solar cells, by reducing thermal losses, thus potentially overcoming the Shockley- Queisser limit.[103] Theoretically, this provides the possibility of a formation of doubling the excited state population. After absorption of one photon, one singlet exciton S_1 is directly photogenerated and splits into two triplet excitons T_1 in a process involving two adjacent molecules making thus the efficiency of the process up to 200 %.[104] As an intermediate state, an intermediate correlated triplet pair state $^1(TT)$ is rapidly formed after photoexcitation that later dissociates to two independent triplet excitons. Energetically, the sum of two triplets' energy must be lower or equal to that of the singlet.[105]



The SF rate is significantly influenced by the morphology of the layers, highlighting thus the importance of deposition parameters. Favorable materials for SF include molecular aggregates, covalently-linked dimers, biradicaloids, and aromatic heterocycles like DPP derivatives and anthracene molecules.[102,106,107] For example, Mauck CM. et al., studied the intermolecular packing variation in polycrystalline thin films and its direct effect on singlet fission efficiency on DPP derivatives using different alkyl substitutions without changing the aromatic core, where the efficiency value was ranging between 70-200 %.[106]

1.4 Dipolar relaxations in macromolecular systems

Electrical transient phenomena are influenced by molecular dynamics that can be studied via dipolar relaxation. The dielectric relaxation is commonly elucidated in the frame of the Havriliak-Negami (HN) relaxation that accounts for asymmetry and broadening of the dielectric spectrum:[108]

$$\varepsilon^*(\omega) = \varepsilon'(\omega) - i\varepsilon''(\omega) = \varepsilon_\infty + \frac{\Delta\varepsilon}{[1+(i\omega\tau_{HN})^\alpha]^\beta} \quad (1.8).$$

Here, ω is an angular frequency of applied AC electric field, ε_∞ represents the permittivity at high-frequency limit ($f \rightarrow \infty$), with $\Delta\varepsilon = \varepsilon_0 - \varepsilon_\infty$ denoting the energy dissipation and ε_0 is the low-frequency limit (static) permittivity. τ_{HN} denotes the central relaxation time of the distribution function, α and β are the constants related to the asymmetry and width of the relaxation spectra. The real part of the permittivity, $\varepsilon'(\omega)$, reflects the capacity to store energy, while the imaginary component, $\varepsilon''(\omega)$, accounts for the energy dissipation within the medium.[109] For the experimental data analysis, a reciprocal value of complex permittivity is often plotted, termed as Modulus, $M^*(\omega)$, gives more visible changes in relaxation behavior, akin to mechanical shear and tensile moduli.[110]

The dynamics of localized movements, such as segmental mobility in polymers, are associated with phenomena like glass transition temperature or α -relaxation. Cooperative reorientation of chain segments, influenced by entropic and enthalpic factors, leads to the transitions from glassy to rubbery states.[111] Secondary transitions, like β - and γ -relaxations, involve stretching or rotational mobility of small polar molecular units or atoms. The Normal-Mode (η -) relaxation describes slow chain relaxation in polymers, involving long-range motions of the end-to-end dipole moment vectors that are parallel to the polymer main chain.[110]

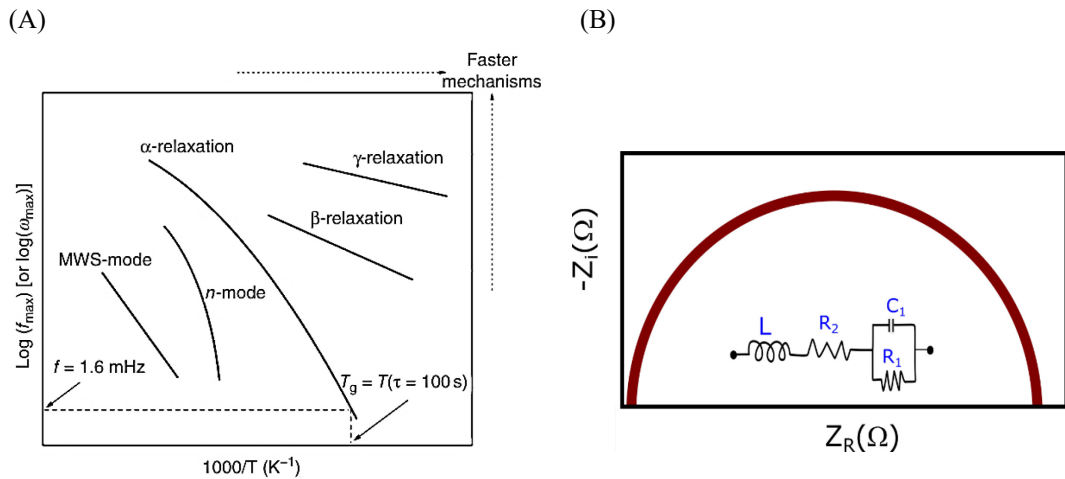


Figure 1.10: A) Typical Arrhenius plots for various relaxation processes in polymer,[110] and B) schematic of Nyquist plot of the complex impedance. R_1 and R_2 indicate parallel and serial resistance, respectively, and L and C_1 represent the inductance and capacity, respectively.

In composite materials, and in conducting composites, Maxwell-Wagner-Sillars relaxation is usually observed at lower frequencies, which occurs in heterogeneous systems due to differences in the electrical conductivity of the composite fractions. The accumulated charges at the interface create a localized electric field, influencing the overall polarization response of the material.

The relaxation time (τ) reflects the interactions between dipoles to their surrounding. Dipoles subjected to stronger hindrances from their surroundings exhibit longer τ , particularly as temperatures rise. Hence, this duration is directly linked to factors such as solvent viscosity in solutions, molecular packing (amorphous or crystalline), and rotational stiffness in solid state. Its temperature dependence is described by an Arrhenius-type equation:

$$\tau(T) = \tau_0 \exp\left(\frac{E_a}{kT}\right) \quad (1.9)$$

Here, τ_0 denotes the pre-exponential factor, which ideally approaches 1 ns, and k is the Boltzmann's constant.[55] The activation energy, E_a , for relaxation is determined from the slope of the Arrhenius plot $\log(\tau)$ vs $\left(\frac{1}{T}\right)$ (Fig. 1.10A). E_a in the range of 100 to 200 kJ mol^{-1} is linked to highly restricted conformational motions, i.e., α -relaxation, whereas a lower E_a suggests other localized motions like β - and γ - relaxations.

For the impedance analysis, a scheme is frequently used consisting of a capacitor, C , resistor, R , and inductor, L , in serial or parallel connection. For a single relaxation:

$$Z(\omega) = R + \frac{1}{j\omega C} \quad (1.10)$$

Nyquist plot is employed as a graphical representation with a plotted real and imaginary part of impedance function, in the x and y axis, respectively, forming a semicircular arc on a complex plane (Fig. 1.10B). For a purely resistive component, only the real part appears, manifested as a point along the real axis. The radius of the semicircle is determined by the product of R and C , where the shape and amplitude of the semicircular arc provide information about the resistance, capacitance, and dielectric properties of the materials.

1.5 Operation mechanisms of electronic devices under study

1.5.1 Memristor

Memristor, a memory resistor, is a two-terminal device that dynamically alters its resistance in response to electrical stimuli, tracking its resistance relative to current or electric charge passing through it previously.[112] Recognized as a fourth fundamental passive circuit component, it links electrical charge (q) to magnetic flux (ϕ). Its capacity to switch between conducting states and retain them makes it as a promising candidate for memory applications. They are current-controlled or voltage-controlled devices, depending on the input source.

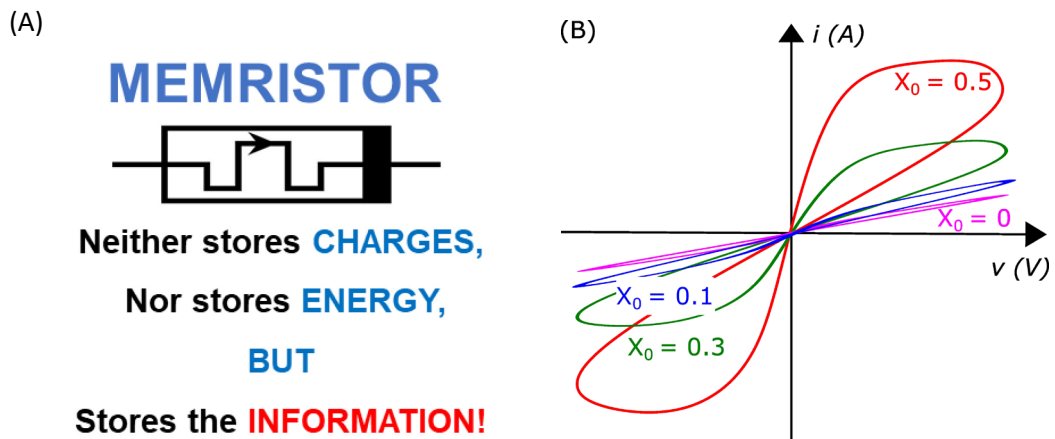


Figure 1.11: A) Schematic of a memristor defining its functionality, B) pinched hysteresis as a device fingerprint with variable $x(t)$ is inversely proportional to frequency f . [113]

Unlike traditional methods relying on charge or energy, this innovative technology utilizes changes in layer conductivity for information storage (Fig. 1.11A). [114] With the co-location of memory and chips, memristors offer in-memory computing with minimal energy consumption. The definition of memristor involves specific criteria, including its characteristic pinched hysteresis loop in a double-valued Lissajous figure of the current-voltage plane [$V(t)$ vs $i(t)$], for all times, t , except when it passes through the origin. [113,115,116] As excitation frequencies rise, the area of hysteresis loops should decrease monotonically, converging to a single-valued function at infinite frequency (Fig. 1.11B).

1.5.1.1 Memristor characteristics

A memristor relates charge ($q(t) = \int_{-\infty}^t i(\tau) d\tau$) to the flux linkage ($\phi(t) = \int_{-\infty}^t v(\tau) d\tau$) through the memristor equation as:[112]

$$M(q(t)) = \frac{v(t)}{i(t)} = \frac{\frac{d\phi(q)}{dt}}{\frac{dq}{dt}} = \frac{d\phi(q)}{dq} \quad (1.11)$$

Here, $M(q(t))$ represents memristance, akin to resistance with unit ohms (Ω), but dependent on the charge passed through it. Eqn. 1.11 elucidates the voltage- or charge-controlled nature of the memristor. If M does not vary, it behaves like a resistor. Despite criticisms regarding memristors' classification as 4th fundamental passive circuit element, their inability to be constructed from a combination of basic circuit elements validates its status.[117]

The first realization of the memristive device was reported by Strukov et al.,[118] at HP Labs, employing a linear ion drift model in a TiO₂-based active layer. According to this model, the layer resistance alters due to a voltage-induced migration of oxygen ions. By reversing the voltage polarity, the device is reset back to the undoped state, resetting the conductivity of the layer to its original value (OFF-state). With the ON-state (full or highly doped device) and OFF-state (fully or highly undoped device), with resistance in each state, R_{ON} and R_{OFF} , respectively (Fig. 1.12), the effective resistance at a given time, t , was calculated considering the state variable, $x(t)$. With the proposed linear drift model and considering the device in OFF-state (i.e., $R_{ON} \ll R_{OFF}$), the effective resistance (memristance) at a given time is:

$$M(q(t)) \frac{v(t)}{i(t)} = R_{OFF} \left(1 - \mu \frac{R_{ON}}{D^2} q(t)\right) \quad (1.12)$$

where μ is the mobility of oxygen ions. This equation satisfies the memristive model

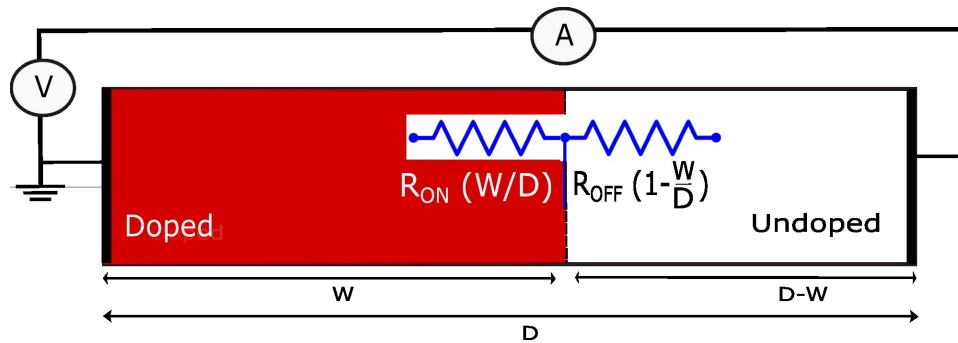


Figure 1.12: Schematics of HP memristor model.[118]

that is based on a linear drift of ions.[116] Additionally, the non-linear model was developed by Joglekar and Wolf [11], considering the boundary condition for non-linear distribution of the electric field inside the memristor, described as:

$$M(q(t)) \frac{v(t)}{i(t)} = R_{OFF} \left(1 - \mu \frac{R_{ON}}{D^2} q(t) f(x) \right) \quad (1.13)$$

$f(x)$ is known as a window function that considers the non-linear model of memristor.

1.5.1.2 Contemporary memory and computing architectures

Contemporary information technology (IT) relies on the digital functionality of integrated circuits (ICs) for data storage or computation, employing resistors, transistors, and capacitors. Electronic memory serves as a fundamental component for storing retrievable digital data within a specific timeframe.[119] This compact unit efficiently interacts with the central processing unit (CPU). These memories are broadly categorized into volatile and non-volatile types, based on their ability to retain data.[120] Volatile memories, such as dynamic random-access memory (DRAM) or static random-access memory (SRAM), lose data when power is turned off. Conversely, non-volatile memories, like write-once read-many times (WORM) or rewritable (flash) memory, retain stored information even without a continuous power supply. WORM memories possess the unique capability of permanently retaining data,

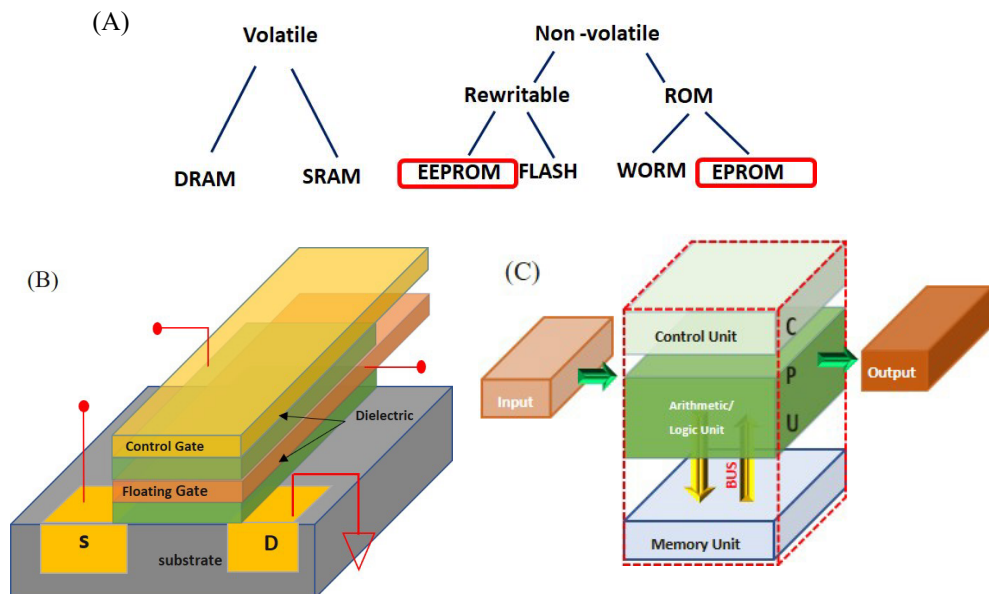


Figure 1.13: Schematics of A) type of electronic memories, B) floating gate MOSFET, and C) Von-Neumann computing architecture.

making them suitable for disposable electronic circuits or archival purposes.[119,120] DRAM, the main computer memory, relies on continuous power or periodic refreshing pulses to maintain data. SRAM, although faster and more reliable is less scalable and costlier, limiting its application only to high-speed systems like cache and buffers.[120] Erasable programmable read-only memory (EPROM) employs a floating-gate transistor array for permanent charge storage data, making it factory programmable (Fig. 1.13A).[119]. In contrast, electrically erasable memory, EEPROM, enables electrical encoding of data and reprogramming. Flash memory and EEPROM feature memory cells resemble a standard MOSFET with two transistor gates: a floating (FG) and a control (CG) (Fig. 1.13B).[72,120] Charge carriers trapped on FG affect transistor behavior allowing for logical state manipulation, storing data of 1 bit per cell, unlike multi-level cells that can store more than one bit in a single cell.

Using MOSFETs for memories and computing involves complex circuitry, multilayer systems, and multiple power sources. Moreover, it requires separate data storage and computing units necessitating data transfer between them (Fig. 1.13C), consuming significant energy and time. This traditional computing architecture faces the von-Neumann bottleneck,[121] prompting to exploration of alternative solutions.

1.5.1.3 Resistive random-access memories (ReRAMs)

Given the circuitry complexity, scalability, and operational bottleneck described above, current research is predominantly focused on ReRAMs that operate based on switching conductivity between high- (HR) and low-resistance (LR) by memory setting and resetting, respectively. Sandwiched between top and bottom electrodes, ReRAM provides simple and cost-effective fabrication potential using roll-to-roll (R2R) printing on a flexible polymeric substrate.[5] Additionally, its scalability and 3D multilayer stacking capability offer high-density data storage and efficient operation, allowing for packing more bits in a single cell. By utilizing ReRAM, the drawbacks of von Neumann computing, such as physical data movements via a bus, can be overcome through in-memory computing, where memory and computing occur in the same location, facilitated by memristors.

Additionally, the memristor possesses intriguing features of analog computation and synapse-mimicking functionalities. In fact, analog computers have historically

played a pivotal role in scientific analyses, tasks such as forecasting atmospheric conditions and predicting natural phenomena like eclipses and tides.[122] In 1956, the introduction of the perceptron by Frank Rosenblatt at Cornell University marked a significant milestone in machine learning, laying the groundwork for artificial neural networks (ANNs) and the development of AI algorithms.[123–125] However, the rise of digital technology, driven by MOSFETs,[126] led to the dominance of binary operations and the conversion of all signal storage and processing into digital counterparts, despite the high energy consumption and processing limitations.

In contrast, analog computing systems offer high efficiency at significantly lower costs and power consumption (1/1000th of digital computing).[127,128] Despite their advantages, challenges such as compatibility issues with modern hardware, poor cyclic reproducibility in multilevel output between 0 and 1, and the need for additional regulators like ASPINITY, have been identified.[122] The emergence of memristors has renewed interest in brain-inspired analog computing.[123] Memristor devices, resembling the neurons and synapses, exhibit conductance changes with external signals such as electric/magnetic or optical pulses, crucial for mimicking neuronal training. By manipulating the amplitude and frequency of input voltage pulses, the control over electrical charge linkage to the flux can be modulated on an analog basis. Decreasing the cell area to a sub-nanometer scale can further minimize the operation power. The existence of intermediate states, decay profile, state retrieval, and their strengthening with repeated pulses signifies the device's capability of synaptic

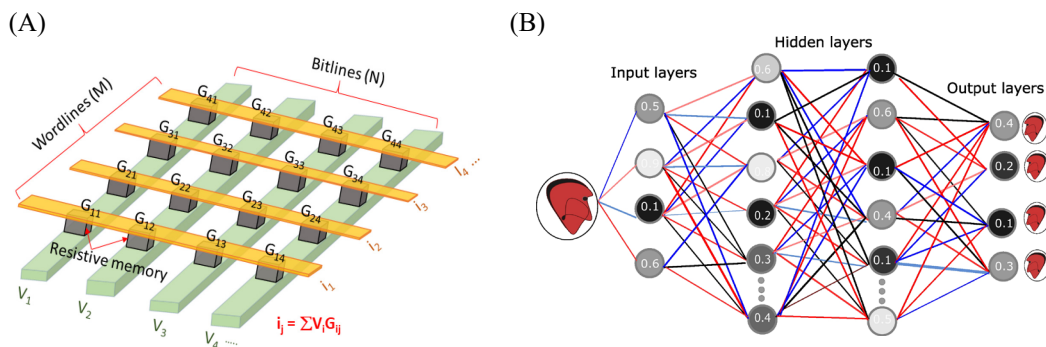


Figure 1.14: A) Schematic diagram of crossbar memory array illustrating the stacking of top and bottom electrodes, B) schematic of mapping operation via matrix multiplication used for image recognition.

functionalities such as competitive Hebbian learning.[129–131]

Analog computing has been already used for image recognition.[128] The dynamic range of the synaptic device, defined as the ratio between maximum and minimum conductance should be maximized for better accuracy in weight mapping. Memristive arrays forming neural networks (Fig. 1.14B) have demonstrated exceptional efficacy in handling cognitive processes and data-intensive tasks, even surpassing human performance in specific complex activities.

1.5.1.4 Neuromorphic computing:

Memristor-based neuromorphic computing, mimicking the brain functionality, offers computation directly within memory chips, eliminating data transfer. The Forecast predicts the global neuromorphic computing market to surpass US \$ 20 billion by 2030, driven by an annual growth rate exceeding 21 %.[132] It has found already practical use in event-driven scenarios like facial/handwriting recognition, weather prediction, stock market analysis, and speech-to-text transcription. This computing employs a unique architecture of a crossbar array of memory unit cells, sandwiched between perpendicularly aligned top and bottom electrodes (Fig. 1.15A) and, similar to ANN, it facilitates simultaneous vector-matrix multiplication of all inputs in a single output operation Fig. 1.15B.[128] An $N \times M$ memristor crossbar can perform an $N \times (N \times M)$ vector-matrix multiplication in one read operation, as the sum of individual cell operations determined by Ohm's and Kirchhoff's laws.[133] This computation highlights the inherent parallelism of memristor-based hardware.[23] This crossbar helps to minimize the device size via 3D stacking and at the same time not restricted to the binary switching of layers; instead, can be carried out with controlled weight modulation like conductance adjustment (Fig. 1.15B).[125] The presence of multiple synaptic levels, i.e. multimode conductance, enhances the adaptive learning and modeling capability.

1.5.1.5 Resistive switching (RS) mechanisms

The current in OSC is governed by injection-limited or bulk-controlled phenomena, as discussed in section 1.3. The resistive switching (RS) in memristors can be attributed to various factors as the formation and rupture of conductive filaments (CFs), valance changes, charge trapping/de-trapping, molecular conformational changes, or of the

carrier transport barrier under external electrical stimuli.[115,134–136] These effects rely on factors like the method of synthesis, selection of metal electrodes, the geometry of the active region, and interface properties.[137] Within insulating or metal oxide layers, the movement of metal ions leads to the formation of conducting filaments within the bulk of the active layer. Polymers and semiconducting materials can exhibit the formation of charge transfer complexes, which occurs mostly in donor-acceptor systems, conformational changes, phase transitions, redox reactions, and the formation of trap-assisted space charge in the bulk or at the electrode interface.[138]

Role of trap-assisted SCLC and field-induced conformational change:

In materials with low electrical conductivity with good injecting contacts the current is frequently limited by space charge and influenced by trapping of charges in localized trapping levels. Filling these traps at elevated voltage leads to a steep increase in conductivity.[139] Once the voltage reaches the so-called trap-filled-limit voltage value, V_{TFL} , all the traps are filled, and the current increases steeply (Fig. 1.15A). Moreover, the Poole-Frenkel mechanism can also play a role as explained in the previous section. If the barrier between the electrode Fermi level and the charge-transporting energy level of the OSC is sufficiently high, the F-N tunneling mechanism can occur at an appropriate electric field.

On the other hand, vinyl or polyimide-based polymers with carbazole or other charge-transporting groups arranged as a comb-like structure in the side chains exhibit a distinct switching mechanism compared to other polymer materials.[140–142] The

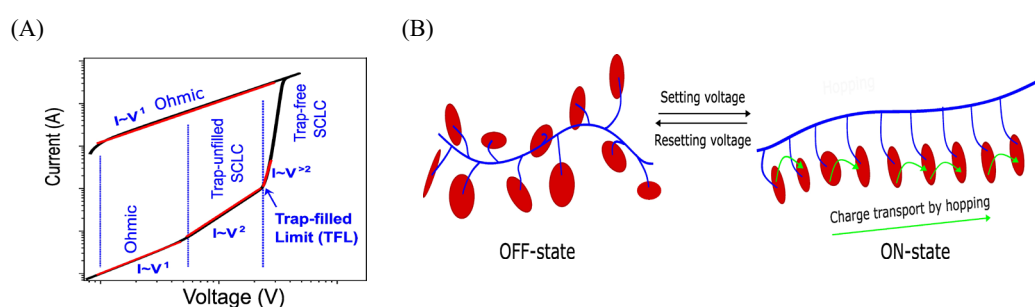


Figure 1.15: A) I-V characteristics of PCaPMA thin-film in ITO | PCaPMA | Al sandwiched structure illustrating three different conduction sections: Ohmic, trap-controlled SCLC, and trap-filled SCLC.[87] B) Schematic of voltage-induced conformational change of molecules through their functional units.[143]

carbazole moieties can be linked to the backbone through spacers of various rigidity or lengths that have an impact on the ON/OFF conductivity ratio and volatility.[141]

In the OFF state, these functional units are randomly oriented or only partially oriented. However, upon the application of an electric field, they tend to adopt a face-to-face ordered structure, resulting in conformational-induced electrical switching (Fig. 1.15B).[141] In acene-based polymers, electric field-induced intramolecular structural changes within their conjugated system have also been reported. Moreover, redox properties of the functional unit together with the control of localized states play a crucial role in memory switching and non-volatility of the conducting state.[144–146]

Redox-based switching and formation of charge-transfer complex:

Redox-based memory switching is based on the ability of organic materials to undergo reversible changes in their oxidation states.[147] By altering their electronic configurations when changing their oxidation states, these materials can modulate electrical conductivity, either gradually for analog change, or abruptly for binary operation. The reversibility of redox reactions allows the memory device to undergo repeated ON-OFF cycles. Transition metal oxides, organic redox-active molecules, certain D-A molecules, and metal-ligand coordinated frameworks are all promising candidates for redox-based memristive switching.[12,74,143,147–149]

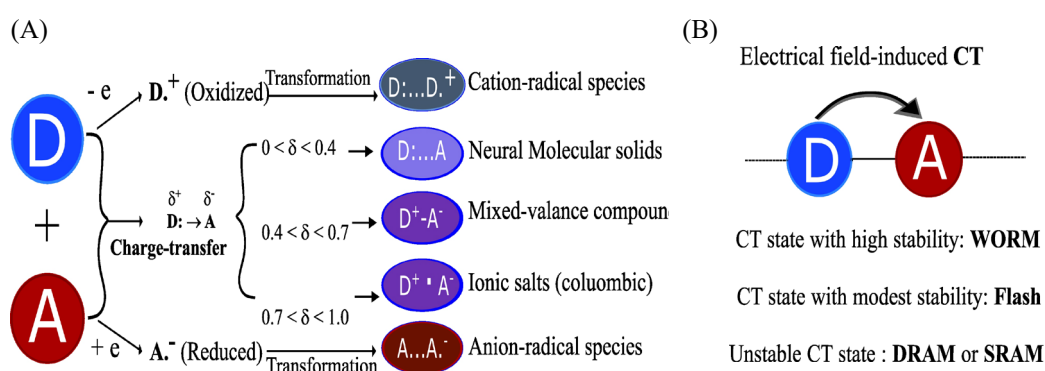


Figure 1.16: Schematic representation of A) formation of ion-radical species and charge transfer complexes with an impact on conductivity,[12] and B) formation of charge transfer complex changing the memory state.[143]

A charge transfer complex also referred to as a D-A complex, can be formed via electronic transition(s) and partial charge transfer from the donor to the acceptor moiety upon the applied voltage.[12] Similar charge transfer complexes are found in metal-ligand coordination complexes, known as organometallic charge transfer.[150–152] These systems are extensively studied for their potential applications in non-volatile organic memories. Charge transfer complex can be intramolecular or intermolecular, and it can be adjusted by modifying the size and ionization strength (IS) of individual moieties that determine the ionic binding and conductivity (Fig. 1.16).[12,143] The formation of a strong dipole moment in a polymer typically sustains the conductive charge transfer state, resulting in non-volatile behavior (Fig. 1.16B).[143]

Filament formation:

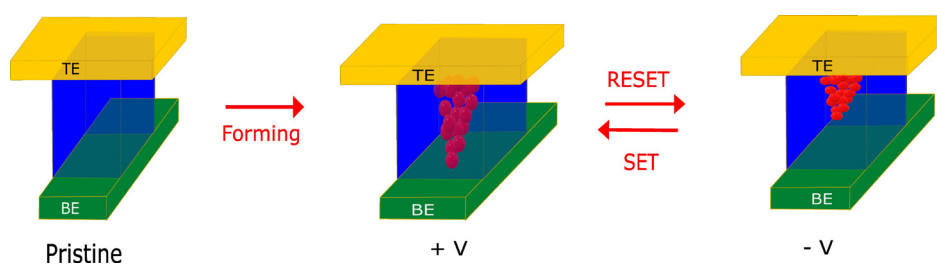


Figure 1.17: Schematic representation of the formation and rupture of filaments in the active layer sandwiched between two electrodes.

Filament formation in resistive switching occurs due to the migration of metallic ions or oxygen vacancies within the switching layer under bias.[153–155] Ions from one electrode diffuse into an active layer, forming CFs. Applying opposite polarity ruptures these filaments, returning the device to the original OFF-state (Fig. 1.17). Various methods, such as measurements of current density, *in-situ* TEM, AFM, and IR imaging using a thermal camera, were used to confirm the effect.[87,156,157]

1.5.2 Organic field-effect transistors (OFETs)

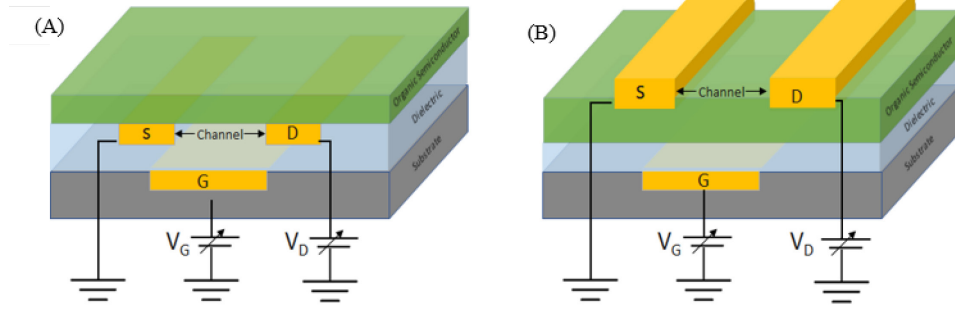


Figure 1.18: Schematics of OFETs A) bottom-gate-bottom-contact (BGBC) and, B) bottom-gate-top-contact (BGTC) structure.

OFET is a three-electrode device having source (S), drain (D), and gate (G) electrodes (Fig. 1.18). Two sets of current-voltage characteristics characterize the OFET properties: output characteristics show the dependences of the source-drain current, I_{SD} , on the source-drain voltage, V_D , with the various gate voltage, V_G , and transfer characteristics show the I_{SD} vs. V_G dependences for various V_D . Additionally, the current through the gate electrode can be measured to obtain a leakage current. There should be ideally zero I_{SD} current for $V_G = 0$. From the output and transfer characteristics, key parameters such as mobility (μ), threshold voltage (V_{th}), and current ON/OFF ratio (I_{ON}/I_{OFF}) can be determined.

Two regions can be distinguished in the current-voltage characteristics:[158]
linear region: for $V_D < V_G$, a linear approximation holds, given by Eqn. 1.19:

$$I_{D_lin} \cong \frac{W}{L} C_i \mu (V_G - V_T) V_D - \frac{V_D^2}{2} \quad (1.14).$$

saturation region: for $V_D > V_G$ and Eqn. 1.20 applies as:

$$I_{D_sat} \cong \frac{W}{2L} C_i \mu (V_G - V_T)^2 \quad (1.25)$$

Here, W and L are the channel width and length between the source-drain electrodes, respectively, and C_i is the capacitance per unit area. The charge carrier mobility can be obtained either by differentiating the linear part of the transfer characteristics as

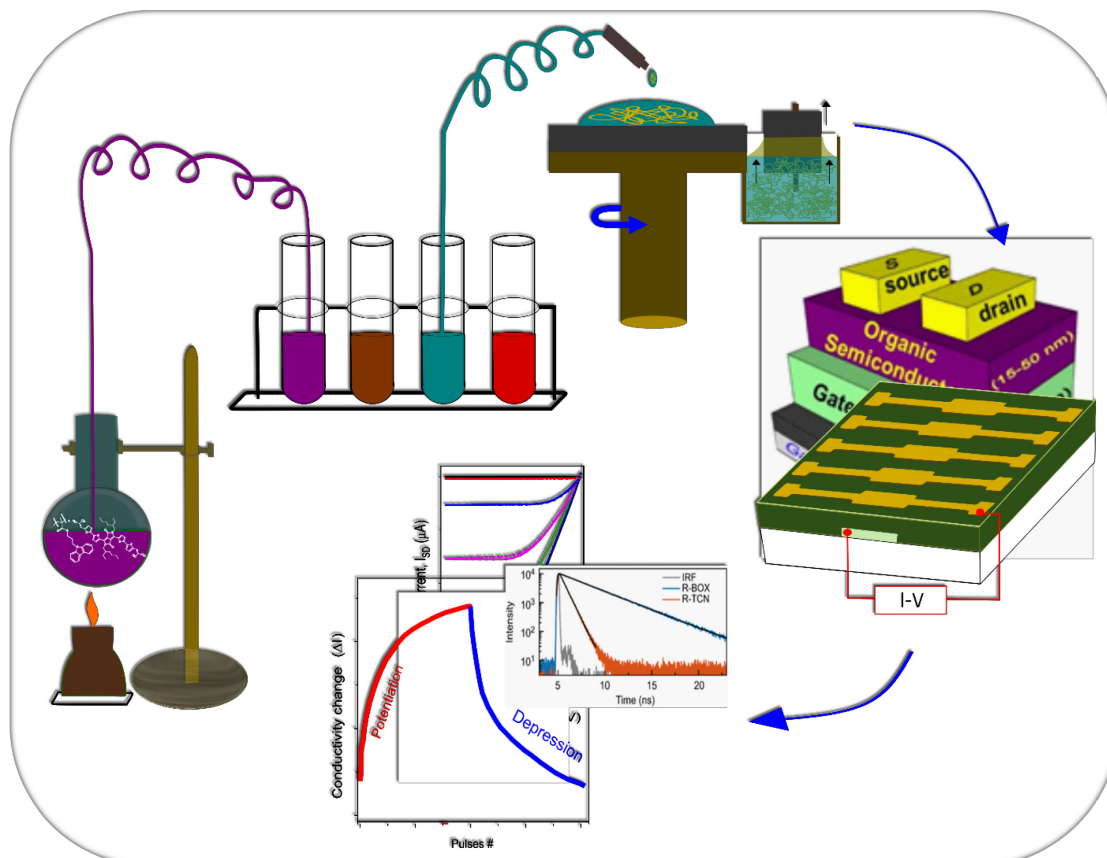
$$\mu_{lin} \cong \frac{L}{W C_i V_D} \frac{\partial I_{D_lin}}{\partial V_G} \quad (1.26)$$

or from the slope of the $\sqrt{I_{D_sat}}$ vs. I_G dependence. The mobility depends on many factors like free charge carrier concentration, electric field, and temperature.

Electric field, as described by the Poole-Frenkel approximation, has a direct impact on mobility as the field modifies the potential barrier and tunneling rate between transport sites.[19,25] However, a reverse effect has been observed in single crystals along the directions of the applied field, showing the band-like transport.[22] Crystals formed by π -conjugated small molecules in the herringbone-like arrangement often facilitate 2D transport.[159] This signifies the effect of crystal anisotropy on mobility as documented by differences between dip-coated and spin-coated layers of TIPS-pentacene.[160] Crystals aligned perpendicularly to the S-D electrodes (i.e., parallel to the direction of CT) exhibit higher mobility compared to parallel alignment.

Some dielectrics, particularly those with polar groups like hydroxyl or cyano-groups tend to create trap DOS in the OSC active channel due to the charge-dipole interaction. This adverse effect can be minimized by crosslinking or by self-assembling a monolayer (usually silane) on top of the dielectrics.[160–162] OFETs can be fabricated with various device geometries, but the most common are those with bottom-gate-top-contact (BGTC) or bottom-gate-bottom-contact (BGBC) (Fig. 1.18). With the current charge carrier mobility of some OSCs reaching up to $20 \text{ cm}^2\text{V}^{-1}\text{s}^{-1}$ OFETs show electrical parameters already comparable to amorphous silicon.[163,164] They found practical applications in AMOLED displays, RFID tags, and sensors for health monitoring. Recently also some more advanced applications of OFETs have occurred, such as memory and adaptive devices, or electronic elements working as artificial neuronal synapses.[25,164,165]

2. Materials and Methods



2.1 Materials

Various materials for synthesis and characterization were used for the Thesis. Many synthetic precursors and reagents like $\text{PdCl}_2(\text{PPh}_3)_4$ and malononitrile were obtained from Precmet (Australia) and TCI (Germany), respectively. Compounds like 2-(tributylstannyl)-1,3-benzoxazole, 5-(4,4,5,5-tetramethyl-1,3,2-dioxaborolan-2-yl)thiophene-2-carbaldehyde, and 3,6-di(thiophen-2-yl)pyrrolo[3,4-c]pyrrole-1,4(2H,5H)-dione, were purchased from Alfa Chemistry, AKSci and Combi-Blocks (USA). All chemicals were employed without further purification. Substrates including glass, ITO-coated glass, and sapphire were purchased from Ossila Ltd (Netherlands), and quartz from Präzisions Glas & Optik GmbH (Germany). Solvents used for synthesis and preparation of samples for electrical and optical measurements, like dimethyl sulfoxide, acetonitrile, chloroform, chlorobenzene, dioxane, ethanol, methanol, and ether, were sourced from P-LAB (Prague, Czech Republic). Similarly, compounds like N-bromosuccinimide, Al_2O_3 , $\text{Pd}(\text{PPh}_3)_4$, 2-ethylhexyl bromide, and salts, such as tetrabutyl ammonium hexafluorophosphate ($n\text{-Bu}_4\text{NPF}_6$), lithium perchlorate (LiClO_4), K_2CO_3 and Na_2CO_3 were sourced from PENTA (Czech). The compounds used for the device fabrication are described by category below:

2.1.1 π -Conjugated small molecules

π -Conjugated small molecules, with typically planar, disc-shaped symmetrical structures, such as 6,13-bis(triisopropylsilylethynyl)pentacene (TIPS-pentacene), perylenes diimide (PDI) and thiophene-diketopyrrolopyrrole (TDPP) derivatives have been used as active layer for various optoelectronic characterization.[17,160,166,167] Despite being bonded together by weak van der Waals forces, these molecules often form crystalline or polycrystalline structures with CT properties close to band transport. However, they often face challenges such as self-aggregation, leading to their poor solubility. Other preparation methods such as PVD have to be employed.

TIPS pentacene (Fig. 2.1A), a p-type semiconductor possessing a high mobility ($\sim 0.92 \text{ cm}^2/\text{Vs}$), features extended π -conjugation.[17,160] This compound was obtained from Ossila Ltd. The substituent bridged with the ethynyl group yields the material an increased solubility. During solidification, it facilitates face-to-face stacking and prevents oxidative degradation of the central acene.[168]

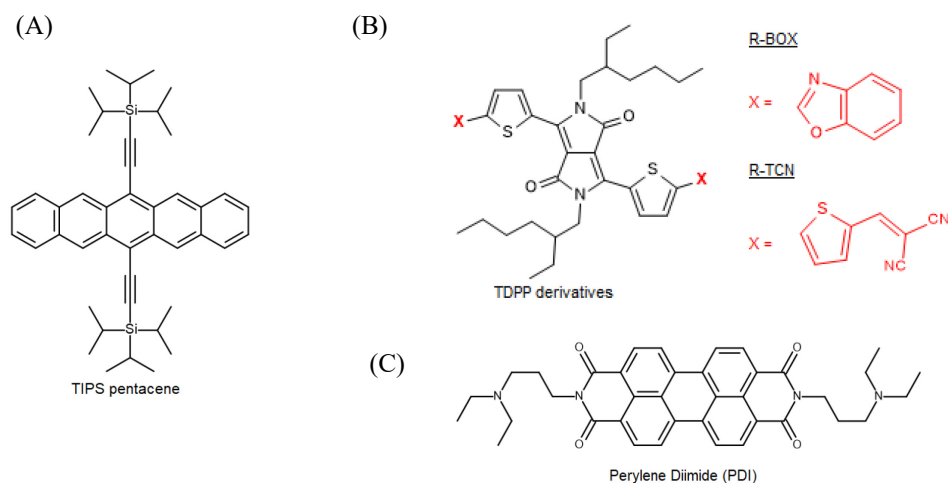


Figure 2.1: Molecular structure of A) 6,13-bis(triisopropylsilylethynyl)pentacene (TIPS pentacene), B) thiophene-diketopyrrolopyrrole (TDPP) derivatives, C) perylene diimide derivative (PDI)

Conversely, PDI is an n-type π -conjugated semiconductor (Fig. 2.1C). It was purchased from Centrum organické chemie, Rybitví, Czech Republic. PDI derivatives are widely used in organic electronics, due to their low-lying energy levels, high carrier mobility, large extinction coefficient, and excellent stability.[169]

For the photophysical studies, symmetric TDPP derivatives with diverse functional end groups were synthesized. Two groups (Fig. 2.1B), published in ChemPhysChem (**Attachment 1**) [167] are presented here. The synthesis involved Suzuki-Miyaura cross-coupling and Knoevenagel condensation with TDPP-Br as a source material used for obtaining the studied derivatives.[167,170,171]

2.1.2 Semiconducting polymers

A high-mobility D-A copolymer, poly[2,5-(2-octyldodecyl)-3,6-diketopyrrolopyrrole-alt-5,5-(2,5-di(thien-2-yl)thieno [3,2-b]thiophene)] (**DPPDTT**) (Fig. 2.2A), used in our study was acquired from Ossila Ltd.[166] This material exhibits good solubility, flexibility, and chemical and thermal stability which makes it suitable for applications in flexible electronics.[172,173] This polymer is made of monomers containing bulky core unit, DPP, and thieno-thiophene (TT) side groups that minimize the bandgap and enhance planarity favorable for hole mobility. Good miscibility with small molecules enables the formation of composite systems. In this thesis, DPP DTT

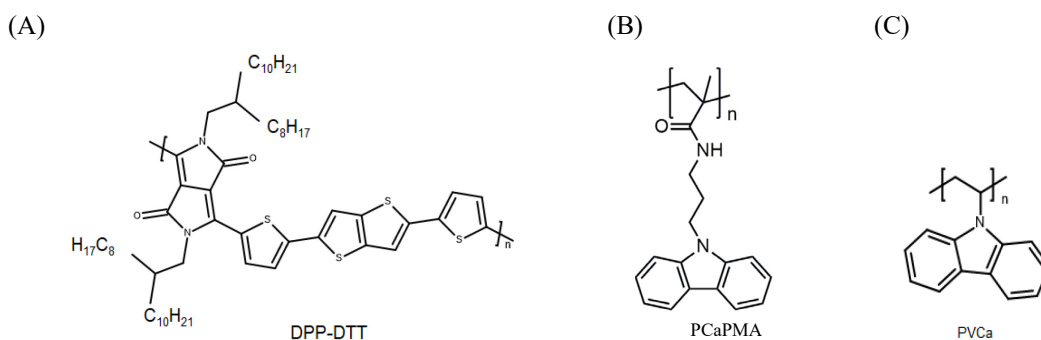


Figure 2.2: Molecular structure of A) 2- poly[2,5-(2-octyldodecyl)-3,6-diketo-pyrrolopyrrole-alt-5,5-(2,5-di(thien-2-yl)thieno[3,2-b]thiophene)](DPPDTT), B) poly(N-(3-(9H-carbazol-9-yl)propyl)methacrylamide (PCaPMA) & C) polyvinylcarbazole (PVCa).

was studied in OFETs and ReRAM devices, both individually and as a composite system with PDI (**Attachment 4**).[166]

Carbazole-based polymers have been extensively studied for decades mainly due to their photoconductivity.[216] In this thesis, polymers with saturated backbone and charge-transporting carbazole units attached as side groups were studied mainly for their memristive properties.[87,131] Poly(N-(3-(9H-carbazol-9-yl)propyl)methacrylamide (PCaPMA) was synthesized using three steps of monomer preparation,[87] followed by a radical polymerization. The details of synthesis together with the structural characterization are reported in **Attachment 2**. [87] Polyvinyl carbazole (PVCa), purchased from BASF Aktiengesellschaft, was used for the comparative study.

2.1.3 Polymer dielectrics, crosslinkers, and passivators

To fabricate OFETs, various polymer dielectrics were used and their effect on device performance was studied. Polymers like polyvinyl phenol (PVP) and poly(vinylalcohol-co-vinylcyanoethoxy) (CEPVA) were employed as dielectric layer due to their high dielectric constant (ϵ') and low conductivity (σ'). In CEPVA, despite having high ϵ' (~ 15), its low glass transition temperature ($T_g \sim 19^\circ\text{C}$) creates problems with mechanical stability already at room temperature. To overcome this problem, crosslinking was applied using various crosslinkers listed in Fig. 2.3B.[174] Crosslinking also proved to be beneficial by reducing the hydrophilicity of the layer surface by minimizing hydroxyl groups that usually occurred as the residues from

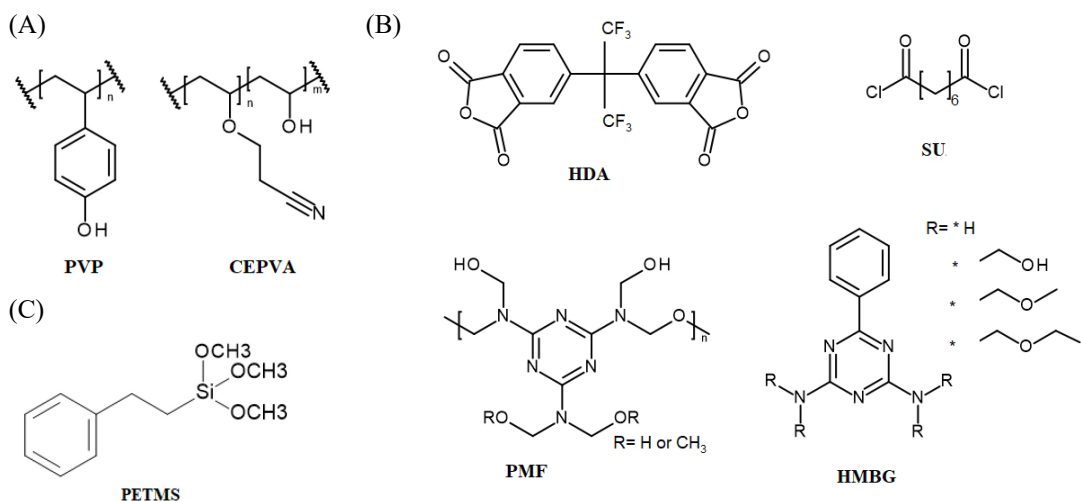


Figure 2.3: Chemical structures of used A) dielectrics, and B) used crosslinkers and C) self-assembled monolayer.

polyvinyl alcohol during synthesis. Moreover, trimethoxy(2-phenylethyl) silane (PETMS) was used as a self-assembling monolayer (SAM) to passivate the dielectric surface reducing the trap DOS caused by the presence of polar groups from dielectrics.

2.2 Device preparation

2.2.1 Preparation of active layers

Thin films of the required thickness (usually 30 nm – 1 μ m) were prepared mainly using spin coating, dip coating, or physical vapor deposition (PVD). Before layer deposition, the substrates were cleaned in an ultrasonic bath subsequently with soap water, de-ionized water, acetone, and isopropanol, each for 15 minutes, followed by drying with compressed nitrogen gas and ozone cleaning for 20 minutes. The layer thicknesses were determined using a profilometer (for film prepared with solution casting) or followed in-situ during deposition by quartz-crystal microbalance (for PVD). Solution processing deposition techniques (dip-coating, spin-coating, or screen-printing, Fig. 2.4A-B) were mainly used for polymer layer preparation from solutions. The dip-coating technique is very useful to control the size and orientation of crystal domains. In this technique, the substrate emerged vertically into a solution, followed by its withdrawal at a rate of 4 mm/min at ambient laboratory conditions.[160] The thickness and morphology of the layer can be well-controlled by using different concentrations of solution, revolution/withdrawing speed, and

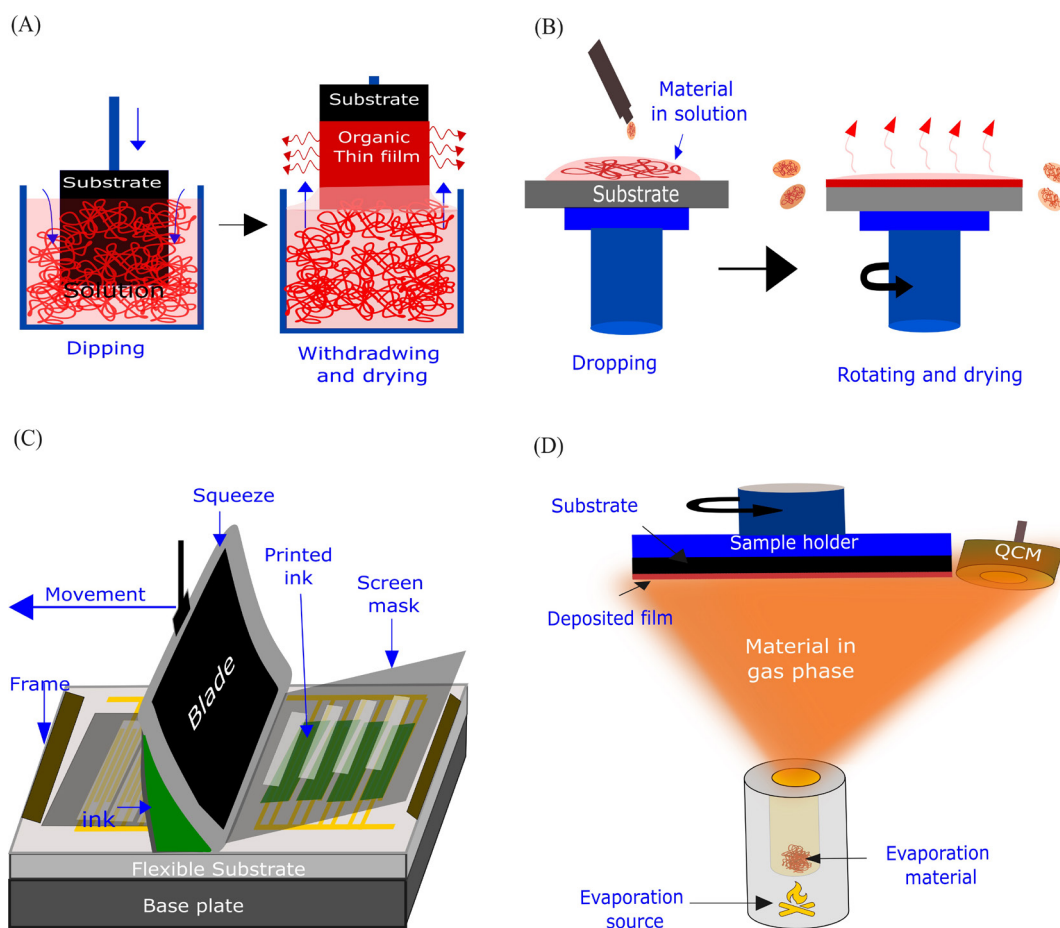


Figure 2.4: Schematic of thin film preparation using A) dip-coating B) spin-coating C) screen printing, and D) physical vapor deposition (PVD) method.

volatility/viscosity of the solvent used for solution preparation. With spin-coating, crystal orientation could not be controlled but the layers are usually more homogenous.

Screen-printing is a facile and cost-effective method proposed for film preparation in flexible substrates. The layer-by-layer printing is highly effective in the manufacturing process where the thickness of the layer can be effectively controlled by solution concentration and pressure applied on the printing blade (Fig. 2.4C). This is superior to other solution casting techniques as it is more material-efficient for layer preparation on an industrial scale without wasting the material. However, controlling the homogeneity in ultra-thin layers on a sub-nm scale is challenging. For layer-by-layer casting, the use of orthogonal solvents for different layers or crosslinking of the bottom layer is mandatory to avoid the dissolution of the previously cast layer.[175]

Physical vapor deposition (PVD) offers an alternative way of thin layer preparation when low-molecular-weight materials lack solubility. In PVD, materials

transition from solid-state to gas phase and condense at the substrate, yielding an ultra-smooth, highly homogenous layer (roughness $\sim 1\text{-}3$ nm) with crystallinity controlled by evaporation rate. Minilab 060 evaporator (Moorfield, UK) operating under ultra-high vacuum conditions (of 3×10^{-7} mbar) was used for thin film deposition from organic materials and metal electrodes (Fig. 2.4D). The vacuum environment prevents oxidation at a high temperature and ensures the purity of deposited layers. Lateral structuring is achievable using a shadow mask. Deposition rate, substrate temperature, and sample holder rotation speed influence the film quality. A slow deposition rate ($\sim 0.3\text{-}0.5$ Å/s) and substrate rotation (~ 10 rpm) were found to yield smooth organic layers. Film thickness was monitored with a quartz-crystal microbalance. Post-deposition treatment (temperature or solvent annealing) of layers was carried out to increase the crystallinity of the layers.

2.2.2 Device fabrication

2.2.2.1 Fabrication of ReRAM devices:

The ReRAM devices (Fig. 2.5) were fabricated by sandwiching an organic layer between the ITO bottom electrode (BE, ~ 100 nm) on the glass substrate and Al or Au top electrode (TE, ~ 100 nm) deposited by PVD using a shadow mask. The ITO electrodes were chemically etched to an appropriate pattern (usually 2 mm strips). The organic low-molecular-weight materials were deposited by PVD, while polymer films were mostly cast from solution. Active cross-sections varied between 2 & 0.15 mm².

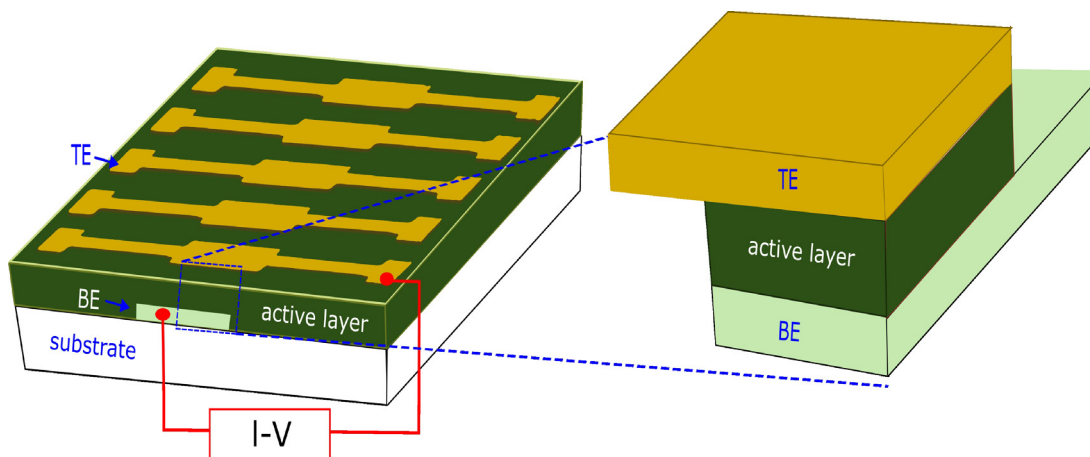


Figure 2.5: Structures ReRAM device with active layer sandwiched between the top electrode, TE, and bottom electrode, BE.

2.2.2.2 Fabrication of OFETs

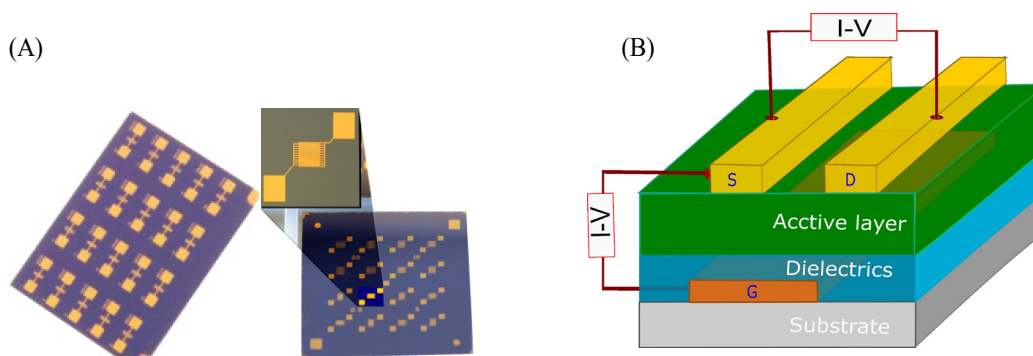


Figure 2.6: Structures of A) individual substrate, left and right, respectively purchased from Ossila.ltd, & Fraunhofer Ltd.,[176,177] for OFET testing, B) schematic of BGTC structure.

Two types of OFET structures were fabricated: bottom-gate bottom-contact (BGBC) and bottom-gate top-contact (BGTC) (Fig. 2.6). For BGBC, silicon chips with heavily doped silicon gate electrodes and 200-300 nm thick thermally grown SiO_x dielectrics were used, either manufactured by Ossila Ltd., or by Fraunhofer Ltd., both with deposited S-D electrodes on dielectrics. BGTC configuration of the OFET featured an organic dielectric layer (PVP or CEPVA, thickness 100-800 nm) cast on a glass|Al or polyethylene-terephthalate (PET)|Al substrate. Al electrodes (thickness 60-100 nm), acting as a gate, were PVD-deposited and subsequently anodized electrochemically in an electrolyte made of 3 weight % electrolytic solution of trisodium citrate dihydrate and citric acid (9:1 ratio) in deionized water and ethylene glycol (1:1 ratio) applying 20 V. The procedure provided about 32 nm thick AlO_x. Polymer dielectric layers were thermally crosslinked using various crosslinkers listed in Fig. 2.3B. The ratio of polymer and crosslinker was 4:1 and crosslinking was done at 120 °C in a vacuum oven, pressure 100 mbar, for 2 h.

In some OFETs, surface passivation (silanization) of dielectrics was carried out prior to the OSC deposition, using trimethoxy(2-phenylethyl) silane (PETMS) cast from solution. In BGTC, Au S-D electrodes were deposited by PVD.

2.2.2.3 Fabrication of device for spectro-electro chemical measurements

For the spectro-electrochemical measurements, glass | ITO (100 nm) | active layer (50 - 100 nm) | gel electrolyte (150 μm) | ITO (100 nm) | glass structures (Fig. 2.7) were fabricated. The active layer was prepared in the same way as used for fabricating

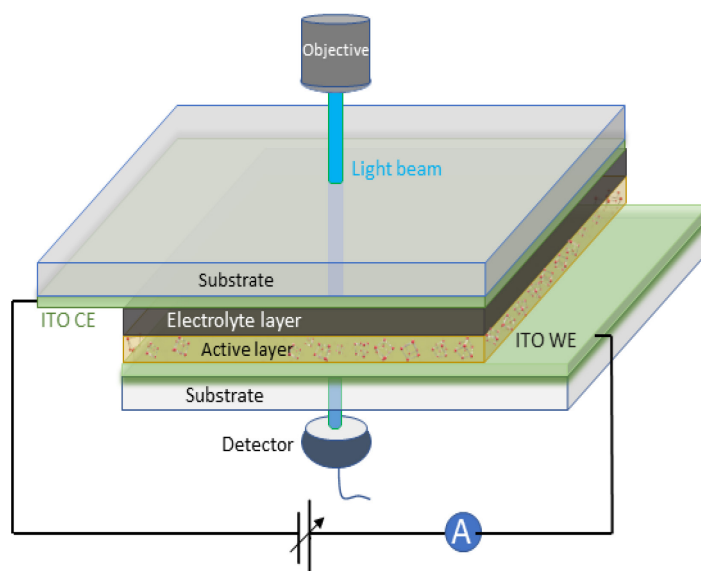


Figure 2.7: Schematic of device used for spectro-electrochemical studies glass | ITO | active layer | electrolyte layer | ITO | glass and the measurement setup.

memristive devices. The gel electrolyte was prepared by gradually adding and stirring lithium perchlorate and polymethyl methacrylate, 10 g each, in 55 ml of polypropylene carbonate until the transparent solution was formed. Air bubbles formation was prevented during fabrication.

2.2.3 Device characterization

2.2.3.1 Optical characterization:

UV-vis absorption and fluorescence spectra were obtained in solutions and on thin films using a spectrophotometer Lambda 950 (PerkinElmer, USA) and FS5 fluorimeter (Edinburgh Instruments, UK), respectively. Temperature dependences of the spectra were measured in a water-cooled Peltier (PTP1, PerkinElmer, USA) sample holder. For thin films with higher opacity, an integration sphere was employed. Fluorescence emission spectra were recorded at multiple excitation and emission wavelengths to assess material purity/homogeneity.

FS5 spectrometer with SC-30 integrating sphere was used for the fluorescence quantum yield measurements. These measurements were performed on dilute solutions with maximum absorbance below 0.05 to avoid any reabsorption effect. The same solvent used for solution preparation was used as a reference. The QY was then calculated by integrating the area under the spectrum using the equation:

$$QY_{obs} = \frac{\int_{\lambda_1}^{\lambda_2} I_{E_Solution} - \int_{\lambda_1}^{\lambda_2} I_{E_Ref}}{\int_{\lambda_1}^{\lambda_2} I_{S_Solution} - \int_{\lambda_1}^{\lambda_2} I_{S_Ref}} \quad (2.1)$$

Where, I_E and I_S represent emission and scattering intensity, respectively, and λ_1 and λ_2 denote spectral selection limits.

Fluorescence lifetime was determined using the time-correlated single photon counting (TCSPC) technique using FluoTime 300 (PicoQuant, Germany) connected to a Solea excitation source at 80 MHz repetition rate. The instrument response function (IRF) was around 200 ps full width at half maximum. For NIR-emitting materials, a PMT detector with voltage ranging from 700 to 900 V was employed.

Transient absorption spectroscopy (TAS), referred to as the optical pump-probe technique, is an efficient tool for investigating the dynamics of molecules in their excited state and the subsequent reaction or product formation. It involves pumping samples with intense laser pulses and measuring their relaxation processes through the course of optical absorption with low-intensity probe light. TAS yields real-time insights into phenomena like internal conversion, excited state migration, charge and energy transfer, new chemical species formation, charge-separated states, and energy transfers.[178]

For femtosecond pump-probe spectroscopy measurements, a setup consisting of with Mantis (Coherent, USA) seeded regenerative amplifier (Legend Elite, Coherent, USA) was used (Fig. 2.8). The laser setup provided pulses with 2.1 W power at a 1 kHz repetition rate centred around 800 nm [159] and probe beam (430-830 nm) was a white light continuum generated on a 3 mm CaF₂ or sapphire crystal. The pump beam was generated by a commercial optical parametric amplifier (TOPAS C, Lithuania). The pump beam was of Gaussian profile with a diameter ($1/e^2$) was 80 μm while the probed beam was elliptical, with diameters of ~ 210 and ~ 330 μm . A magic angle (54.7°) polarization was maintained for the measurements. A typical IRF was around 150 fs. For the nanosecond flash photolysis, a pump beam was generated using Nd: YAG laser (Surelite SL I-10, Continuum, USA) operating at a repetition rate of 10 Hz,

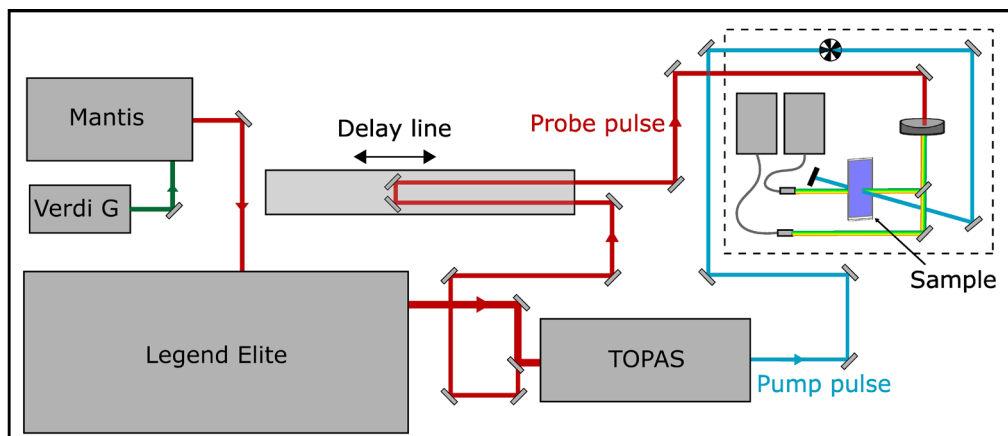


Figure 2.8: Schematic of pump-probe laser setup for TAS measurements.

while the probe beam was electronically synchronized with an output of a femtosecond amplifier (800 nm, Legend Elite, Coherent, USA) operating at 20 Hz.

Solutions were measured in a 2 mm cuvette under continuous stirring. Thin films were measured using a translation stage and a relatively lower pump power to minimize fluence-dependent processes such as singlet-singlet annihilation, photodegradation, or influence of long-living states.

The measurements were performed in a transmission mode measuring the change in the layer absorbance ΔA before and after excitation:

$$\Delta A = \log\left(\frac{P_0}{P_t}\right) \quad (2.2)$$

where, P_0 and P_t are the power of the probe laser beam transmitted by the sample before the pump pulse and at the delay time t after the pump, respectively.

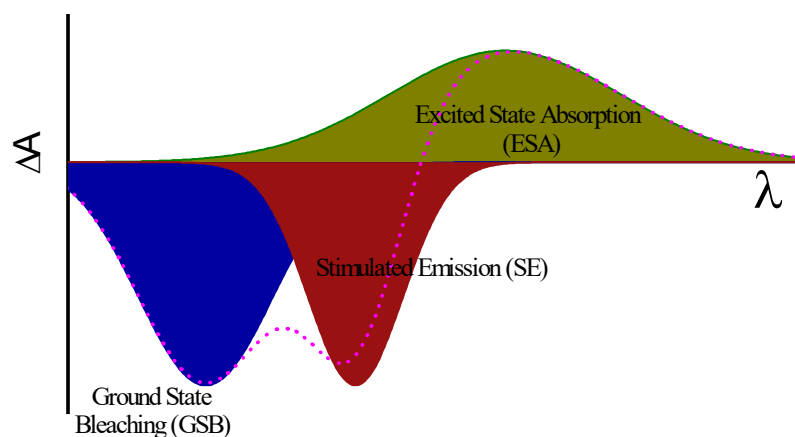


Figure 2.9: Schematic of TA spectrum (dash and dot line) and its components: ground state bleach (GSB), stimulated emission, and excited state absorption (ESA).

The TAS spectrum (Fig. 2.9) encompasses the negative signal of ground-state bleach (GSB) caused by the decrease in ground-state absorption and stimulated emission, and positive signals of excited-state absorption (ESA).[178] The ESA can be caused by optical transitions from an excited state to a higher excited states. ESA can also result from other processes like charge transfer states or photoreaction products.[178,179]

Raw transient absorption data were background-subtracted, chirp-corrected, and analysed using Glotaran software package.[180] Data obtained from femtosecond and nanosecond pump-probe experiments were analysed using Global Analysis, a method extracting information about the excited- state dynamics. This technique performs a simultaneous fit to an entire dataset using a model based on a set of differential equations describing various processes like energy/charge transfer and ISC.[181] The related parameters and rate constants were then optimized with the initial and final populations of the excited states to obtain the best fit for the experimental data using techniques like least-squares fitting or maximum likelihood estimation.[182] The yield of the triplet population was determined using the singlet depletion method.[183]

2.2.3.2 Broadband dielectric (relaxation) spectroscopy

Broadband dielectric spectroscopy (BDS) measurements were conducted using a Novocontrol Broadband Dielectric Spectrometer (Novocontrol technologies, Germany), equipped with an Alpha frequency analyzer and QUATRO temperature controller, operating with 0.5-1 V_{AC} and within frequency and temperature range of $10^{-2} - 10^7$ Hz and -100 to 220 °C, respectively. In both increasing and decreasing temperature ramps, 10°C/min was maintained followed by 2 min stabilization before each measurement.

BDS is a powerful tool for impedance analysis in a wide range of temperature and frequency. Besides giving information on complex permittivity, i.e. dielectric constant and electrical conductivity, this method allows for the examination of various dipolar relaxations or charge carriers transport mechanisms. It also provides information on structural conformation changes and polymer segmental motion.[184]

Through the changes in the complex permittivity frequency spectrum with temperature, it effectively detects phase transitions like glass transition, melting, or crystallization, known as primary transitions.[55] Additionally, it can detect localized relaxation mechanisms, such as the rotational or wagging motion of side-groups or

end-groups of macromolecules, referred to as secondary transitions. This technique is particularly sensitive to the motion of polar groups, such as -C=O, -C-OH, and -C-N-H, providing insights beyond those offered by conventional thermal analytical methods like differential calorimetry.[108]

With BDS, usually the complex capacitance C^* is measured in dependence on angular frequency, ω , and temperature, T, defined by the equation:

$$C(\omega) = \varepsilon_0 \varepsilon^*(\omega) \frac{A}{d} \quad (2.3)$$

where, ε^* is the complex permittivity and ε_0 is the permittivity of vacuum, A and d , are the area and thickness of the measured cell, respectively. From the complex permittivity, other parameters can be calculated, like conductivity

$$\sigma'(\omega) = \varepsilon_0 \omega \varepsilon''(\omega) \quad (2.4)$$

and modulus, $M^* = 1/\varepsilon^*$, which were used for the characterization of charge transport and relaxation phenomena.

2.2.3.3 EC and SEC characterization

Cyclic voltammetry was acquired on active materials deposited on ITO|glass as a working electrode, using an AMEL s.r.l. potentiostat (Italy). A 0.1 M electrolytic solution of n-Bu₄NPF₆ or n-Bu₄ClO₄ in acetonitrile was used, with Pt and Ag | AgCl wire serving as counter and reference electrodes, respectively. As an internal reference, a 10 mM ferrocene solution was used in the same electrolyte. For SEC measurements, the same sandwiched structure as the memristive system was used but covered with an additional ITO | glass as TE and a gel electrolyte layer between the active layer and TE (Fig. 2.7). The spectral measurement was performed following a voltage application for 10 s to allow for completion of redox processes within the layer.

2.2.3.4 Electrical characterization

Electrical characterization of memory devices was performed using a Keithley 2602 source meter (Keithley Instruments, USA), in the air or inside a vacuum chamber (turbomolecular pump, Pfeiffer Vacuum GmbH, Germany) controlled by a HAAKE F6 thermostat (Thermo Haake, Germany). Voltage sweeps from 0 V to $\pm U_{\max}$ was applied repeatedly in cycles, with voltage polarity referring to the ITO BE. Temperature dependences were measured inside a

vacuum at various temperature ranges and sweeping rates, allowing the proper time for the sample to thermally stabilize before performing each measurement. For synaptic plasticity measurements, voltage-induced multimodal changes in resistance were measured, mainly the current as a function of time, frequency, and amplitude of electrical trigger pulses.[131] These measurements were performed on the same devices used for digital memory characterization. For the analogy to neuronal synapsis behaviour, TE and BE were assigned as pre-synaptic and post-synaptic neurons, respectively. Two types of voltage-sweeps were applied to confirm the analog property: continuously increasing/decreasing sweep-based ($0 \rightarrow \pm 0.5$ V) and fix pulse-based (usually trigger pulses of ± 0.5 V), in a given number of cycles. The continuous change in device conductance was probed by a reading pulse of 50 mV, applied after a very short time-interval, Δt of 10 - 20 ms, after each trigger pulse. The polarity-dependent change in device conductance was attributed to potentiation and depression of neuronal synapses.

For the characterization of field-effect transistors, the same electrical setup was exploited, with the second channel of Keithley 2602 serving as a power supply for the gate electrode. Both output and transfer characteristics, in air and in an inert atmosphere, were measured with a sweep rate of 0.5 Vs^{-1} . The field-effect mobility (μ) and threshold-voltage (V_T) were extracted from the transfer curves.

2.2.3.5 *Surface profilometry*

Tencor P-17 stylus profilometer (KLA, USA) employing a 2D or 3D scan or atomic force microscope (AFM) operating in the tapping mode (OTESPA-R3, Bruker) at a resonance frequency of 150 kHz, to find out the surface profile (roughness) and film thickness in Å to nm range. For the 3D scan using a profilometer, a slow scan-speed of $2 \mu\text{m/s}$, 2000 Hz bandwidth, and a scanning density of 1 line per 500 nm was used.

2.2.3.6 *Other characterization methods*

Attenuated total reflectance Fourier-transform infrared (ATR FTIR) spectroscopy was used to characterize the bonding configuration or chemical composition of the materials. Polymer thin films cast on Al foil were recorded using a Nicolet Nexus 870 FTIR spectrophotometer (ThermoScientific, Canada), in an ATR Golden Gate unit

(Specac) equipped with a diamond prism and a controlled heated top plate in a dry-air-purged environment. This technique operated in an energy regime is sensitive to intramolecular bonding-deformation excitations, including vibrations, rotations, and stretching modes. For *in-situ* temperature measurements of PCaPMA, the spectra were recorded at 5 °C steps in the interval 25 – 100 °C, and at 10 °C steps between 100-150 °C, followed by cooling of the sample in 10 °C steps.

X-ray Diffraction (XRD) patterns were collected using a high-resolution Explorer diffractometer (GNR, Italy) with a Mythen 1K strip detector, operated at 40 kV and 30 mA. The measurements were performed under the CuK α radiation using Bragg - Brentano geometry, in a 2 θ range, with a 0.05° step and a step time of 10 s. The peak deconvolution was carried out using the Fityk 1.3.1 program.[185]

¹H and ¹³C NMR spectra were recorded at 400 and 100 MHz at 25 °C with a Bruker AVANCE III 400 instruments equipped with BBO/Prodigy cryoprobe. Chemical shifts are reported in ppm relative to TMS signal. The residual solvent signal in ¹H and ¹³C NMR spectra was used as a reference (CDCl₃ 7.25 and 77.23 ppm). Apparent resonance multiplicities are described as s: singlet, d: doublet, and m: multiplet.

Gel permeation chromatography was obtained on a Shimadzu HPLC (Kyoto, Japan) chromatograph equipped with a PDA detector. Thin-layer chromatography was conducted on aluminium sheets coated with silica gel 60 F254, with visualization using a UV lamp (254 or 360 nm).

Differential scanning calorimetry (DSC) curves were measured using a DSC calorimeter Q2000 (TA Instruments, USA) at a scan rate of 5 °C/min in a nitrogen environment. This technique was utilized to measure the heat flow of a sample as a function of temperature through which the thermal transitions such as glass transition temperature, crystallinity, and melting properties of the materials can be investigated.

Thermogravimetric analysis (TGA) of the organic materials was carried out on thermogravimetric analyser, Pyris 1 TGA (PerkinElmer, USA) in the temperature range 35-800 °C at the rate 10 °C min⁻¹ with the fixed air flow rate at 25 mL min⁻¹.

Wettability (surface energy) of the substrates and organic layers was characterized using a contact angle method, measured as an angle between the edge of the liquid drop (usually water ~3-5 μ L) and the substrate/layer surface. Contact angle goniometer OCA 20 (Dataphysics, Germany) equipped with SCA 21 software was used for the measurement, and the profile was fitted using the Young–Laplace equation.

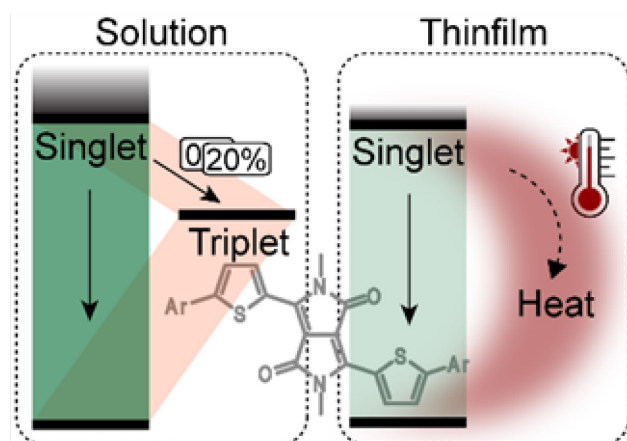
3. Results and Discussion

3.1 Photophysics of TDPP derivatives: Insights into ultrafast processes

This part of the study is based on:

Y.R. Panthi, A. Thottappali, P. Horáková, L. Kubáč, *Photophysics of benzoxazole and dicyano functionalised diketopyrrolopyrrole derivatives : Insights into ultrafast processes and the triplet state*, ChemPhysChem. 25 (2024) e202300872.

<https://doi.org/doi.org/10.1002/cphc.202300872> (Attachment 1) [167]



3.1.1 Overview of the study

Thiophene-diketopyrrolopyrrole (TDPP) molecules have been recently extensively researched in the field of OSCs due to their remarkable stability, strong optical absorption, and ease of synthesis.[186] TDPPs, featuring a D-A molecular structure, exhibit an efficient intramolecular charge transfer facilitating low-energy photon absorption extended to the NIR region.[159] Through a proper molecular design, the derivatives of TDPPs can facilitate efficient π - π stacking. This approach allows for a precise energy level adjustment through functionalization and alkylation at various positions of the core of the molecule, offering many opportunities for tailoring the structure-to-property relationship required for the targeted optoelectronic applications.[187,188] Such structural engineering can not only mitigate nonradiative losses but it can also enhance the diffusion length of excitons by extending their lifetime.[189,190] Understanding the photophysics of TDPP molecules is crucial for managing excitonic processes such as triplet fusion, temperature-activated delayed fluorescence, and singlet fission (SF), pivotal in optimizing organic photovoltaic devices.[100,191–194] Particularly in the context of SF, the TDPPs present intriguing prospects as the process efficiency can be modulated by the molecular structural modification through alkylation or functionalization and by tuning the sample morphology by some suitable post-processing method like the solvent vapor or thermal annealing.[107,195,196]

Studying the photophysics of individual molecules in dilute solutions and in their aggregated state offers insights into the underlying processes of observed phenomena. For instance, investigating triplet ISC formation in solution establishes a direct structure-property relation on a molecular level.[197] For some processes, like for the SF, the formation of dimers is crucial and can be achieved in a polar medium.[198,199] However, analysis of such interactions in solid-states is a complex

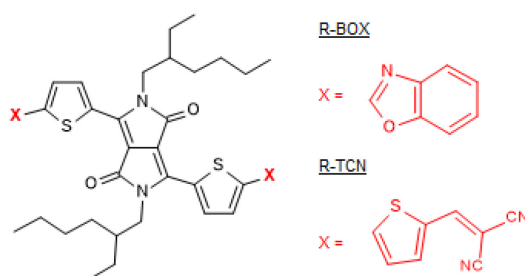


Figure 3.1: Chemical structure of TDPP derivatives, R-BOX & R-TCN (**Attachment 1**).

issue due to numerous close-range interactions.[200] Conformational heterogeneity further complicates the analysis, highlighting the importance of studying these processes first in a solution phase.[201]

In this work, photophysical processes were studied in two monomeric TDPP molecules, terminal-functionalized with different acceptor groups, benzoxazole (-BOX) and thieno-dicyano (-TCN) (Fig. 3.1).[167] Variation in acceptor group affinity significantly influences the energy levels of molecules, leading to a pronounced red shift extended into the NIR region. Altering the steric hindrance imposed by various end groups changes the molecular geometry, and the intermolecular interaction and consequently affects the photophysical properties.[190] To conduct a comparative analysis, steady-state and ultrafast transient absorption spectroscopy techniques were performed on these TDPP derivatives in both chloroform solutions and thin films.

3.1.2 Results and discussion

3.1.2.1 Steady-state spectroscopy and TCSPC

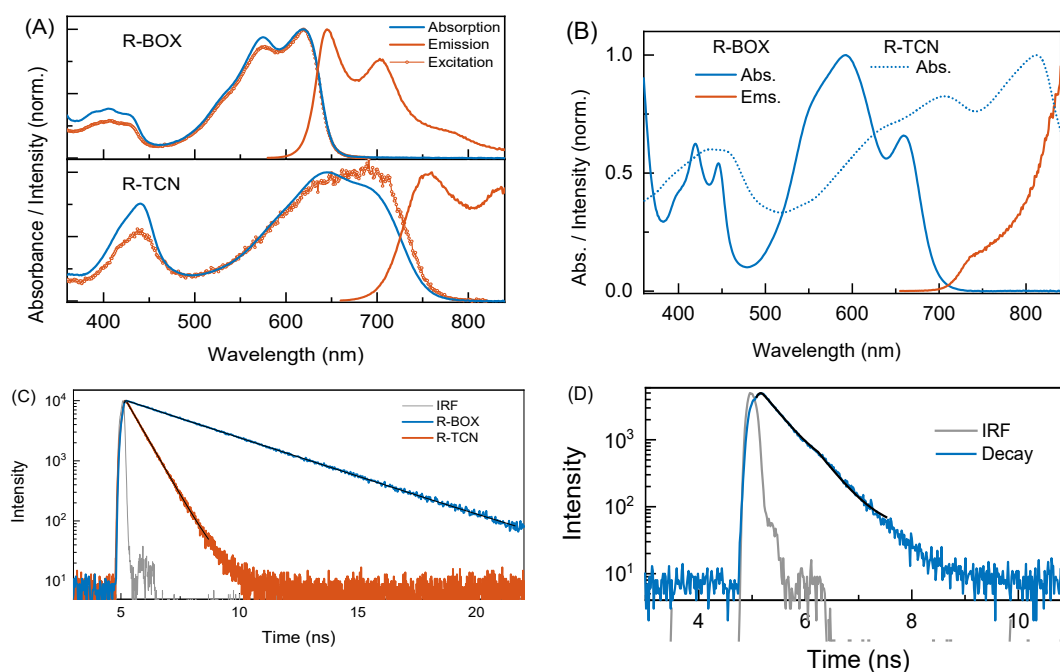


Figure 3.2. Steady-state absorption, emission, and excitation spectra of TDPP derivatives in A) chloroform solution and B) thin film. C) Fluorescence decay of both derivatives in C) solution and D) fluorescence decay of R-BOX in thin film (**Attachment 1**).

Both TDPP derivatives, R-BOX and R-TCN, in chloroform solution and thin-film, display strong absorption in the visible region, indicative of π - π^* type transition that extends to NIR region due to the intramolecular charge transfer between the thiophene donor and DPP acceptor moiety, typical for such conjugated TDPP derivatives.[106,159] In solution, both materials exhibit well-resolved vibronic features, with a similar but mirror spectral profile of absorption and emission spectra. Compared to R-BOX, the R-TCN derivative exhibits a large red-shift in thin film compared to the solution.

Table 3.1. Spectroscopic parameters of TDPPs in solution and thin film (**Attachment 1**).

	TDPP	λ_{abs} (nm) ^b	λ_{ems} (nm)	ϵ (M ⁻¹ cm ⁻¹)	Stokes' shift ^a (cm ⁻¹)	QY %	τ_f (ns)	τ_{TA} (ps)
Solution	R-BOX	620	645	45000	670	52	3.4	4.6, 3.5
	R-TCN	700	755	61000	1400	<20	0.6	5, 700, inf.
Thin Film	R-BOX	660	-	-	-	~5	0.4	-
	R-TCN	810	-	-	-	-	-	-

λ_{abs} - absorption peak; λ_{ems} - emission peak; ϵ - molar extinction coefficient at the maxima; QY - fluorescence quantum yield; τ_f - fluorescence lifetime from TCSPC; τ_{TA} - lifetime from transient absorption; inf. = non-decaying lifetime (infinite).

^a Calculated after converting the spectra to its transition dipole moment representation [202];

^b Lowest energy vibrational shoulder.

Stoke's shift, and shorter fluorescence lifetime compared to R-BOX, are explained by the larger conjugation length and by the presence of the stronger electron-withdrawing -CN groups.[171,203] The overlap of the excitation spectrum with the absorption spectrum confirms the electronic coupling of respective states (Fig. 3.2A).

In thin film, a significant red-shift and loss of vibrational features occur due to the superimposition of intramolecular modes within the broad band, indicating conformational locking and electronic coupling between adjacent molecules.[200] This phenomenon is primarily attributed to improved crystallization during solidification, leading to a delocalization of excited states, which is dependent on sample preparation-induced morphology.[107] In R-TCN, fluorescence emission cannot be measured due to the absorption in NIR region, originating possibly from J-aggregates.[200] In contrast, R-BOX exhibits single exponential fluorescence decay independent of emission wavelength, confirming spectroscopically homogenous thin film, albeit with small excimer-like characteristics. Additionally, the emission lifetime is decreased to 0.4 ns, almost an order of magnitude lower than that of the solution, suggesting the presence of additional nonradiative channels in the system.

3.1.2.2 Femtosecond pump-probe spectroscopy:

The study investigates the photophysical characteristics of TDPP molecules under different excitation wavelengths. In solution and upon excitation at 625 nm, both molecules demonstrate transient absorption (TA) features across the entire probe range (440-820 nm). These features comprise a positive signal representing excited state absorption and negative features corresponding to the ground-state bleach and stimulated emission, with an overall peak at 635 nm and 735 nm in R-BOX and R-TCN respectively, as the weighted sum of two components.[204]

In the R-BOX solution, spectral characteristics remain predominantly stable within a 5 ns window, exhibiting a minor red shift in the stimulated emission region early after photoexcitation. In R-TCN, TA spectra resemble its steady-state absorption spectra, but with significant red shifts and band broadening with increasing time, accompanied by the prominent spectral evolution of the dynamic Stokes shift over the initial 10 – 15 ps, particularly in the stimulated emission region, indicative of excited state processes(Fig. 3.3C-D).[205] Pumping the sample at 625 nm, i.e. with an excess of the vibrational energy, triggers this evolution akin to vibronic processes.[206] Excitation at the red edge of the absorption band (at 725 nm), i.e. at the lower vibrational level results in a relatively smaller evolution, affirming this hypothesis.

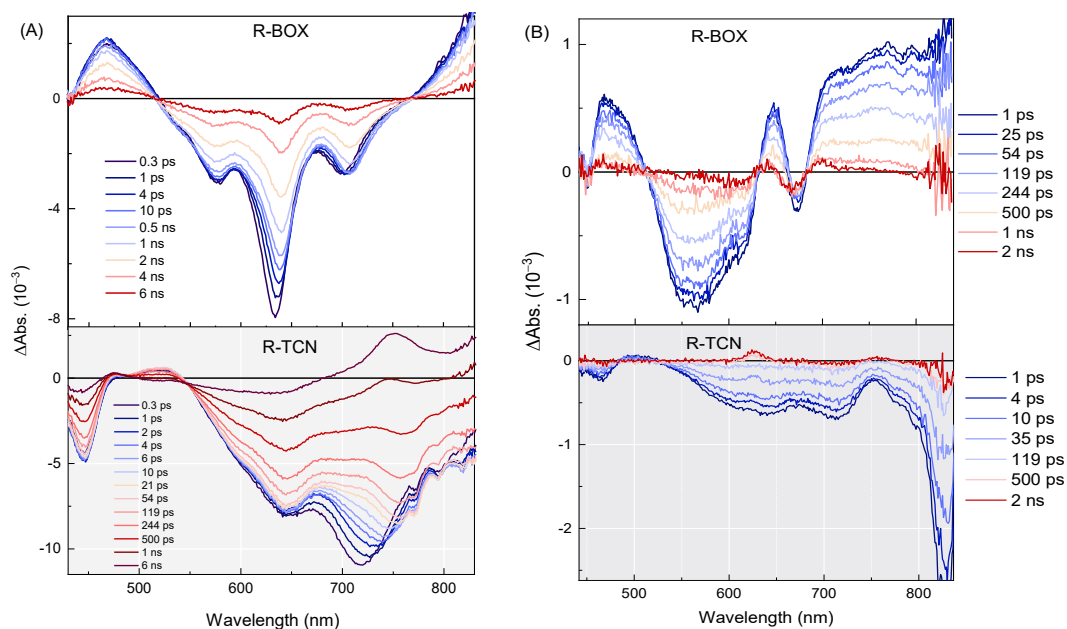


Figure 3.3. Spectral evolution of R-BOX (top panel) and R-TCN (bottom panel) in (A) solution and B) thin film with pump at 625 nm (**Attachment 1**).

A more pronounced effect was in R-TCN compared to R-BOX, showing the structure-dependent nature of the vibrational evolution. Considering the chemical structure, R-TCN incorporates flexible functional groups with an increased rotational degree of freedom while R-BOX features only cyclic units as end groups, potentially imposing higher steric hindrance and limiting structural flexibility. Consequently, it likely facilitates structural alterations upon excitation, transitioning the molecule from its unrelaxed state to a highly stable configuration over time. This study underscores the role of excess vibrational energy on structural dynamics, influenced by molecular flexibility, driving spectral evolution.

In contrast to their behavior in solution, thin-films of both materials display long-time spectral features consistent with the occurrence of triplet states (Fig. 3.3B).[167] Assuming that the long-term transient spectra originate in triplet absorption, exciting at 625 nm and using the pump energy of 18 nJ/ pulse, R-BOX would show ~110 % triplet yield, that varied depending on the pump wavelength and excitation laser beam fluence. For instance, doubling the pump power results in 6 times increase in the yield. When excited in the UV region, namely at 340 - 400 nm, the same laser beam fluence enhanced the yield by 3 to 4 times. The pump-dependent yield, coupled with the calculated value exceeding the theoretical limit, suggests a detrimental impact on the supplied energy.

3.1.2.3 Triplet state and spectral contribution from heat

In order to assess heat dissipation artefacts caused by high-energy pump pulses, [207–209] temperature-dependent steady-state absorption spectra were recorded within the range of 20-35 °C (Fig. 3.4). At high pump density, processes like singlet-singlet annihilation (SSA) can diminish the yield of triplet generation. Additionally, the conical crossover may accelerate this process. These processes potentially lead to unintended heat generation, driven by the excess energy from the excitation to higher excited states.[209,210] We showed that these differences show features very similar to the TA spectra recorded in a longer time-scale, even with a low pump density of 7×10^{17} photon.pulse⁻¹.cm⁻³. These features were observed in all studied TDPP derivatives (not shown in this thesis). Measurements of thin films on sapphire substrates, which offer superior thermal conductivity and, hence, enhanced heat dissipation [167,211] exhibited faster signal recovery in the nanosecond timescale,

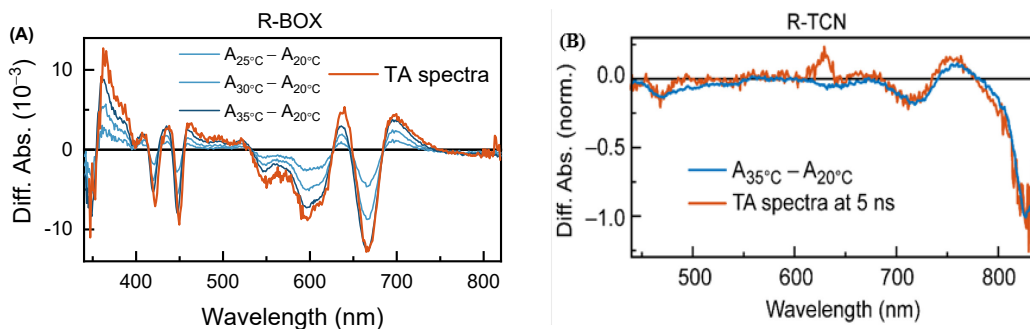


Figure 3.4. The difference in steady-state absorption spectra of **(A)** R-BOX thin film at different temperatures with respect to the spectrum recorded at 20 °C, and **(B)** the difference between steady-state absorption spectra of R-TCN recorded at 35 and 20 °C (blue) compared to the TA spectrum after 5 ns delay (red; scaled to the strongest signal) (**Attachment 1**).

with no significant differences observed in the picosecond range. It suggests that laser-induced heat may potentially obscure signals in longer delay times, where triplet absorption is usually observed. These findings show the complexity of the interpretation of transient spectroscopic data obtained under high pump densities and the importance of mitigating heat-induced artifacts for reliable analysis.

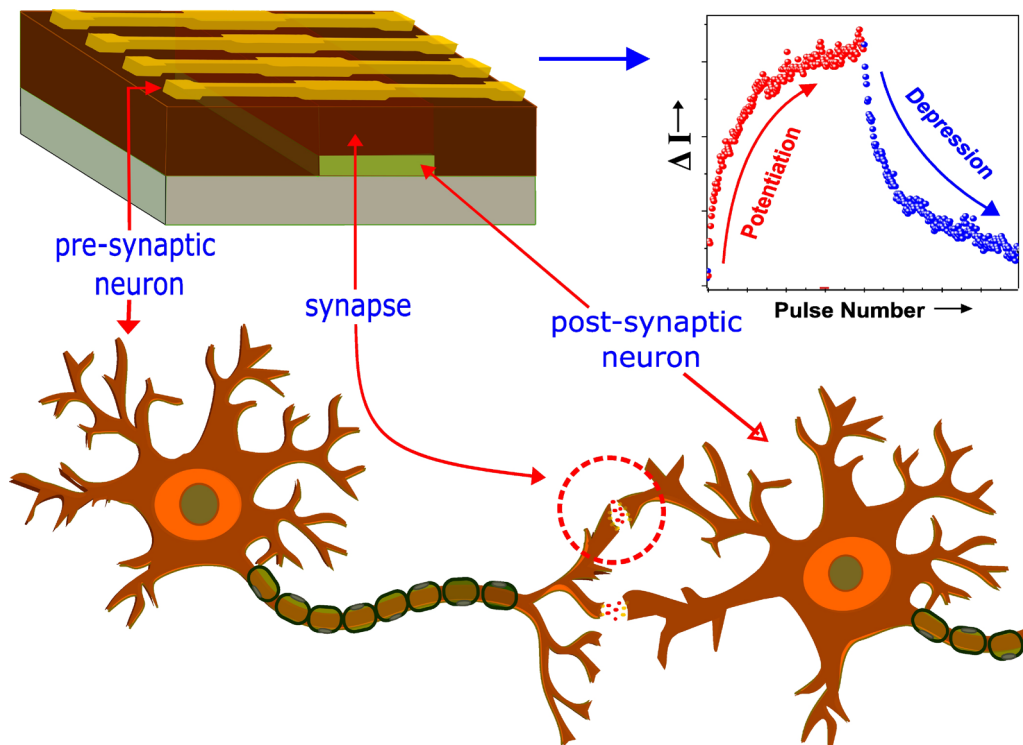
3.1.3 Summary

Two TDPP derivatives under study, R-BOX, and R-TCN, characterized by extended conjugation and differing in electron-withdrawing end groups, exhibited typical DPP spectroscopic features, with R-TCN displaying strong NIR absorption and a higher redshift from solution to thin-film phase. Using ultrafast optical pump-probe spectroscopy, the excited-state phenomena in picosecond to nanosecond timescale were elucidated. R-TCN demonstrated significant structural evolution alongside vibrational effect, converting a notable portion of ~20% of excited singlets to triplets, indicating efficient inter-system crossing. Conversely, in R-BOX, a simplified excited-state dynamic, devoid of intermediate states was studied. In both molecules, long-time signals resembling singlet fission were observed in thin films; however, direct comparison to their temperature-dependent steady-state spectra led to the conclusion that these signals likely originate from laser-induced thermal artifacts. Identifying the triplet state in solution provides valuable insight into engineering DPP molecules, particularly for applications related to triplet states facilitated phenomena.

3.2 Organic memristors: Electronic memory and emulation of synaptic plasticity

This part of the study is based on:

- A. **Y.R. Panthi**, J. Pflieger, D. Výprachtický, A. Pandey, M.A. Thottappali, I. Šeděnková, M. Konefał, S.H. Foulger, *Rewritable resistive memory effect in poly[N-(3-(9H-carbazol-9-yl)propyl)-methacrylamide] memristor*, *J. Mater. Chem. C* 11 (2023) 17093–17105. <https://doi.org/10.1039/d3tc03394e>. (Attachment 2)[87]
- B. **Y.R. Panthi**, A. Pandey, A. Šturcová, D. Výprachtický, S.H. Foulger, J. Pflieger, *Emulating Synaptic Plasticity with Poly[N-(3-(9H-carbazol-9-yl)propyl)methacrylamide] Memristor*, *Mater. Adv.* 5 (2024) 6388–6398 (2024). <https://doi.org/10.1039/d4ma00399c> (Attachment 3) [131].
- C. Pflieger, J.; **Panthi, Y. R.**; Paruzel, B.; Kubáč, L.; Černý, J.; *Prepisovatelný elektronický rezistivní paměťový element*, UŽITNÝ VZOR CZ 32526 U1, 2019, (Attachment 4);[166] and,
- D. The study of memristive effect in composite system of DPP-DTT and PDI, (manuscript under preparation).



3.2.1 Overview of the study

In this chapter, two carbazole-based polymers were investigated, namely poly-[N-(3-(9H-carbazol-9-yl)propyl)methacrylamide] (PCaPMA) and polyvinyl carbazole (PVCa); and a polymer composite comprised of DPP-DTT copolymer with PDI filler in several ratios, namely 1:0, 9:1, 4:1 and 2:1, respectively. First, these materials were used in two-terminal sandwiched structures, demonstrating their functionality as ReRAM. The studied systems exhibited binary resistive switching, leading to nonvolatile electronic memory behavior when applied bias exceeded a threshold limit, V_T . Below V_T , the devices showed multimodal resistance changes, resembling synaptic behavior.[87,131] The ReRAM properties of PCaPMA were compared with commercial polymer, polyvinyl carbazole (PVCa), to understand the role of side groups on memristive behavior. In the case of the DPP-DTT composite, binary resistive switching, nonvolatility, and the ability to mimic synaptic plasticity are dependent on the composite composition. We studied both DPP-DTT and PDI materials are good charge transporting materials,[172] exhibiting pronounced field-effect behavior when incorporated in an active channel of OFETs, & demonstrating high charge carrier mobilities.[169,212] These materials are of significant interest in many organic electronic applications but have received limited attention in memristive studies yet.[213,214]

3.2.2 Results and discussion

3.2.2.1 Material and layer properties

The polymer PCaPMA was synthesized via radical polymerization (Fig. 3.5). The monomer was prepared by a three-step synthesis inspired by the known process of diamine substitution with aliphatic groups.[215] The details of the polymer synthesis, its structural characterization, the fabrication of sandwich structures ITO | PCaPMA | Al or Au, are reported in **Attachment 2**.[87] This polymer ($M_w = 6000$) exhibits good thermal stability with a glass transition temperature $T_g \sim 150^\circ\text{C}$, and excellent solubility in common organic solvents. Due to its high solubility, this polymer forms homogenous, pinhole-free films, as confirmed by AFM and profilometry measurements. It exhibits a semi-crystalline structure confirmed by several relatively wide peaks at X-ray diffractograms (XRD) (included in attachment)

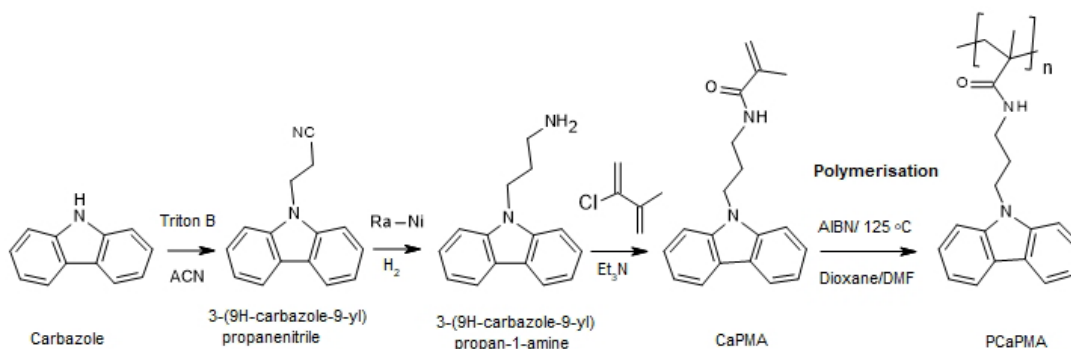


Figure. 3.5: Synthesis of the N-(3-(9H-carbazol-9-yl)propyl)methacrylamide (CaPMA) and its radical polymerization to PCaPMA (**Attachment 2**).

with $2\theta = 6.76^\circ, 12.30^\circ, 19.86^\circ$, corresponding to d-spacing of 13.1 Å, 7.2 Å, and 4.5 Å, respectively, with the last one representing π - π stacking of carbazole groups.[216] XRD peaks in PVCa powder are similar to those in PCaPMA, except for the first (6.76°), albeit narrower and more pronounced, implying more ordered alignment between polymer chains. In powder form, the degree of crystallinity[217] was found to be 51.6% and 40.6 % for PVCa and PCaPMA, respectively. The non-volatile memory behavior was supported by structure stabilization by physically crosslinked hydrogen bonds between the amide and carbonyl groups.

DPP-DTT and PDI exhibit p-type and n-type mobility, respectively, along with their good solubility, stability, and flexibility. XRD recorded on the thin film of all composites (not shown here) showed a similar pattern to pure DPP-DTT, suggesting a homogenous dispersion of PDI molecules within the layer of DPP-DTT without altering its lattice. The layers are polycrystalline, with XRD peaks at $4.6^\circ, 9.0^\circ, 13.1^\circ$, and 17.7° , indicating interplanar distances (d-spacing) 19.4, 9.8, 6.7, and 5.0 Å, respectively.

3.2.2.2 Optical properties

The UV-vis optical absorption and fluorescence emission spectra of PCaPMA and PVCa, dissolved in DMSO and cast as thin films on quartz substrates, are presented in Fig. 3.6, normalized to their respective maxima. Only vibronic peaks of the lowest electronic transition in the spectral region above 300 nm are shown, originating from the π - π^* ($^1A - ^1L_b$) transition of carbazole chromophores, aligned with the short axis of the carbazole molecule.[87,218] Compared to PVCa, the polymer PCaPMA

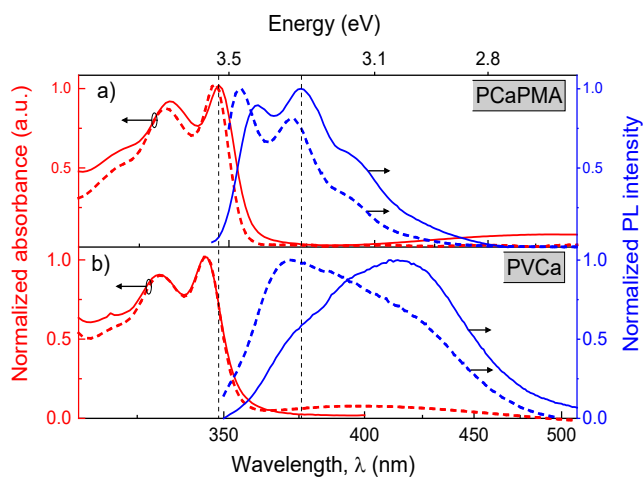


Figure. 3.6: UV-vis absorption (red) and emission spectra (blue) of a) PCaPMA and b) PVCa in thin films (solid lines) and solutions (dashed-lines) (**Attachment 2**).

displayed a slight spectral shift towards lower energy, with a minimal shift from solution to solid phase. The fluorescence emission spectrum of PCaPMA demonstrated mirror symmetry with absorption spectrum and a smaller Stokes shift, attributed to a smaller mutual on-chain chromophore interaction. The fluorescence peaks correspond to vibronic structure of the $\pi-\pi^*$ optical transitions of carbazole monomers, notably lacking excimer emission found in PVCa.[219,220]

In the solid state, PCaPMA exhibited an increased Stokes shift and a more intense 0-1 band, indicating structural changes in the excited state. PVCa in dimethyl sulfoxide solution showed intense monomeric emission and weak mutual interaction between chromophores, which intensified in the solid state due to sandwich-type mutual interactions between carbazole groups.[220] PCaPMA's spectra lacked this excimer emission due to its less ordered structure. Differences in optical spectra between PCaPMA and PVCa in thin layers were attributed to different packing of carbazole molecules rather than electronic effects observed in alkyl-substituted carbazoles. Higher flexibility of PCaPMA and bulky side chains decreased chromophore concentration, lowering the probability of excimer formation.

3.2.2.3 Electrochemical study

The cyclic voltammograms of PCaPMA, PVCa, DPP-DTT, and PDI thin films deposited on ITO-coated glass substrates were recorded using ITO as a working electrode, Pt wire as a counter electrode, and Ag | AgCl rod as a reference electrode. Acetonitrile solution of $n\text{-Bu}_4\text{NPF}_6$ was used as an electrolyte. The CV curves,

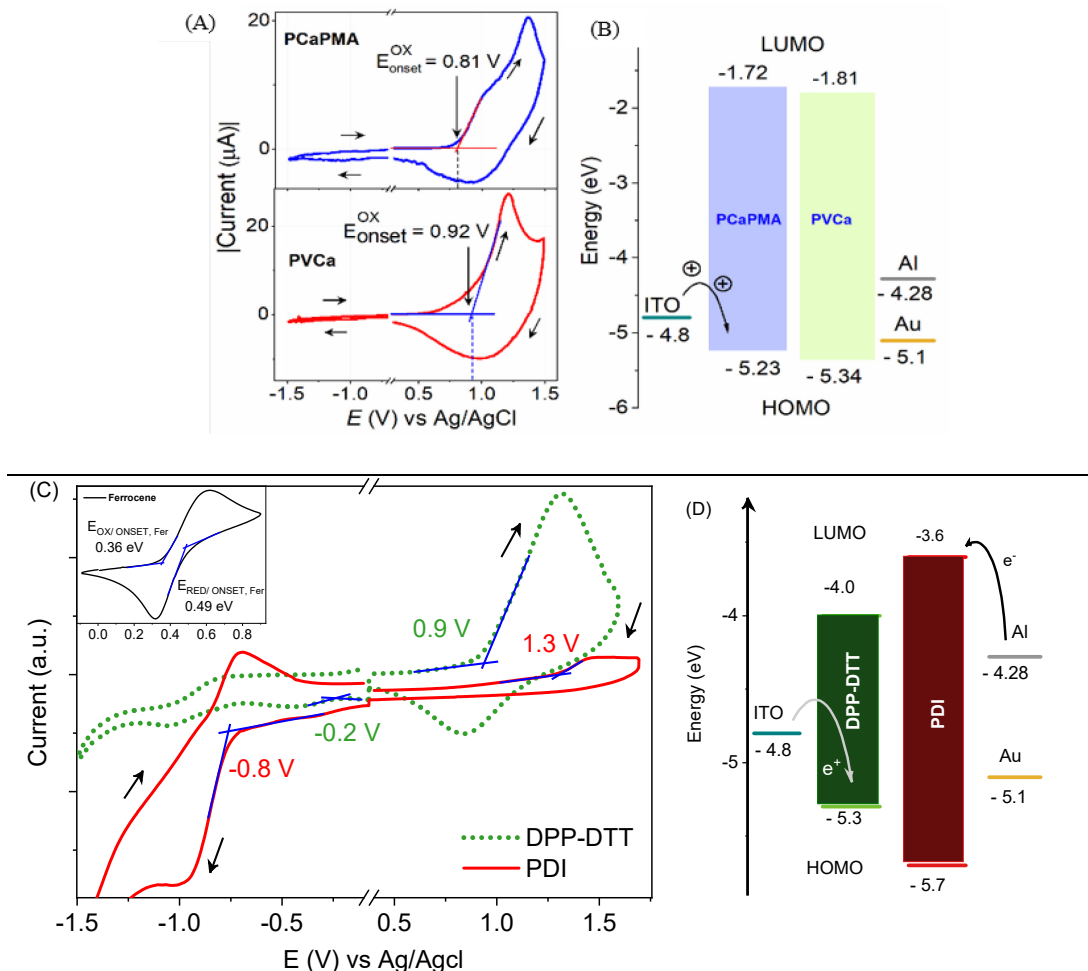


Figure 3.7: Cyclic voltammogram (CV) of A) PCaPMA and PVCa and C) DPP-DDT and PDI films cast on the ITO | glass; B) and D) energy diagrams of materials and electrodes. Scan rate 20 mV/s sweep direction indicated by arrows (**Attachment 2**).

recorded with a scanning rate of 20 mV/sec, are depicted in Fig. 3.7A. In PCaPMA, the anodic scan exhibits an oxidation peak at ~ 1.37 V with an onset at about 0.81 V, while in PVCa, the onset occurs at ~ 0.92 V. Similarly, DPP-DDT displays a distinct oxidation peak, whereas PDI exhibits a more dominant reduction peak. The energy levels were then calculated using:

$$E_{\text{LUMO}} = -[E_{\text{RED_ONSET}} - E_{\text{RED_ONSET, Fer}} + 4.8] \quad (3.1)$$

$$E_{\text{HOMO}} = -[E_{\text{OX_ONSET}} - E_{\text{OX_ONSET, Fer}} + 4.8] \quad (3.2)$$

Here, $E_{\text{OX_ONSET}}$ and $E_{\text{RED_ONSET}}$ denote the onset oxidation and reduction potential, respectively. The onset potentials of the ferrocene/ferrocenium ion couple, $E_{\text{OX_ONSET, Fer}}$ and $E_{\text{RED_ONSET, Fer}}$, respectively, were measured against the Ag|AgCl reference electrode under the same conditions as for the tested organic materials.

For DPP-DTT, the energy positions of the LUMO and HOMO were determined to be -4.0 and -5.3 eV respectively, resulting in the energy bandgap $E_g = 1.3$ eV. For PDI, the LUMO and HOMO were observed to be -3.6 and -5.7 eV with the bandgap $E_g = 2.1$ eV. The energy values obtained in our experiment are consistent with previous literature reports for DPP-DTT and PDI derivatives.[221–223] The HOMO levels of PCaPMA and PVCa were determined to be -5.23 and -5.34 eV, respectively. In these polymers, the LUMO positions could not be measured electrochemically, they were derived from the respective HOMO positions and the bandgap obtained from the Tauc plot of the optical absorption spectra. Using this approach, the LUMO positions of -1.72 eV and -1.81 eV, were obtained for PCaPMA and PVCa, respectively.

3.2.2.4 Electrical characteristics

The DC current-voltage (I-V) characteristics of sandwich devices containing an active layer made of PCaPMA, PVCa, and DPP-DTT: PDI composites are shown in Fig. 3.8. The measurements were conducted at room temperature in the dark, and in a vacuum, pressure 10^{-4} Pa.

Bistable conductance

Current-voltage characteristics were measured with voltage sweeps ranging from 0 to $\pm U_{max}$, and back to 0 V as shown in Fig. 3.8. All devices exhibited bistable switching behavior between a high resistance state (HRS) and a low resistance state (LRS).

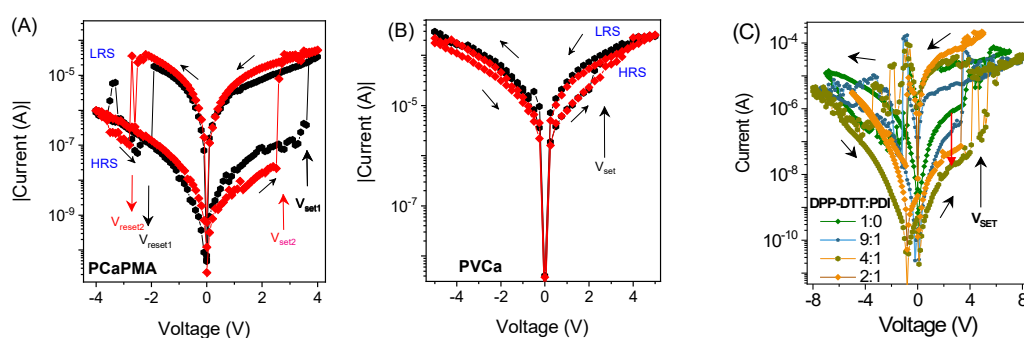


Figure 3.8: Current-voltage (I-V) characteristics illustrating bi-stable switching of A) ITO | PCaPMA | Al, B) ITO | PVCa | Al and C) ITO | DPPDTT: PDI composites | Al, in a sandwiched layer. HRS and LRS stand for high- and low-resistance states, respectively, V_{set} and V_{reset} denote the threshold voltage in which the resistance changes to LRS and HRS, respectively (**Attachment 2**).

Compared to PVCa, polymer PCaPMA, and composite layers displayed bistable conduction, exceeding two orders of magnitude in current in LRS compared to HRS. With ITO grounded and voltage sweep in a positive direction, the current increased from the HRS to the LRS when the applied voltage reached a threshold value (V_T). In some cells, the setting and resetting processes were continuous, leading to negative differential resistance (NDR), particularly at fast scan rates. For most of the devices with 100 nm thick active layer, V_T ranged from 2 to 5 V.

In most of the samples, setting a compliance limit (I_{CL}) proved to be beneficial to prevent any possible electrical breakdown. PCaPMA with Au TE had higher OFF-state current and lower V_T corresponding to a lower energy barrier between the HOMO level of PCaPMA and the work function of gold, compared to ITO (Fig. 3.7 A). In the composite systems, no direct dependency of V_T was observed with varied PDI content; however, the value of OFF-state current decreased with the increased PDI content. The dynamic switching characteristics of ITO | PCaPMA | Al (Fig. 3.9A) were tested with ± 5 V as setting and resetting voltage, respectively, and 0.5 V applied for reading the device conductivity in both HR and LR states. The devices exhibited electrically stable responses over 200 write-read-erase-reread (WRER) cycles, with a high degree of reproducibility. Moreover, the devices remained stable for hours when the current was

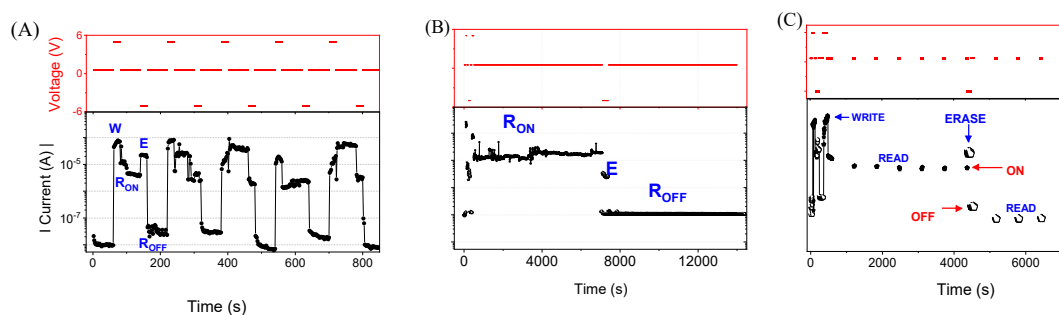


Figure 3.9: Testing the memory behaviour in ITO | PCaPMA | Al, with A) dynamically repeated write-read-erase-reread (WRER) cycles, B) persistence of both ON and OFF states under constant applied voltage of 0.5 V, and C) volatility test in different time intervals without power supply in between. Voltage pulses are shown in red (top panels), and the corresponding current response is in black (bottom panels). W: writing (setting), E: erasing (resetting), R_{ON} and R_{OFF} : reading in the ON and OFF state respectively (**Attachment 2**).

measured in both ON and OFF states with a continuously applied reading voltage of 0.5 V, keeping the current ON/OFF ratio higher than 100.

Multimodal conductance change: Mimicking neuro-synaptic plasticity

Voltage-induced resistance changes were analysed via current-voltage (I-V) characteristics of ITO | active layer | Au or Al devices, simulating synaptic effects of action potentials. Trigger pulses (10 ms, 500 mV) were used to induce conductance modulation, monitored by -50 mV read pulses of 50 ms duration (Fig. 3.10A). These findings align with the magnitudes of action potential seen in the human brain.[144,224] When repeated pulses were applied to TE, the current increased continuously, signifying the long-term potentiation of the device. As the conductance increase was caused when the bias was applied to the TE, this electrode is considered to be an analogy of the pre-synaptic terminal, and the current is referred to as an excitatory post-synaptic current (EPSC).[14,225] Conductance increase was observed

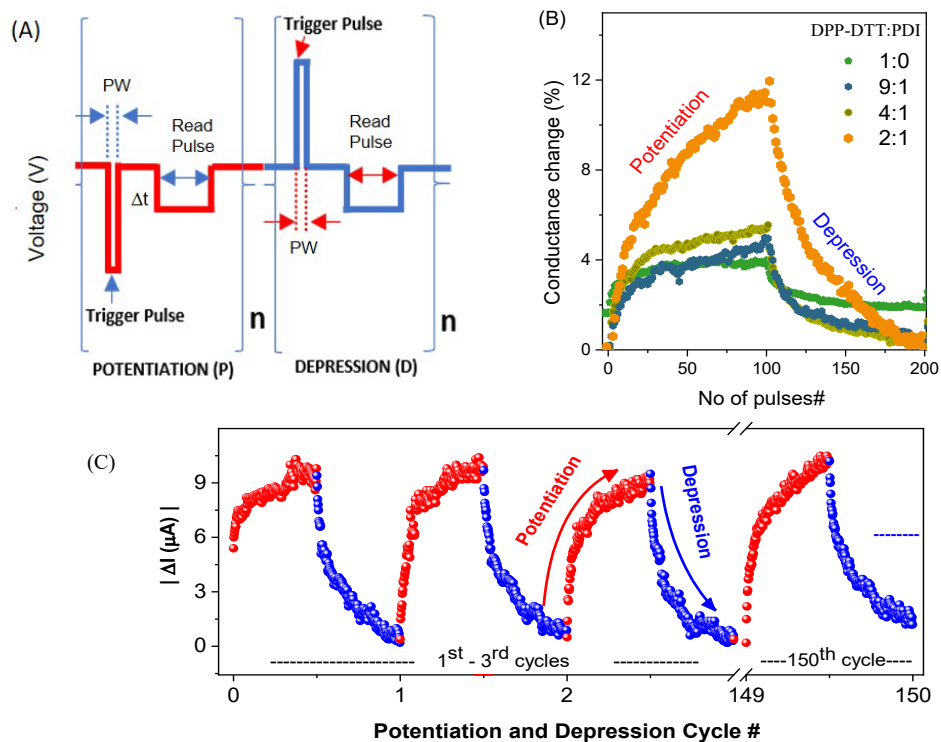


Figure. 3.10. A) Schematics of pulse setup for the measurement of analog changes in device conductance, B) Potentiation/depression (P/D) cycle showing conductance change in ITO | DPP- DTT: PDI composite | Au device with 100 consecutive DC pulse scans of each polarity and C) 150 P/D cycles in ITO | PCaPMA | Au device illustrating good reproducibility (**Attachment 3**).

over 200 consecutive pulses, representing a synaptic potentiation. After 100 pulses the current started to saturate. It is analogical to synaptic properties known as long-term potentiation, indicating the saturation of learning.[226] Reversing the polarity of pulses caused the current decrease, like the synaptic depression) in neuronal synapses. In the ITO | PCaPMA | Au device, the conductance changes were found to be reproducible over 150 cycles (Fig. 3.10C) at room temperature without a marked degradation.

In devices with the composite (DPP-DTT: PDI) active layer, similar synaptic properties were observed. Higher PDI content (4:1 or 2:1 ratios) led to a more pronounced plasticity. In either system, no significant signal degradation was noted over 100 measured cycles, confirming the good reproducibility and stability of the devices.

With both, PCaPMA and composite active layers, the changes were more prominent in the case of Au TE. With Al TE, devices had similar but much smaller changes. Repeated cycles displayed consistent behavior, reaffirming the memristor's potential to emulate cognitive processing akin to neural synapses. The potentiation/depression was observable even with trigger pulses ± 100 mV. With an increased trigger pulse the current changes were bigger, while the longer time delay between pulses induced smaller current changes. The current change usually tends to saturate after 100 pulses. These overall effects mirror the functionality of biological synapses.[227]

Memory transition and associative learning

As illustrated in Fig. 3.11 A, stimulating the ITO | PCaPMA | Au device with trigger pulses at a frequency below 1 Hz, the conductance relaxes to its initial levels between subsequent triggers, akin to short-term potentiation (STP), resembling memory fading after weak stimulation in biological systems. Triggering at a frequency above 1 Hz, each subsequent stimulation partially preserves the conductance from the previous stimulation, mimicking long-term potentiation (LTP) and leading to a transition from short-term memory (STM) to long-term memory (LTM). This transition occurs progressively with increasing frequency, facilitating rapid LTP evolution.

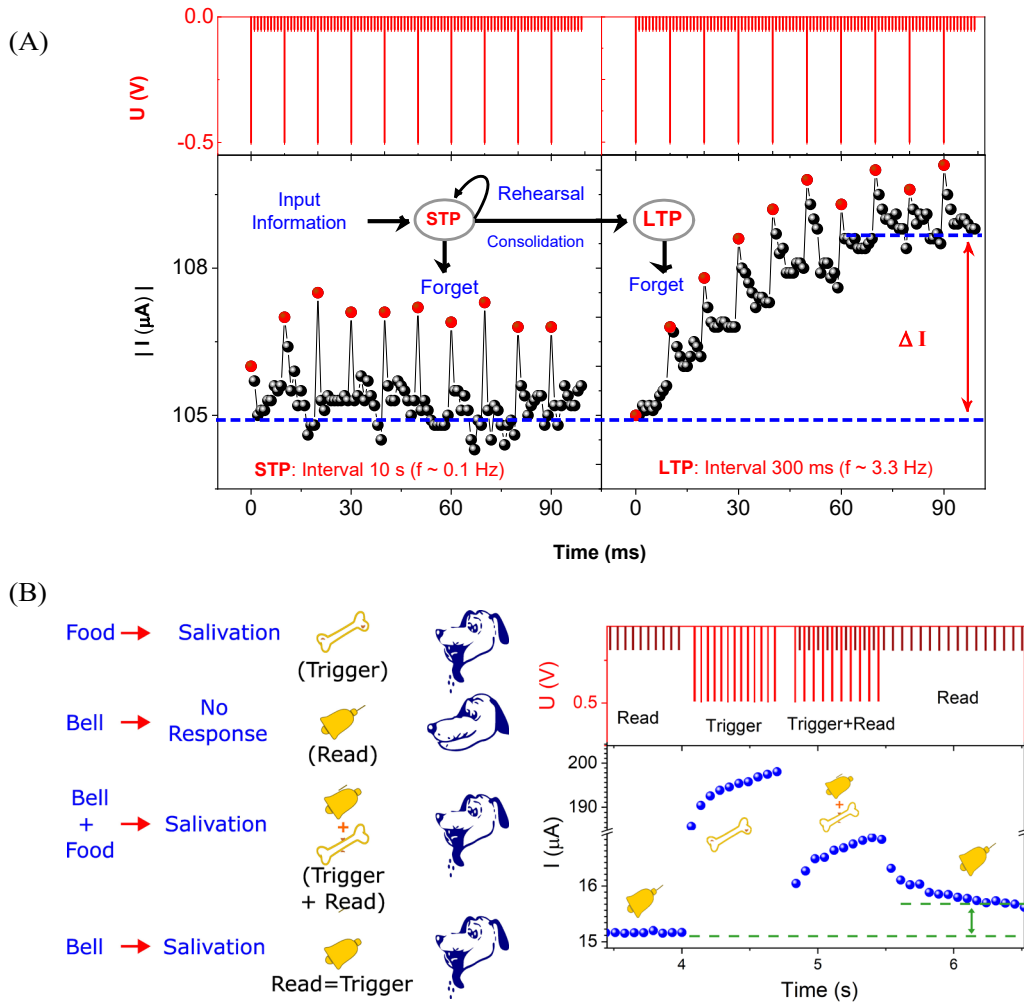


Figure. 3.11: A) Progression of conductance changes during stimulation by trigger pulses at different frequencies: 0.1 Hz (left) and 3.3 Hz (right). The inset shows a diagram of learning and memory retention during the rehearsal process.[228] B) Schematic of the Pavlovian learning algorithm utilized to stimulate dog, and B) experimental observation in ITO | PCaPMA | Au device with the voltage trigger as conditioned stimulus (**Attachment 3**).

exceeded biological level but the effects were observable also at lower amplitudes, although with a reduced signal-to-noise ratio. These results underscore the potential of these devices to emulate memory processes and mimicking learning, required for AI development.[25,229]

Paired-pulse facilitation/depression and spike-timing-dependent plasticity

Paired-pulse facilitation/depression (PPF/PPD) analysis aims at the understanding of short-term plasticity, explaining temporal dynamics of

conductance changes in response to dual stimuli. PPF represents a phenomenon observed in most chemically transmitting synapses, where the second of two closely followed excitatory pulses induces an enhancement in the amplitude of the post-synaptic response. Conversely, PPD occurs when the second stimulus diminishes the response, indicating a weakening of synaptic transmission.

Stimulation of the conductance was performed using a pair of trigger pulses with randomly varying inter-spike time interval Δt . A_1 and A_2 denote the current monitored by the reading pulses after 5 ms following the first and second stimulation pulse, respectively. For PPF, the amplitude A_2 was enhanced compared to A_1 , while A_2 was suppressed for PPD. This change defines the PPF/D index, which was calculated for 45 pulse pairs with randomly varying intervals, Δt obtained by using the following equation:[230]

$$\text{PPF/D index (\%)} = \frac{A_2 - A_1}{A_1} \times 100\% \quad (3.3)$$

The dependence of the PPF/D index on Δt is shown in Fig. 3.12.A. Before each PPF/D measurement, the sample was left to relax for 5 min without any excitation. Decreasing the interval between pulses enhanced the memory effect of the pre-spiking pulse on the subsequent one. The obtained values were then fitted using the double exponential function, following the equation:

$$\text{PPF/D index} = C_0 + C_1 e^{-\Delta t/\tau_1} + C_2 e^{-\Delta t/\tau_2} \quad (3.4)$$

where τ_i are the decay times and C_i are the corresponding weight constants of two processes determining the decay profile. The short-term and long-term time constants are obtained to be 79 and 730 ms for PPF and 35 and 280 for PPD. These time constants are close to those observed in biological systems.[231] Additionally, spike-timing dependent plasticity (STDP) shows the plasticity features of inter-neuronal connections, based on the sequence and temporal separation, Δt , between pre-synaptic and post-synaptic spikes (Fig. 3.12B).[232] STDP is also an activity-driven mechanism that constitutes an important principle of competitive Hebbian learning, serving as a basis for cognitive learning.[233] The triggers were applied to Au and ITO electrodes, representing the pre-synaptic and post-synaptic neurons, respectively, (inset of the figure) and the conductance change was monitored by reading pulse after two different

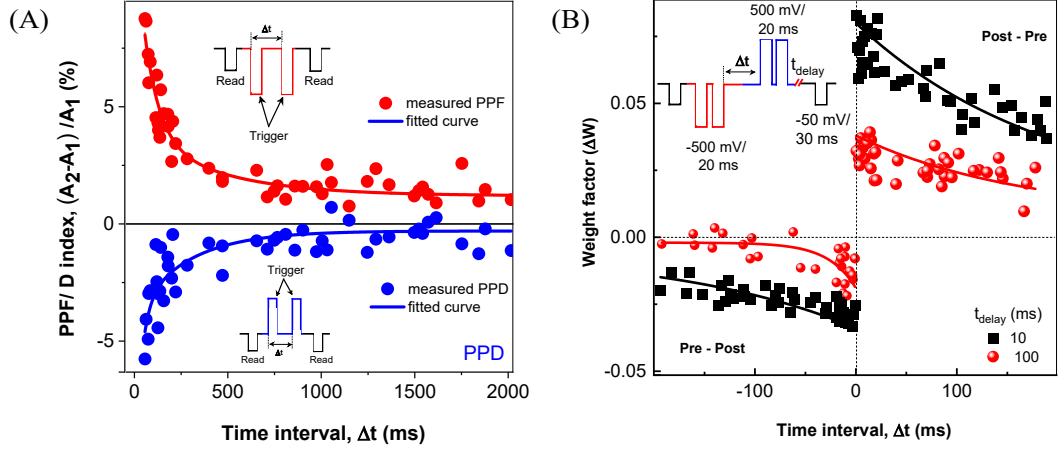


Figure. 3.12: A) Dependence of PPF (red symbols) and PPD (blue symbols) index on randomly varying inter-spike time interval Δt . Solid lines - double exponential fit using Eq. 3.4. B) Dependence of the synaptic weight ΔW on the time interval Δt between the pre- and post-synaptic spikes for two different time delays: $t_{\text{delay}} = 10$ ms (black squares), and $t_{\text{delay}} = 100$ ms (red circles). Full lines – data fitted using Eqn. 3.6 Inset: trigger/read pulse sequences used for measurements (**Attachment 3**).

time delays, $t_{\text{delay}} = 10$ ms and 100 ms, respectively, for both spike pair orders. An increase in conductance ($\Delta G > 0$) was observed for $\Delta t > 0$ indicating the strengthening of the synaptic connection, and a weakening of synapse, i.e. reduction in conductance, $\Delta G < 0$, for $\Delta t < 0$. The relative synaptic weight change (weight factor, ΔW) was then calculated using the equation:[232]

$$\Delta W = \frac{\Delta G}{G} \frac{(G_2 - G_1)}{G_1} \quad (3.5)$$

Here, G_1 and G_2 denote the conductance after and before pre- and post-spiking pairs. The experimentally measured weight factors were fitted using the eqn:

$$\Delta W = \begin{cases} A_+ e^{-|\Delta t| \tau_+} + W_0, & \text{for } \Delta t > 0 \\ A_- e^{-|\Delta t| \tau_-} + W_0, & \text{for } \Delta t < 0 \end{cases} \quad (3.6)$$

where, W_0 denotes the asymptotic value, as the weighting factor was not fully normalized, Δt is the interval between pre- and post-synaptic spikes pairs, with A_+ and A_- representing predetermined scaling factors, and τ_+ and τ_- denote the relaxation time constants. For $\Delta t > 0$, the relaxation time τ_+ was extracted as 190 ms and 160 ms, for the delay time 10 and 100 ms, respectively. For $\Delta t < 0$, relaxation times, τ_- , were obtained as 180 ms and 27 ms. This pattern correlates

well with the asymmetric Hebbian Learning rule, whereby the positive time delay induces LTP, and the negative one causes LTD of the synapse.[130,227]

3.2.2.5 Working mechanisms

Study of conformational relaxations by impedance spectroscopy

The impedance spectra in carbazole-based polymers, PCaPMA and PVCa, were found to exhibit three distinct relaxation processes, labelled as α -, β - and γ - relaxations, best seen in the loss modulus spectra (Fig. 3.13A). The low-temperature γ -relaxation appeared only in PCaPMA, and it was attributed to the rotational freedom of the pendant carbazole groups due to the flexible spacer [87,234]. The α - and β -relaxation were found at high-temperatures, and they were correlated with the glass transition temperature and side chain conformation around the C-C bonds, respectively. A merging of $\alpha\beta$ -relaxation occurred at even higher temperatures.[87,142] All relaxations originate in thermally activated processes.[235]

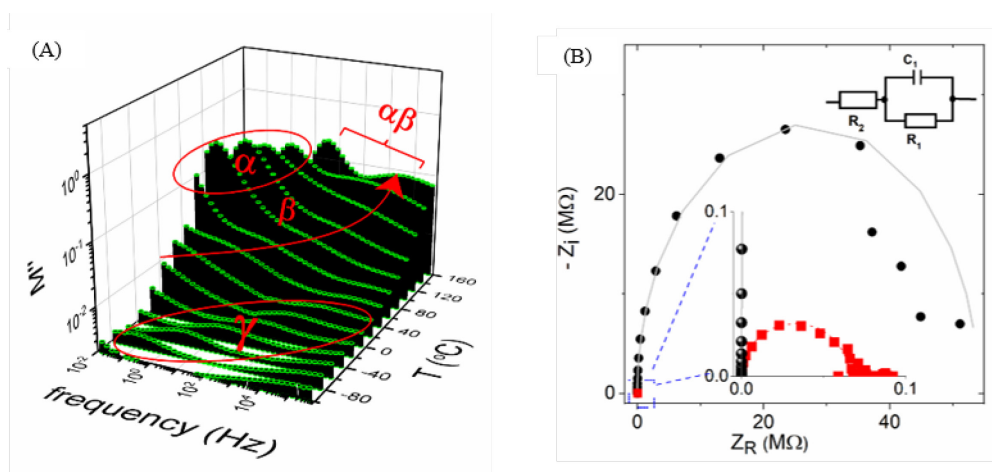


Figure 3.13: A) Temperature dependence of the loss modulus M'' spectra in PCaPMA, illustrating α -, β - and γ - relaxations B) Nyquist plot of the complex impedance of the pristine sample (black circles), and of sample in ON state (red squares) in the zoomed view of the high-frequency region. Experimental points were fitted using an equivalent circuit shown in the inset of Figure 3.13B. Fitting parameters: $R_2 = 5.4 \cdot 10^7 \Omega$ (OFF state), $R_2 = 6.5 \cdot 10^5 \Omega$ (ON state); $C = 1.2 \cdot 10^{-9} F$ and $R_1 = 80 \Omega$ for both ON and OFF states (**Attachment 2**).

The Nyquist plot (Fig. 3.13B), illustrates the real and imaginary part of the impedance on a fresh sample (ITO | PCaPMA 80 nm | Al) in the OFF state, and after applying the DC voltage sweep from 0 V to +5 V, turning it to the ON state. Notably, only the real part of the impedance has been changed between the two conducting states of the device before and after switching, with almost the same capacitance and serial resistance R_1 . This indicates that interface electrode effects or injection barrier change, caused by possible Al_2O_3 formation [236] do not impact the switching mechanism. Similarly, the unchanged capacitance between pristine and voltage-loaded samples suggests that no dielectric breakdown occurred in the active layer.[237]

Role of space charges and traps

The nearly insulating nature of PCaPMA, owing to its saturated backbone, results in minimal free charge carrier concentration in thermal equilibrium, leading to space charge-limited current (SCLC).[51,80] This SCLC is predominantly influenced by localized states [87,131] within the layer, making it trap-controlled.[4] A representative band diagram of the ITO | PCaPMA | Au or Al devices (Fig. 3.5A), illustrates the adjustment of the energy barrier at the metal-organic interface. Carriers are injected through a smaller Schottky barrier, particularly via gold ($\phi = 5.1$ eV) or ITO ($\phi = 4.8$ eV), electrode.[238] The injected carriers are captured in traps.[239] Once the trap DOS is filled with injected carriers, SCLC becomes trap-free, leading to a steep increase in conductance. With shallow traps filled predominantly in low voltage regions, an analog effect can be observed, exhibiting the trigger pulse rate-dependent device conduction.[240]

Experimental confirmation of SCL transport is evidenced by I-V characteristics of ITO | PCaPMA | Al device, in double logarithmic scale (Fig. 3.14A). The low-voltage linear region in the OFF state exhibits typical Ohmic conduction $I \propto V^m$ with $m = 1$, while trap-controlled SCLC is dominated at higher voltage, transitioning the device to the ON state at a specific setting voltage of V_T where the quasi-Fermi level shifts above the trap energy levels, leading to the trap-free SCLC, characterizing the LR state.[4,80,137] The device exhibits nonvolatile memory behavior, retaining its state even without applied voltage. Reverting to its OFF state requires reverse biasing or prolonged disconnection from power to eliminate previously formed space charges and to make the trapping sites empty.[241]

The hypothesis was further validated by the fitting of I-V characteristics in a linear scale (Fig. 3.14B). Various CT mechanisms were explored, including SCLC, or SCLC with field-dependent mobility (SCLC-F), along with Ohmic or Schottky contact behaviour. Considering field-dependent mobility in analogous carbazole-based polymers,[242] SCLC-F model was chosen, typical for dispersive hopping transport,[81] and the Ohmic dependence:[243]

$$I = A \frac{9}{8} \mu \epsilon_i \frac{V^2}{d^3} \exp\left(\frac{0.891}{kT} \left(\frac{e^3 V}{\pi \epsilon_i d}\right)^{1/2}\right) + B V \exp\left(-\frac{C}{T}\right) \quad (3.7)$$

Here, T represents room temperature (298 K), μ the hole mobility at a low electric field ($3 \times 10^{-6} \text{ cm}^2 \text{ V}^{-1} \text{ s}^{-1}$, the value taken from the similar polymer material, [242]) $\epsilon_i = 3.1$ is the relative permittivity, and d is the film thickness (100 nm in this case). A , B , and C are constants independent of voltage and temperature.

These analyses suggest that the RS mechanism stems from the trapping/detrapping process. However, the device's non-volatility cannot be solely attributed to thermally activated detrapping from the 0.33 eV trap depth. Another stabilizing mechanism likely involves the reorientation of carbazole groups in the side chains by an applied voltage, aiding charge transfer between adjacent chromophores.[244–246] The conductance state is further stabilized by the hydrogen

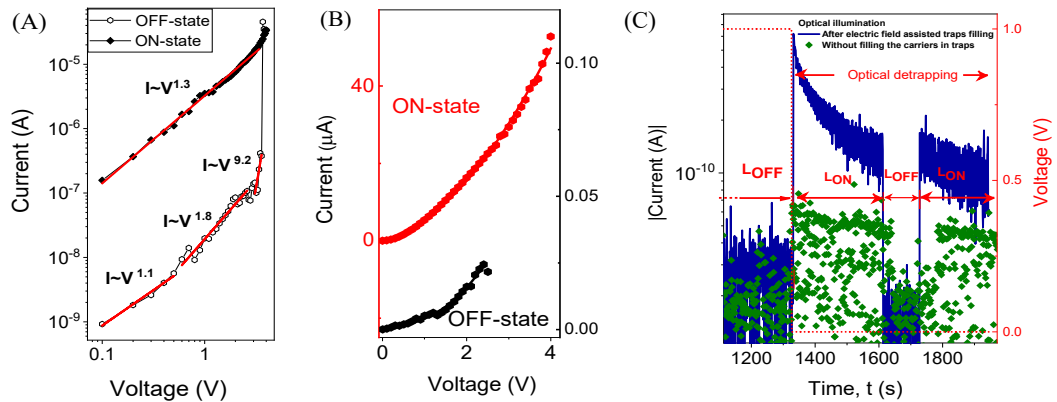


Figure 3.14: Fitting of the A) Linear & B) log-log I-V cycle of ITO | PCaPMA | Al device, and C) Photodetrapping process of trapped charges in same device configuration after biasing at +1 V (blue curve) and without pre-biasing (green dots). Red dots indicate the applied bias. The illumination was taken through the glass | ITO faces using Xe-lamp equipped with a 300-400 nm bandpass filter (light intensity $400 \mu\text{W}/\text{cm}^2$). L_{ON} and L_{OFF} show the illumination ON and OFF, respectively (**Attachment 2**).

bonds formed between amide and carbonyl in the linker.

Trap density was calculated using an electric field-induced trapping and optical detrapping experiment on ITO | PCaPMA | Al device following the methodology outlined by Q. Chen et al., [247] Initially, traps were charged by applying +1 V to the ITO electrode for a specific duration. Subsequently, we recorded the current under short-circuit conditions while illuminating the sample with light in the 300-400 nm region from a Xenon lamp equipped with a thermal and bandpass filter. The discharge current followed a stretched exponential decay $I = I_0 \exp[-(t^a)/\tau]$, with parameters $a = 0.5$, $\tau = 6.8$ s, until the traps were emptied. No current was observed under the same illumination conditions without prior voltage application, confirming that the current originates from the trapped charges. Since the current was detected only within wavelength range where the carbazole chromophores absorb light, it suggests the removal of the space charge trapped in the localized energy levels within the bandgap by intrinsically photogenerated free charges in the polymer. Integrating the discharge current, we estimated the stored charges in the 80 nm thick film to be approximately 10^{18} charges/cm³. The persistence of discharge current, which was unchanged even after interruption of illumination for about two minutes, indicates charges trapped in deep levels with a low escape rate. The fully reversible charging/light-induced discharging cycle strongly supports the trapping/detrapping resistive memory mechanism.

Redox phenomena

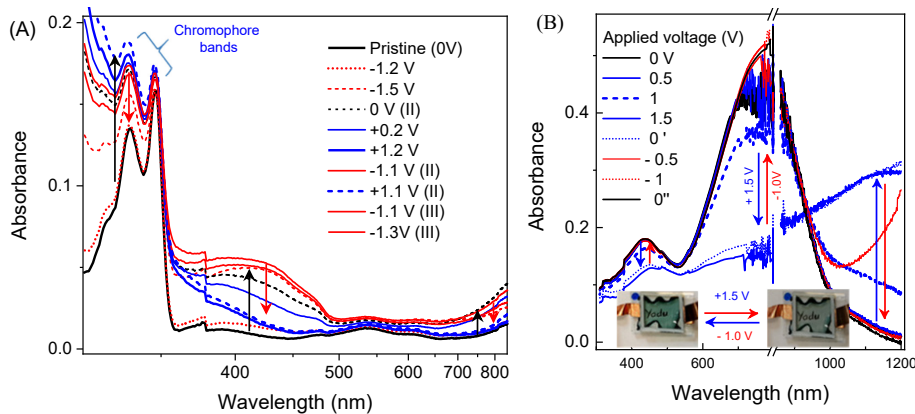


Figure. 3.15: UV-vis spectra *in-situ* voltage of ITO | active layer | gel-electrolyte | ITO device with A) PCaPMA and B) DPP-DTT as an active layer.

Fig. 3.15 presents *in-situ* voltage UV-Vis spectra (spectro-electrochemical spectra) during electrochemical cycling of the ITO | active layer | gel-electrolyte | ITO sample (device structure shown in the photograph in the inset of Fig. 3.15 B). During oxidation, the spectra demonstrated a notable increase around the main absorbance peaks. In PCaPMA, an increased absorbance of bands centered at 333 nm and 346 nm was observed, correlated with the oxidation of carbazole.[282] The process was found reversible.

In films of DPP-DTT (and DPP-DTT molecularly doped with PDI, not included here), the redox processes are visible at around 800 nm, changing colours between colourless and green, within ± 1.5 V (Fig 3.15B). The redox changes were completely reversible. At higher bias voltage (+1.5V), a new transition in the electronic absorption spectrum around 1200 nm appeared, which could be attributed to the presence of polarons or bi-polarons in the film.[248] The process was again reversible. These oxidation and reduction phenomena correlate well with the conductivity changes in the memristor. Such successive redox processes are also important in electrochromic applications.

Field-effect behavior in composite system

The DPP-DTT, characterized by its donor (D)–acceptor (A) based backbone of fused ring moieties (thienothiophene-TT and diketopyrrolopyrrole-DPP), exhibits excellent π - π stacking and high carrier mobility.[173,249,250] The field-effect characteristics were analysed using a bottom-gate bottom-contact (BGBC) structure with the spin-coating active layer on a pre-fabricated OFET substrates (Fig. 2.6A).[176] Annealing the DPP-DTT layer from 70 to 140°C increased mobility from 0.06 to 0.1 $\text{cm}^2\text{V}^{-1}\text{S}^{-1}$.

The introduction of PDI resulted in a higher density of traps or scattering centers, reducing I_{SD} , mobility, and overall conductivity by almost two orders of magnitude (Fig. 3.16 B-C). The n-type PDI additive (Fig. 3.16C) potentially created structural defects and localized electronic polarization, introducing both static and dynamic disorder.[25,251,252] However, the HOMO energy level of PDI lies below that of DPP-DTT (Fig. 3.7B), suggesting that it is an inactive state for charge carrier trapping, rather acting more as a scattering centre reducing the charge carrier mobility.[70]

In our system, an increased concentration of PDI molecules could potentially act as shielding agents around the crystal boundaries of DPP-DTT, influencing the transport of carriers. The molecular dispersion of PDI without any phase separation (confirmed with the XRD curve) may create an electrostatic shielding in the intermolecular interaction of DPP-DTT molecules, affecting their electronic coupling.[253] The decrease in I_{SD} in transfer characteristics and consequently the mobility may be attributed to these effects. Additionally, the increased concentration of PDI has led to a significant increase in V_T by more than an order of magnitude.

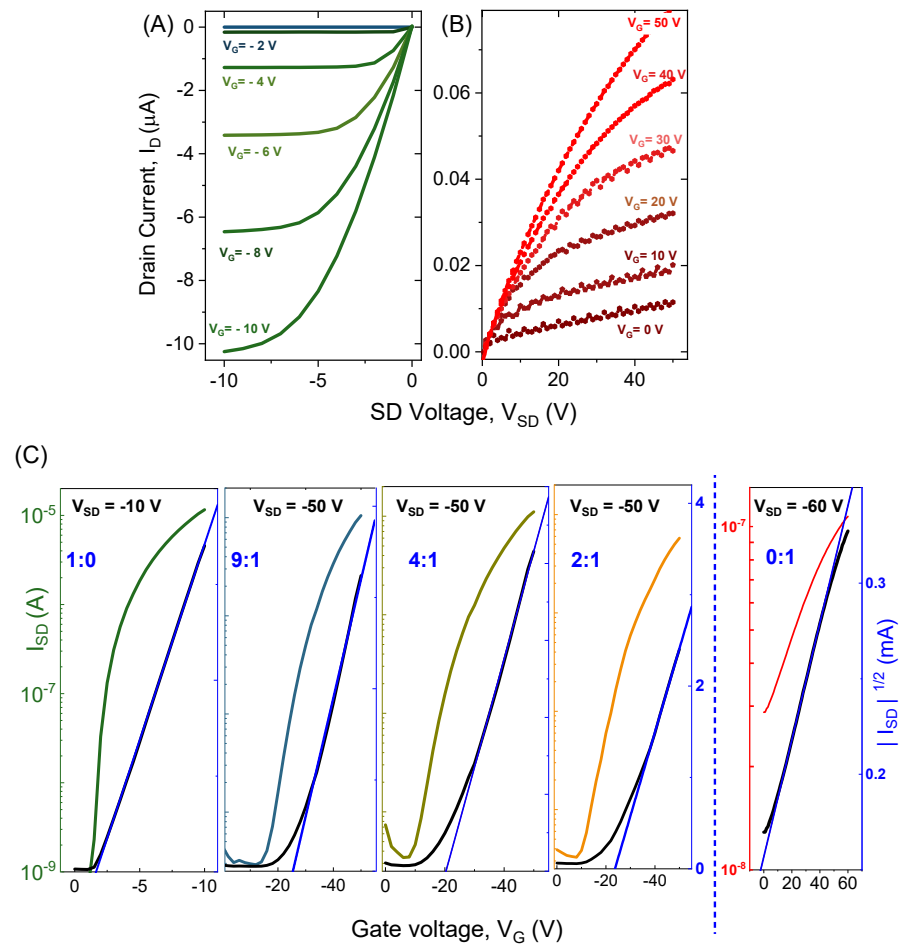


Figure 3.16: Output characteristics of A) pure DPP-DTT and, B) pure PDI. And, C) transfer characteristics of pure DPP-DTT and PDI and the composite system.

3.2.3 Summary

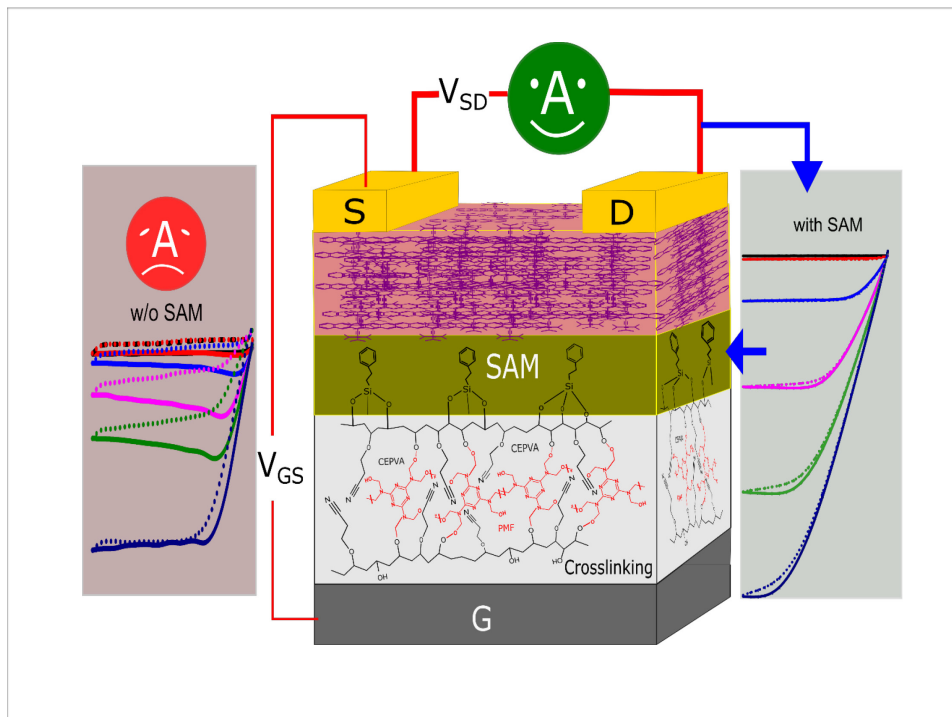
The memristors, made as sandwich structures with active layers from newly synthesized carbazole-containing polymer, PCaPMA, and composite system of DPP-DTT mixed with PDI as an active layer, were found to serve a dual purpose of

electronic memory and emulating biological synapse functionality. Both polymers exhibit compact pinhole-free layers suitable for the fabrication of a sandwiched system via solution casting methods. Devices exhibited hysteresis in their I-V characteristics, with the possibility of resistive switching between two distinct conducting states, making the polymers applicable in non-volatile ReRAM devices. The current ON/OFF ratio exceeded 100 with a satisfactory retention time, even without encapsulation.

Moreover, their resistance exhibits continuous variation upon triggering by voltage pulses, depending on their polarity, amplitude, and frequency. Mimicking neuro synaptic features, they demonstrate both short- and long-term plasticity. Persistent stimulation induces prolonged conductance changes, while weaker inputs yield volatile memorization. In PCaPMA, the memory transition occurs above a 1 Hz repetition rate of stimulating pulses, enabling associative learning akin to the Pavlov dog salivation experiment. In DPP-DTT, the memory window, synaptic plasticity, and bipolar resistive switching behavior were enhanced with increased perylene concentration.

These devices fulfill fundamental memory and synaptic plasticity requirements, addressing both short-term and long-term plasticity, as demonstrated by PPF/D and STDP characteristics. The resistive switching was attributed to the bulk properties of the polymers. In PCaPMA, the tendency of carbazole units to undergo conformational changes and redox reactions governs the changes. In DPP-DTT: PDI, trapping/detrapping combined with redox reaction support the conductance changes.

3.3 Role of dipolar polarization and interface optimization on the performance of OFETs



3.3.1 Overview of the study

Organic field-effect transistors, OFET, as the fundamental electronic component, are increasingly being adapted for flexible electronics. Achieving optimal performance while ensuring stability and reproducibility remains a challenge. High dielectric constant of the gate dielectrics is essential for desirable electrical characteristics and flexible device application, necessitating the production of pinhole-free thin layers, primarily using printing technology.[254]

Conventional polymer dielectrics often have low dielectric constants, leading to diminished device performance and increased power consumption.[255] To address this, modifications such as polyvinyl alcohol to poly(2-cyanoethyl vinyl ether) (CEPVA) have been introduced, exhibiting a low dielectric loss and dielectric constant (ϵ') around 15, when crosslinked with various crosslinkers.[174,256] The crosslinking improves layer integrity by forming a rigid network of hydrogen bonds, consequently locking the dipolar disorders.[160] Furthermore, studies on bias stress effects have shown that intentional charging of polymer dielectrics before applying the S-D voltage can lead to the threshold voltage (V_T) shift and changes in hysteresis.[257] Defects on dielectrics and OSC layers or at their interface have an impact on the OFET performance. Overall, the study of these effects can provide insights into hysteresis, charge trapping/detrapping, dielectric polarization, and ion migration.[258,259] The presence and nature of hysteresis in I-V characteristics of output or transfer curves, can vary depending on their origin and location. Clockwise or anticlockwise hysteresis can provide insight into underlying mechanisms such as slow-responding polar species or trap DOS in the dielectric medium, respectively.[259]

The common approach to mitigate these defects in OFETs involves the introduction of a self-assembling monolayer (SAM) of small molecules, or a thin buffer layer coating of non-polar molecules or polymer, referred to as surface passivation.[260,261] SAMs, typically composed of binding, spacer, and functional units, are often made of silanes. These molecules are covalently bonded to the surface, enhancing surface energy and hydrophobicity, and thus reducing water adsorption.[262] SAMs promote better molecular ordering of the OSCs layer and optimize the OSC crystal growth. Different SAMs, such as phosphonic or carboxylic acids for oxidic surfaces, organosulfur and chloro-silanes for metals, silicon, and polymeric surfaces containing hydroxyl groups, were proved to improve charge

injection and transport, ultimately enhancing charge carrier mobility.[263,264] They even alter the work function of metals lowering the energetic barrier.[85]

In the present work, a crosslinked dielectric system was exploited, followed by surface passivation. The influence of four crosslinkers (HAD, SU, PMF, and HMBG as listed in Fig. 2.3) on the hysteresis of I-V characteristics was studied. The effect of passivation with trimethoxy(2-phenylethyl) silane (PETMS) as SAM molecule is presented. Passivation was used to minimize trapping centers at the dielectric surface and improve mutual interactions between dielectrics and the OSC layer.[22,265] As the charge-transporting (active) layer, TIPS pentacene and DPP-DTT were used. Gold or platinum electrodes were used as S-D electrodes for small contact resistance and good charge injection due to their compatibility with p-type OSCs.

3.3.2 Results and discussion

3.3.2.1 Impact of casting conditions on OFET properties

Fig. 3.17 depicts the output and transfer characteristics of an OFET incorporating a PVP dielectric layer prepared through three solution casting techniques: spin coating, dip coating, and printing. The PVP polymer with HMBG crosslinker, 4:1 by wt%, was dissolved in propylene glycol methyl ether acetate. The resultant layer underwent crosslinking at 150°C in 100 mbar vacuum oven for 2 h.

All devices exhibited typical p-type transistor behavior, operating efficiently at lower voltages. The spin-coated PVP dielectric layer (approx. 200 nm thick), demonstrated optimal characteristics in both output and transfer curves (Fig. 3.17). In contrast, dip-coated dielectric film (around 100 nm thick) exhibited increased film roughness (5-10 nm) and a 50% reduction in mobility, along with a higher V_T . OFETs with thicker dielectric layers (about 800 nm) made by printing required higher operating voltages and a higher S-D voltage was required to achieve saturation.

OFETs prepared with spin-coating, dip-coating, and printing of dielectrics exhibited different mobility values of 0.51, 0.12, and 0.08 $\text{cm}^2\text{V}^{-1}\text{s}^{-1}$, and threshold voltages of -1.3, -3.0, and 8.0 V, respectively.

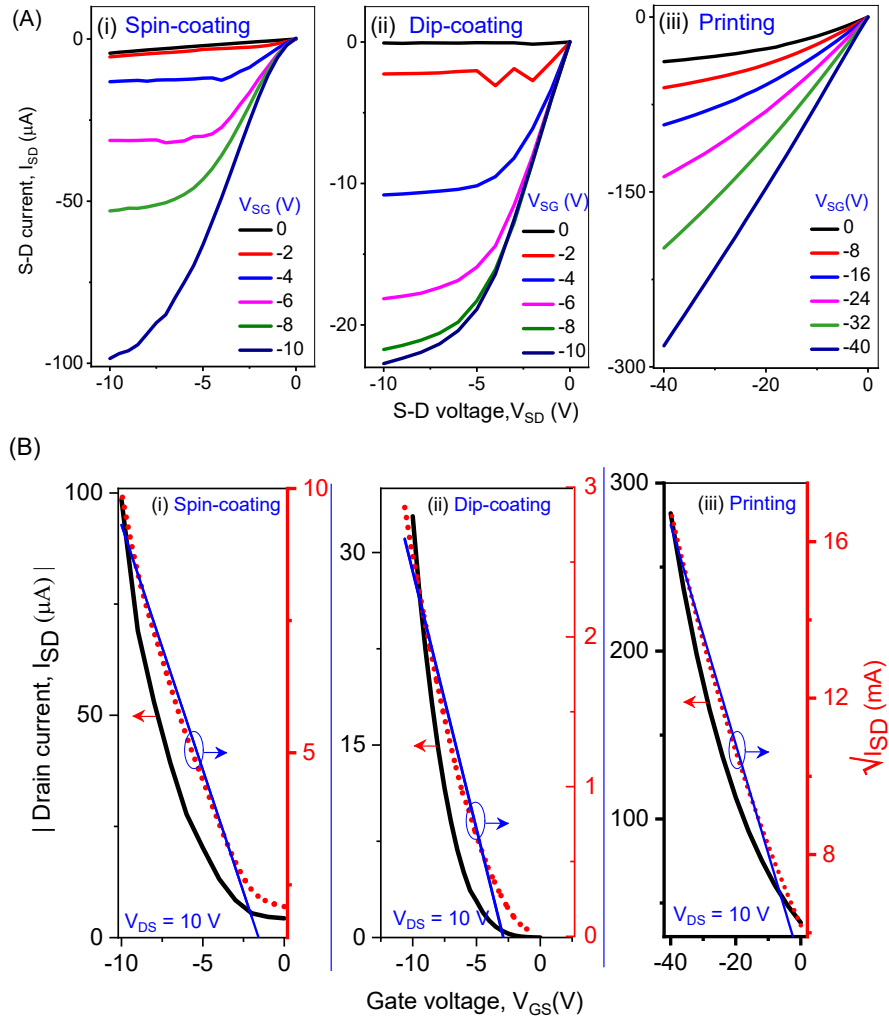


Figure 3.17: OFET output (A) and transfer (B) characteristics with PVP dielectrics cast via dip-coating (16 mm/min), spin-coating (2000 rpm), and screen printing.

3.3.2.2 Fully printed OFET

One set of OFETs was fabricated by preparing all layers by printing. Electrical characteristics were measured in both ambient and vacuum (pressure 5×10^{-5} mbar). Small hysteresis was observed in output characteristics when measured in air (Fig. 3.18B) and became more pronounced with increased pre-bias time of the gate field. The device measured in air exhibited S-D current at $V_{SG} = 0$ V, likely from water content causing anticlockwise hysteresis, but the field effect and the saturation were still observed.[257,259] The hysteresis nearly disappeared in a vacuum with a slight reduction in current, supporting the hypothesis of humidity effects from polar dielectrics.

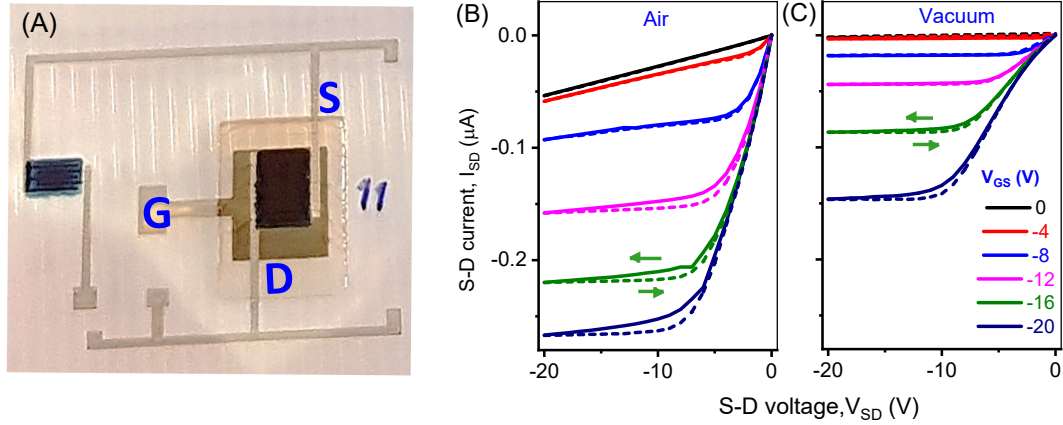


Figure 3.18: A) Optical image of fully printed transistor on flexible PET substrate (printed PVP layer: light grey, printed DPP DTT layer: dark grey). B-C) Output characteristics of the device measured in air and vacuum (5×10^{-5} mbar).

3.3.2.3 OFETs with polymer dielectric crosslinked by various crosslinkers.

In the second part of the study, a high-k dielectric ($\epsilon' \sim 15$), CEPVA,[256] was used for OFET fabrication. CEPVA was crosslinked with the aim of increasing its T_g , and the impact of various crosslinkers on device performance was investigated. Compared to devices without crosslinked dielectric, crosslinking the layer increased the current ON/OFF ratio and decreased leakage current. It also helped to avoid dielectric breakdown, even at high operating voltages.[174] However, crosslinking adversely affected the I-V characteristics, introducing increased hysteresis in transfer characteristics (Fig. 3.18).

With all crosslinkers used in this study, the transfer characteristics displayed anticlockwise hysteresis during cycling the gate voltage, suggesting the influence of traps within the active channel or at the interface between dielectrics and OSC.[266] PMF crosslinker, containing a hydroxyl linker, demonstrated saturated output curves but significant hysteresis with a large shift in V_T and reduced channel current. Crosslinkers HDA or SU, containing more electronegative halide linkers (Cl or F), showed relatively smaller hysteresis in transfer characteristics but the I_{SD} current decreased significantly after initial onset, creating a bell-shaped hysteresis. The only minimal hysteresis observed for $V_{GS} = 0V$ suggests charge trapping/de-trapping is the main cause of hysteresis, as it is more sensitive to V_{SG} than V_{SD} . [258] The uncrosslinked fraction of hydroxyl groups or the impurities likely contribute to trap DOS.

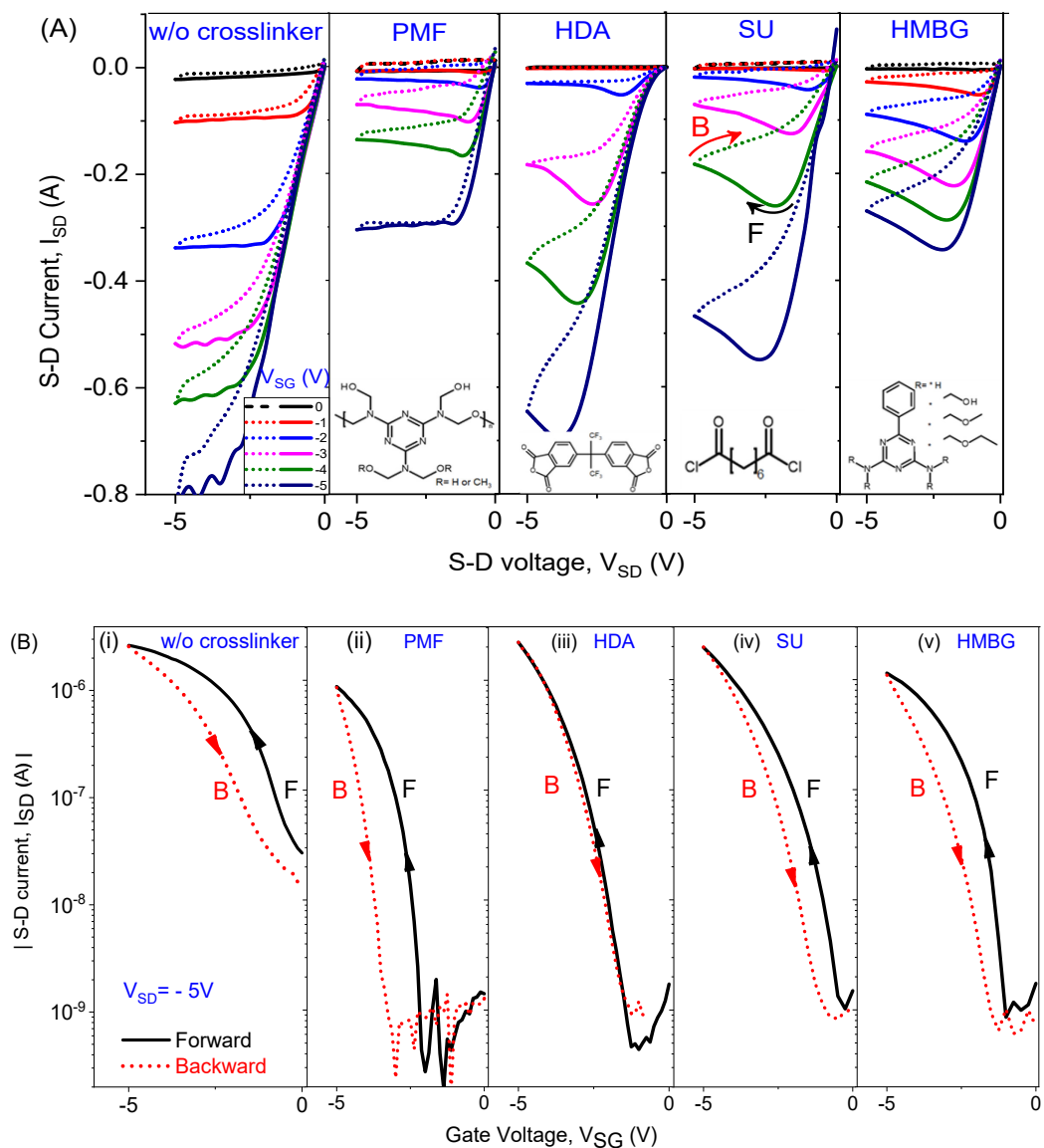


Figure. 3.19: (A) Output and (B) transfer characteristics of OFETs having CEPVA dielectrics without any crosslinker and crosslinked with HDA, SU, PMF, and HMBG from left to right, respectively. In both output and transfer characteristics, the solid lines represent the forward bias sweep continuously increased from zero and dotted line represents the backward bias sweep decreased from maximum to zero. F and B denotes forward and backward sweeps.

3.3.2.4 Interface optimization using self-assembling monolayer

A strategy to mitigate hysteresis of I-V characteristics of OFETs involves the incorporation of a blocking layer, like a self-assembling monolayer (SAM), between

the OSC and gate dielectric. This layer impedes charge penetration from the gate dielectric into the OSC active layer, consequently reducing the charge trapping. In CEPVA dielectrics crosslinked with PMF, significant hysteresis was observed, characterized by a bell-shaped profile between linear and saturation regime. Applying a PETMS monolayer at the dielectric-OSC interface notably reduced this hysteresis, accompanied by a threefold increase in channel current (Fig. 3.20).

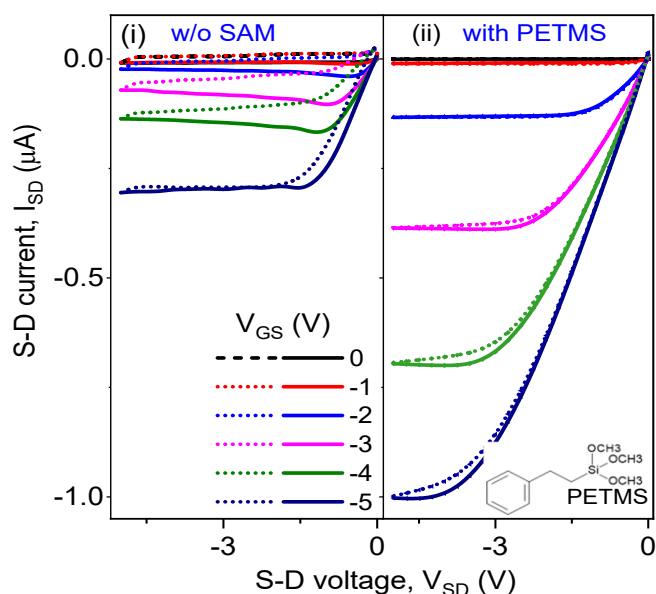


Figure 3.20: Output characteristics of OFETs with CEPVA dielectrics crosslinked with PMF (i) without applying SAM and (ii) after silanisation with PETMS silane.

3.3.3 Summary

In conclusion, we investigated the influence of various solution-casting methods on the OFET performance with PVP dielectrics. Spin coating demonstrated superior results, while printing emerged as essential for market transition, offering operational versatility. Additionally, CEPVA dielectrics crosslinked with different crosslinkers exhibited enhanced performance of the device but the hysteresis effect was increased. The integration of PETMS, a self-assembling monolayer (SAM), showed promise in mitigating hysteresis, highlighting a viable strategy for improving OFET characteristics. Further research is crucial to fully grasp the understanding of observed variations in hysteresis with different crosslinkers and other OFET parameters.

4. Conclusions

In this thesis, we contributed to the research of photophysical and electrical phenomena in organic semiconductors. We focused namely on the processes that occur in these materials upon photoexcitation and on the charge transport influenced by trapping/detrapping on localized levels and by the dynamics of molecular segments.

The first part delved into the excited-state dynamics of two TDPP derivatives, R-BOX and R-TCN, characterized by the extended conjugation and differing electron-withdrawing end groups. With optical spectroscopic techniques, the chapter explored the excited-state phenomena in these compounds in solutions and thin films, together with the vibrational evolution of excited states, and their dependence on molecular packing in solid state. Notably, the identification of efficient ISC in R-TCN solution and the long-time signals resembling triplet states formed by singlet fission in thin films of both molecules contribute to the understanding of the structure-property relationship. As the main result, we showed that also thermal effects must be considered for the interpretation of transient optical absorption spectra obtained by the pump-and-probe laser spectroscopy in longer time delays since they can lead to misinterpretation of data and erroneous quantitative analysis.

In the second part we focused on the development and characterization of memristive devices capable of exhibiting electronic memory and emulating the functionality of biological synapses. Sandwich structures that employed PCaPMA polymer and DPP-DTT: PDI composite as the active layers showed memristive properties that exhibited both features. The incorporation of a low-molecular-weight acceptor molecule, perylene, into a DPP-DTT polymer has enhanced synaptic plasticity. The findings underscored the potential of these systems in neuromorphic computing and AI.

In the last part, we focused on the impact of dipolar relaxation in polymer dielectrics on the performance of organic field-effect transistors. This work highlighted the importance of interface engineering for device performance.

All these results achieved within this Thesis contributed to the understanding of the physical nature of the studied phenomena in organic materials and can be further exploited in materials science and device engineering in organic electronics.

Bibliography

- [1] A. Köhler, H. Bässler, *Electronic processes in organic semiconductors*, Wiley-VCH, Weinheim, Germany, 2015.
- [2] O. Ostroverkhova, *Organic optoelectronic materials: Mechanisms and applications*, *Chem. Rev.* 116 (2016) 13279–13412. <https://doi.org/10.1021/acs.chemrev.6b00127>.
- [3] S. Forrest, N.C. Moore, Energy efficiency with organic electronics: Ching W. Tang revisits his days at Kodak, *MRS Bull.* 37 (2012) 552–553. <https://doi.org/10.1557/mrs.2012.125>.
- [4] J. Kalinowski, *Organic light-emitting diodes: Principles, characteristics and processes*, CRC Press, Florida, 2018.
- [5] M.C. Choi, Y. Kim, C.S. Ha, *Polymers for flexible displays: From material selection to device applications*, *Prog. Polym. Sci.* 33 (2008) 581–630. <https://doi.org/10.1016/j.progpolymsci.2007.11.004>.
- [6] LG advances OLED technology with a transparent and flexible UHD display 77 inch, (2017). <https://www.digitalavmagazine.com/en/2018/05/25/lg-avanza-tecnologia-oled-con-pantalla-uhd-transparente-y-flexible-77-pulgadas/>.
- [7] E.K. Solak, E. Irmak, *Advances in organic photovoltaic cells: A comprehensive review of materials, technologies, and performance*, *RSC Adv.* 13 (2023) 12244–12369. <https://doi.org/10.1039/d3ra01454a>.
- [8] L. Lu, D. Wang, C. Pu, Y. Cao, Y. Li, P. Xu, X. Chen, C. Liu, S. Liang, L. Suo, Y. Cui, Z. Zhao, Y. Guo, J. Liang, Y. Liu, High-performance flexible organic field effect transistors with print-based nanowires, *Microsystems Nanoeng.* 9 (2023) 80. <https://doi.org/10.1038/s41378-023-00551-x>.
- [9] S.S. Goswami, T. Venkatesan, An organic approach to low energy memory and brain inspired electronics, *Appl. Phys. Rev.* 7 (2020) 021303. <https://doi.org/10.1063/1.5124155>.
- [10] F. Pan, S. Gao, C. Chen, C. Song, F. Zeng, Recent progress in resistive random access memories: Materials, switching mechanisms, and performance, *Mater. Sci. Eng. R.* 83 (2014) 1–59. <https://doi.org/10.1016/j.mser.2014.06.002>.
- [11] W. Huang, X. Xia, C. Zhu, P. Steichen, W. Quan, W. Mao, J. Yang, L. Chu, X. Li, Memristive artificial synapses for neuromorphic computing, *Nano-Micro Lett.* 13 (2021) 85. <https://doi.org/10.1007/s40820-021-00618-2>.
- [12] Y. Li, Q. Qian, X. Zhu, Y. Li, M. Zhang, J. Li, C. Ma, H. Li, J. Lu, Q. Zhang, Recent advances in organic-based materials for resistive memory applications, *InfoMat.* 2 (2020) 995–1033. <https://doi.org/10.1002/inf2.12120>.
- [13] Y. van de Burgt, A. Melianas, S.T. Keene, G. Malliaras, A. Salleo, Organic electronics for neuromorphic computing, *Nat. Electron.* 1 (2018) 386–397. <https://doi.org/10.1038/s41928-018-0103-3>.
- [14] A.S. Sokolov, H. Abbas, Y. Abbas, C. Choi, Towards engineering in memristors for emerging memory and neuromorphic computing: A review, *J. Semicond.* 42 (2021) 013101. <https://doi.org/10.1088/1674-4926/42/1/013101>.
- [15] C. Il Park, M. Seong, M.A. Kim, D. Kim, H. Jung, M. Cho, S.H. Lee, H. Lee, S. Min, J. Kim, M. Kim, J.H. Park, S. Kwon, B. Kim, S.J. Kim, W. Park, J.Y. Yang, S. Yoon, I. Kang, World's first large size 77-inch transparent flexible OLED display, *J. Soc. Inf. Disp.* 26 (2018) 287–295. <https://doi.org/10.1002/jsid.663>.
- [16] LG V30+ phone - impressive specs, LG. (2023). https://www.lg.com/levant_en/mobile-phones/lg-V30-plus.
- [17] A. Moliton, *Optoelectronics of molecules and polymers*, Springer, New York, 2010.
- [18] T. Tsanova, Acciona puts organic PV on wind turbine tower to lift efficiency, *Renewables Now.* (2019). <https://renewablesnow.com/news/acciona-puts-organic-pv-on-wind-turbine-tower-to-lift-efficiency-654541/>.
- [19] V. Coropceanu, J. Cornil, D.A. da Silva Filho, Y. Olivier, R. Silbey, J.-L. Brédas, Charge transport in organic semiconductors, *Chem. Rev.* 107 (2007) 926–952. <https://doi.org/10.1021/cr050140x>.
- [20] O. Ostroverkhova, *Handbook of organic materials for electronic and photonic devices*, Woodhead Publishing, Amsterdam, 2019. <https://doi.org/10.1016/c2016-0-05254-3>.
- [21] P. Bober, Y. Li, U. Acharya, Y.R. Panthi, J. Pflieger, P. Humpolíček, M. Trchová, J. Stejskal, Acid Blue dyes in polypyrrole synthesis: The control of polymer morphology at nanoscale in the promotion of high conductivity and the reduction of cytotoxicity, *Synth. Met.* 237 (2018) 40–49. <https://doi.org/10.1016/j.synthmet.2018.01.010>.
- [22] H. Klauk, Organic thin-film transistors, *Chem. Soc. Rev.* 39 (2010) 2643–2666.

- <https://doi.org/10.1039/b909902f>.
- [23] Y. Xiao, B. Jiang, Z. Zhang, S. Ke, Y. Jin, X. Wen, C. Ye, A review of memristor: Material and structure design, device performance, applications and prospects, *Sci. Technol. Adv. Mater.* 24 (2023) 2162323. <https://doi.org/10.1080/14686996.2022.2162323>.
- [24] K. Walzer, B. Männig, M. Pfeiffer, K. Leo, Highly efficient organic devices based on electrically doped transport layers, *Chem. Rev.* 107 (2007) 1233–1271. <https://doi.org/10.1021/cr050156n>.
- [25] L. Cao, C. Ren, T. Wu, Recent advances in doped organic field-effect transistors: Mechanism, influencing factors, materials, and development directions, *J. Mater. Chem. C* 11 (2023) 3428–3447. <https://doi.org/10.1039/d2tc05035h>.
- [26] H. Akamatu, H. Inokuchi, Y. Matsunaga, Electrical conductivity of the perylene–bromine complex, *Nature*. 173 (1954) 168–169. <https://doi.org/10.1038/173168a0>.
- [27] H. Inokuchi, Photoconductivity of the condensed polynuclear aromatic compounds, *Bull. Chem. Soc. Jpn.* 27 (1954) 22–27. <https://doi.org/10.1246/bcsj.27.22>.
- [28] M. Pope, Professor Hiroo Inokuchi: A pioneer and major contributor to the field of electronic processes in organic materials, *Synth. Met.* 64 (1994) 109–113. [https://doi.org/10.1016/0379-6779\(94\)90101-5](https://doi.org/10.1016/0379-6779(94)90101-5).
- [29] Organic electronics market size & trends analysis, 2023-2032, *Glob. Mark. Insights.* (2023). <https://www.gminsights.com/industry-analysis/organic-electronics-market>.
- [30] H. Spanggaard, F.C. Krebs, A brief history of the development of organic and polymeric photovoltaics, *Sol. Energy Mater. Sol. Cells.* 83 (2004) 125–146. <https://doi.org/10.1016/j.solmat.2004.02.021>.
- [31] N.B. Zhitenev, A. Sidorenko, D.M. Tennant, R.A. Cirelli, Chemical modification of the electronic conducting states in polymer nanodevices, *Nat. Nanotechnol.* 2 (2007) 237–242. <https://doi.org/10.1038/nnano.2007.75>.
- [32] S. Gao, X. Yi, J. Shang, G. Liu, R.W. Li, Organic and hybrid resistive switching materials and devices, *Chem. Soc. Rev.* 48 (2019) 1531–1565. <https://doi.org/10.1039/c8cs00614h>.
- [33] J. Fu, P.W.K. Fong, H. Liu, C.S. Huang, X. Lu, S. Lu, M. Abdelsamie, T. Kodalle, C.M. Sutter-Fella, Y. Yang, G. Li, 19.31% binary organic solar cell and low non-radiative recombination enabled by non-monotonic intermediate state transition, *Nat. Commun.* 14 (2023) 1760. <https://doi.org/10.1038/s41467-023-37526-5>.
- [34] J.F. Gibbons, W.E. Beadle, Switching properties of thin Nio films, *Solid State Electron.* 7 (1964) 785–790. [https://doi.org/10.1016/0038-1101\(64\)90131-5](https://doi.org/10.1016/0038-1101(64)90131-5).
- [35] P.O. Sliva, G. Dir, C. Griffiths, Bistable switching and memory devices, *J. Non. Cryst. Solids.* 2 (1970) 316–333. [https://doi.org/10.1016/0022-3093\(70\)90148-1](https://doi.org/10.1016/0022-3093(70)90148-1).
- [36] E. Apollos, Memristor theory and mathematical modelling, *Int. J. Comput. Appl.* 178 (2019) 1–8. <https://doi.org/10.5120/ijca2019919089>.
- [37] Y. Sadaoka, Y. Sakai, Switching in poly(N-vinylcarbazole) thin films, *J. Chem. Soc. Faraday Trans. 2 Mol. Chem. Phys.* 72 (1976) 1911–1915. <https://doi.org/10.1039/f29767201911>.
- [38] M.M. Rehman, H.M.M.U. Rehman, J.Z. Gul, W.Y. Kim, K.S. Karimov, N. Ahmed, Decade of 2D-materials-based RRAM devices: A review, *Sci. Technol. Adv. Mater.* 21 (2020) 147–186. <https://doi.org/10.1080/14686996.2020.1730236>.
- [39] A. Krishnaprasad, N. Choudhary, S. Das, D. Dev, H. Kalita, H.-S. Chung, O. Aina, Y. Jung, T. Roy, Electronic synapses with near-linear weight update using MoS₂/graphene memristors, *Appl. Phys. Lett.* 115 (2019) 103104. <https://doi.org/10.1063/1.5108899>.
- [40] S. Liu, X. Chen, G. Liu, Conjugated polymers for information storage and neuromorphic computing, *Polym. Int.* 70 (2021) 374–403. <https://doi.org/10.1002/pi.6017>.
- [41] S. Lee, S. Kim, H. Yoo, Contribution of polymers to electronic memory devices and applications, *Polymers (Basel)*. 13 (2021) 3774. <https://doi.org/10.3390/polym13213774>.
- [42] B. Hwang, J.S. Lee, Recent advances in memory devices with hybrid materials, *Adv. Electron. Mater.* 5 (2019) 1800519. <https://doi.org/10.1002/aelm.201800519>.
- [43] D. Johnson, Mapping of memristor could speed its commercialization, *IEE Spectr.* (2021). <https://spectrum.ieee.org/mapping-of-memristor-could-speed-its-commercialization>.
- [44] R. Fackenthal, M. Kitagawa, W. Otsuka, K. Prall, D. Mills, K. Tsutsui, J. Javanifard, K. Tedrow, T. Tsushima, Y. Shibahara, G. Hush, 19.7 A 16Gb ReRAM with 200MB/s write and 1GB/s read in 27nm technology, in: 2014 IEEE Int. Solid-State Circuits Conf. San Fr. CA, USA, IEEE, 2014. <https://doi.org/10.1109/isscc.2014.6757460>.
- [45] P. Clarke, Crossbar ReRAM in production at SMIC, *EE Times.* (2017). <https://www.eetimes.com/crossbar-reram-in-production-at-smic/>.
- [46] G. Hilsen, IMEC, Panasonic push progress on ReRAM, *EE Times.* (2015).

- https://www.eetimes.com/document.asp?doc_id=13273.
- [47] W.C. Shen, C.Y. Mei, Y.D. Chih, S.S. Sheu, M.J. Tsai, Y.C. King, C.J. Lin, High-K metal gate contact RRAM (CRRAM) in pure 28nm CMOS logic process, in: 2012 Int. Electron Devices Meet., IEEE, 2012: pp. 31.6.1-31.6.4. <https://doi.org/10.1109/iedm.2012.6479146>.
- [48] S. Yu, P.Y. Chen, Emerging memory technologies: Recent trends and prospects, *IEEE Solid-State Circuits Mag.* 8 (2016) 43–56. <https://doi.org/10.1109/mssc.2016.2546199>.
- [49] E. Briman, The future of memory-The time for ReRAM, *Circuit Cellar.* (2022). <https://circuitcellar.com/insights/tech-the-future/the-future-of-memory-the-time-for-reram/>.
- [50] J. Xiang, T.K. Wang, Q. Zhao, W. Huang, C.L. Ho, W.Y. Wong, Ferrocene-containing poly(fluorenylethynylene)s for nonvolatile resistive memory devices, *J. Mater. Chem. C.* 4 (2016) 921–928. <https://doi.org/10.1039/c5tc03042k>.
- [51] M. Pope, C.E. Swenberg, *Electronic processes in organic crystals and polymers*, Oxford University Press, Oxford, 1999. <https://doi.org/10.1093/oso/9780195129632.001.0001>.
- [52] A. Tsumura, H. Koezuka, T. Ando, Macromolecular electronic device: Field-effect transistor with a polythiophene thin film, *Appl. Phys. Lett.* 49 (1986) 1210–1212. <https://doi.org/10.1063/1.97417>.
- [53] K. Myny, E. Van Veenendaal, G.H. Gelinck, J. Genoe, W. Dehaene, P. Heremans, An 8b organic microprocessor on plastic foil, in: 2011 IEEE Int. Solid-State Circuits Conf. San Fr. CA, USA, 2011: pp. 321–324. <https://doi.org/10.1109/isscc.2011.5746337>.
- [54] K.C. Kao, W. Hwang, S. Choi, Electrical transport in solids, *Phys. Today.* 36 (1983) 90. <https://doi.org/10.1063/1.2915326>.
- [55] J.W. Schultz, *Dielectric spectroscopy in analysis of polymers*, Wiley, New Jersey, 2006. <https://doi.org/10.1002/9780470027318.a2004>.
- [56] P.W. Atkins, J. De Paula, J. Keeler, *Molecular structure*, in: *Atkins' Phys. Chem.*, Oxford University Press, 2018.
- [57] J. Roncali, Molecular engineering of the band gap of π -conjugated systems: Facing technological applications, *Macromol. Rapid Commun.* 28 (2007) 1761–1775. <https://doi.org/10.1002/marc.200700345>.
- [58] P.M. Beaujuge, C.M. Amb, J.R. Reynolds, Spectral engineering in π -conjugated polymers with intramolecular donor-acceptor interactions, *Acc. Chem. Res.* 43 (2010) 1396–1407. <https://doi.org/10.1021/ar100043u>.
- [59] Z.G. Zhang, J. Wang, Structures and properties of conjugated donor-acceptor copolymers for solar cell applications, *J. Mater. Chem.* 22 (2012) 4178–4187. <https://doi.org/10.1039/c2jm14951f>.
- [60] Y. Yang Michael, W. Chen, L. Dou, W.H. Chang, H.S. Duan, B. Bob, G. Li, Y. Yang, High-performance multiple-donor bulk heterojunction solar cells, *Nat. Photonics.* 9 (2015) 190–198. <https://doi.org/10.1038/nphoton.2015.9>.
- [61] J. Lee, R. Singh, Competitive role between conformational lock and steric hindrance in D-A copolymers containing 1,4-bis(thieno[3,2-b]thiophen-2-yl)benzene unit, *Dye. Pigment.* 181 (2020) 108540. <https://doi.org/10.1016/j.dyepig.2020.108540>.
- [62] E.W. Lim, R. Ismail, Conduction mechanism of valence change resistive switching memory: A survey, *Electron.* 4 (2015) 586–613. <https://doi.org/10.3390/electronics4030586>.
- [63] R. Hausermann, *Fast and slow charge trapping and transport in organic semiconductors*, ETH Zurich, 2013.
- [64] S. Jung, C.H. Kim, Y. Bonnassieux, G. Horowitz, Injection barrier at metal/organic semiconductor junctions with a Gaussian density-of-states, *J. Phys. D. Appl. Phys.* 48 (2015) 395103. <https://doi.org/10.1088/0022-3727/48/39/395103>.
- [65] I.D. Parker, Carrier tunneling and device characteristics in polymer light-emitting diodes, *J. Appl. Phys.* 75 (1994) 1656–1666. <https://doi.org/10.1063/1.356350>.
- [66] R. Saxena, V.R. Nikitenko, I.I. Fishchuk, Y. V. Burdakov, Y. V. Metel, J. Genoe, H. Bässler, A. Köhler, A. Kadashchuk, Role of the reorganization energy for charge transport in disordered organic semiconductors, *Phys. Rev. B.* 103 (2021) 165202. <https://doi.org/10.1103/PhysRevB.103.165202>.
- [67] A. Troisi, Charge transport in high mobility molecular semiconductors: Classical models and new theories, *Chem. Soc. Rev.* 40 (2011) 2347–2358. <https://doi.org/10.1039/c0cs00198h>.
- [68] Y.N. Gartstein, E.M. Conwell, Field-dependent thermal injection into a disordered molecular insulator, *Chem. Phys. Lett.* 255 (1996) 93–98. [https://doi.org/10.1016/0009-2614\(96\)00359-4](https://doi.org/10.1016/0009-2614(96)00359-4).
- [69] H. Bässler, A. Köhler, Charge transport in organic semiconductors, *Top. Curr. Chem.* (2012) 312. https://doi.org/10.1007/128_2011_218.
- [70] H.F. Haneef, A.M. Zeidell, O.D. Jurchescu, Charge carrier traps in organic semiconductors: A

- review on the underlying physics and impact on electronic devices, *J. Mater. Chem. C* 8 (2020) 759. <https://doi.org/10.1039/c9tc05695e>.
- [71] W.L. Kalb, S. Haas, C. Krellner, T. Mathis, B. Batlogg, Trap density of states in small-molecule organic semiconductors: A quantitative comparison of thin-film transistors with single crystals, *Phys. Rev. B* 81 (2010) 155315. <https://doi.org/10.1103/PhysRevB.81.155315>.
- [72] S.M. Sze, K.K. Ng, S.M. Sze, K.N. Kwok, *Physics of semiconductor devices*, Wiley, New York, 2006. <https://doi.org/10.1002/0470068329>.
- [73] M.-A. Stoeckel, Y. Olivier, M. Gobbi, D. Dudenko, V. Lemaire, M. Zbiri, A.Y. Guilbert, G. D'Avino, F. Liscio, N. Demitri, X. Jin, Y.-G. Jeong, M.-V. Nardi, L. Pasquali, L. Razzari, D. Beljonne, P. Samori, E. Orgiu, Freeing electrons from extrinsic and intrinsic disorder yields band-like transport in n-type organic semiconductors, *ArXiv Mater. Sci.* (2019). <https://api.semanticscholar.org/CorpusID:202565474>.
- [74] Z. Zhao, M.E. El-Khouly, Q. Che, F. Sun, B. Zhang, H. He, Y. Chen, Redox-active azulene-based 2D conjugated covalent organic framework for organic memristors, *Angew. Chem. - Int. Ed.* 62 (2023) e202217249. <https://doi.org/10.1002/anie.202217249>.
- [75] S. Giannini, A. Carof, J. Blumberger, Crossover from hopping to band-like charge transport in an organic semiconductor model: Atomistic nonadiabatic molecular dynamics simulation, *J. Phys. Chem. Lett.* 9 (2018) 3116–3223. <https://doi.org/10.1021/acs.jpcclett.8b01112>.
- [76] L. Bozano, S.A. Carter, J.C. Scott, G.G. Malliaras, P.J. Brock, Temperature- and field-dependent electron and hole mobilities in polymer light-emitting diodes, *Appl. Phys. Lett.* 74 (1999) 1132–1134. <https://doi.org/10.1063/1.123959>.
- [77] A. Miller, E. Abrahams, Impurity conduction at low concentrations, *Phys. Rev.* 120 (1960) 745–755. <https://doi.org/10.1103/PhysRev.120.745>.
- [78] P. Mark, W. Helfrich, Space charge-limited currents in organic crystals, *J. Appl. Phys.* 33 (1962) 205–215. <https://doi.org/10.1063/1.1728487>.
- [79] M. Campos, Space charge limited current in naphthalene single crystals, *Mol. Cryst. Liq. Cryst.* 18 (1972) 105–115. <https://doi.org/10.1080/15421407208083254>.
- [80] S.A. Moiz, I.A. Khan, W.A. Younis, K.S. Karimov, Space charge-limited current model for polymers, in: *Conduct. Polym., InTech*, 2016: pp. 91–117. <https://doi.org/10.5772/63527>.
- [81] P.N. Murgatroyd, Theory of space-charge-limited current enhanced by Frenkel effect, *J. Phys. D. Appl. Phys.* 3 (1970) 151–156. <https://doi.org/10.1088/0022-3727/3/2/308>.
- [82] C.W. Tang, S.A. Vanslyke, Organic electroluminescent diodes, *Appl. Phys. Lett.* 51 (1987) 913–915. <https://doi.org/10.1063/1.98799>.
- [83] I.H. Campbell, J.D. Kress, R.L. Martin, D.L. Smith, N.N. Barashkov, J.P. Ferraris, Controlling charge injection in organic electronic devices using self-assembled monolayers, *Appl. Phys. Lett.* 71 (1997) 3528–3530. <https://doi.org/10.1063/1.120381>.
- [84] L. Jun, S. Jiu-Xun, C. Zhao, Improved expression of charge-carrier mobility in disordered semiconducting polymers considering dependence on temperature, electric field and charge-carrier density, *Synth. Met.* 159 (2009) 1915–1921. <https://doi.org/10.1016/j.synthmet.2009.07.007>.
- [85] B. De Boer, A. Hadipour, M.M. Mandoc, T. Van Woudenberg, P.W.M. Blom, Tuning of metal work functions with self-assembled monolayers, *Adv. Mater.* 17 (2005) 621–625. <https://doi.org/10.1002/adma.200401216>.
- [86] M. Guesmi, V. Kanclír, T. Thoř, O. Taboubi, I. Šeděnková, Y.R. Panthi, J. Pflieger, K. Židek, I. Sed, Y.R. Panthi, J. Pflieger, K. Zidek, Study of defects in fused silica via a Franck-Condon analysis, *J. Lumin.* 257 (2023) 119668. <https://doi.org/10.1016/j.jlumin.2023.119668>.
- [87] Y.R. Panthi, J. Pflieger, D. Výprachtický, A. Pandey, M.A. Thottappali, I. Šeděnková, M. Konefał, S.H. Foulger, Rewritable resistive memory effect in poly[N-(3-(9H-carbazol-9-yl)propyl)-methacrylamide] memristor, *J. Mater. Chem. C* 11 (2023) 17093–17105. <https://doi.org/10.1039/d3tc03394e>.
- [88] M.T. do Casal, J.M. Toldo, F. Plasser, M. Barbatti, Using diketopyrrolopyrroles to stabilize double excitation and control internal conversion, *Phys. Chem. Chem. Phys.* 24 (2022) 23279–23288. <https://doi.org/10.1039/d2cp03533b>.
- [89] J.M.S. Lopes, N.M.B. Neto, P.T. Araujo, An introduction to steady-state and time-resolved photoluminescence, in: *Inorg. Photochem., SpringerLink, Heidelberg*, 2022. https://doi.org/10.1007/978-3-030-63713-2_6.
- [90] Y. Liu, P. Kilby, T.J. Frankcombe, T.W. Schmidt, Electronic transitions of molecules: Vibrating Lewis structures, *Chem. Sci.* 10 (2019) 6809–6814. <https://doi.org/10.1039/c9sc02534k>.
- [91] and J.K. Peter Atkins, Julio de Paula, *Atkins' Physical Chemistry*, Oxford Univ. Press USA 12th Ed. (2022). <https://global.oup.com/ukhe/product/atkins-physical-chemistry->

- 9780198847816?cc=cz&lang=en& (accessed December 26, 2023).
- [92] M. Baer, R. Englman, A modified Born-Oppenheimer equation: application to conical intersections and other types of singularities, *Chem. Phys. Lett.* 265 (1997) 105–108. [https://doi.org/10.1016/s0009-2614\(96\)01411-x](https://doi.org/10.1016/s0009-2614(96)01411-x).
- [93] M.A. Filatov, Heavy-atom-free BODIPY photosensitizers with intersystem crossing mediated by intramolecular photoinduced electron transfer, *Org. Biomol. Chem.* 18 (2019) 10–27. <https://doi.org/10.1039/c9ob02170a>.
- [94] L. Xu, C.W. Tang, L.J. Rothberg, High efficiency phosphorescent white organic light-emitting diodes with an ultra-thin red and green co-doped layer and dual blue emitting layers, *Org. Electron.* 32 (2016) 54–58. <https://doi.org/10.1016/j.orgel.2016.02.010>.
- [95] K.-W. Tsai, M.-K. Hung, Y.-H. Mao, S.-A. Chen, K.-W. Tsai, M.-K. Hung, Y.-H.S. Mao, -A Chen, Solution-processed thermally activated delayed fluorescent OLED with high EQE as 31% using high triplet energy crosslinkable hole transport materials, *Adv. Funct. Mater.* 29 (2019) 1901025. <https://doi.org/10.1002/adfm.201901025>.
- [96] L.G. Franca, A. Danos, R. Saxena, S. Kuila, K. Stavrou, C. Li, S. Wedler, A. Köhler, A.P. Monkman, Exploring the early time behavior of the excited states of an archetype thermally activated delayed fluorescence molecule, *J. Phys. Chem. Lett.* 15 (2024) 1734–1740. <https://doi.org/10.1021/acs.jpcllett.4c00030>.
- [97] A. Shukla, S.K.M. McGregor, R. Wawrzinek, S. Saggar, E.G. Moore, S.-C. Lo, E.B. Namdas, Light amplification and efficient electroluminescence from a solution-processable diketopyrrolopyrrole derivative via triplet-to-singlet upconversion, *Adv. Funct. Mater.* 31 (2021) 2009817. <https://doi.org/10.1002/adfm.202009817>.
- [98] A.S. Tanwar, R. Parui, R. Garai, M.A. Chanu, P.K. Iyer, Dual “static and dynamic” fluorescence quenching mechanisms based detection of TNT via a cationic conjugated polymer, *ACS Meas. Sci. Au.* 2 (2022) 23–30. <https://doi.org/10.1021/acsmesuresciau.1c00023>.
- [99] W.H. Chiang, Y.H. Chang, C.C. Lin, H.C. Kuo, G.R. Lin, J.J. Huang, Effect of radiative & nonradiative energy transfer processes of light-emitting diodes combined with quantum dots for visible light communication, *Discov. Nano.* 18 (2023) 29. <https://doi.org/10.1186/S11671-023-03812-w>.
- [100] A.B. Pun, L.M. Campos, D.N. Congreve, Tunable emission from triplet fusion upconversion in diketopyrrolopyrroles, *J. Am. Chem. Soc.* 141 (2019) 3777–3781. <https://doi.org/10.1021/jacs.8b11796>.
- [101] F. Auzel, Upconversion and anti-Stokes processes with f and d ions in solids, *Chem. Rev.* 104 (2004) 139–173. <https://doi.org/10.1021/cr020357g>.
- [102] S. Singh, W.J. Jones, W. Siebrand, B.P. Stoicheff, W.G. Schneider, Laser generation of excitons and fluorescence in anthracene crystals, *J. Chem. Phys.* 42 (1965) 330–342. <https://doi.org/10.1063/1.1695695>.
- [103] M.C. Hanna, A.J. Nozik, Solar conversion efficiency of photovoltaic and photoelectrolysis cells with carrier multiplication absorbers, *J. Appl. Phys.* 100 (2006) 074510. <https://doi.org/10.1063/1.2356795/342873>.
- [104] M.B. Smith, J. Michl, Singlet fission, *Chem. Rev.* 110 (2010) 6891–6936. <https://doi.org/10.1021/cr1002613>.
- [105] H. Kim, P.M. Zimmerman, Coupled double triplet state in singlet fission, *Phys. Chem. Chem. Phys.* 20 (2018) 30083–30094. <https://doi.org/10.1039/c8cp06256k>.
- [106] C.M. Mauck, P.E. Hartnett, E.A. Margulies, L. Ma, C.E. Miller, G.C. Schatz, T.J. Marks, M.R. Wasielewski, Singlet fission via an excimer-like intermediate in 3,6-bis(thiophen-2-yl)diketopyrrolopyrrole derivatives, *J. Am. Chem. Soc.* 138 (2016) 11749–11761. <https://doi.org/10.1021/jacs.6B05627>.
- [107] D. Rais, P. Toman, U. Acharya, Y.R. Panthi, M. Menšík, A. Zhigunov, M.A. Thottappali, J. Pflieger, M. Vala, A. Marková, S. Stříteský, M. Weiter, M. Cigánek, J. Krajčovič, K. Pauk, A. Imramovský, A. Zaykov, J. Michl, Singlet Fission in thin solid films of bis(thienyl)diketopyrrolopyrroles, *Chempluschem.* 1 (2020) 2689–2703. <https://doi.org/10.1002/cplu.202000623>.
- [108] S. Havriliak, S. Negami, A complex plane representation of dielectric and mechanical relaxation processes in some polymers, *Polymer (Guildf).* 8 (1967) 161–210. [https://doi.org/10.1016/0032-3861\(67\)90021-3](https://doi.org/10.1016/0032-3861(67)90021-3).
- [109] J.R. Macdonald, Impedance spectroscopy, *Ann. Biomed. Eng.* 20 (1992) 289–305. <https://doi.org/10.1166/jnn.2011.5092>.
- [110] A. Vassilikou-Dova, I.M. Kalogeras, Dielectric analysis, in: *Therm. Anal. Polym. Fundam. Appl.*, Wiley, New Jersey, 2009. <https://doi.org/10.1002/9780470423837.ch6>.

- [111] R.D. Priestley, P. Rittigstein, L.J. Broadbelt, K. Fukao, J.M. Torkelson, Evidence for the molecular-scale origin of the suppression of physical ageing in confined polymer: Fluorescence and dielectric spectroscopy studies of polymer-silica nanocomposites, *J. Phys. Condens. Matter.* 19 (2007) 205120. <https://doi.org/10.1088/0953-8984/19/20/205120>.
- [112] L.O. Chua, Memristor—The missing circuit element, *IEEE Trans. Circuit Theory.* 18 (1971) 507–519. <https://doi.org/10.1109/tct.1971.1083337>.
- [113] S.P. Adhikari, M.P. Sah, H. Kim, L.O. Chua, Three fingerprints of memristor, *IEEE Trans. Circuits Syst. I Regul. Pap.* 60 (2013) 3008–3021. <https://doi.org/10.1109/tcsi.2013.2256171>.
- [114] Y.P. Lin, C.H. Bennett, T. Cabaret, D. Vodenicarevic, D. Chabi, D. Querlioz, B. Joussetme, V. Derycke, J.O. Klein, Physical realization of a supervised learning system built with organic memristive synapses, *Sci. Rep.* 6 (2016) 31932. <https://doi.org/10.1038/srep31932>.
- [115] X.M. Wang, S.Y.R. Hui, Graphical modelling of pinched hysteresis loops of memristors, *IET Sci. Meas. Technol.* 11 (2017) 86–96. <https://doi.org/10.1049/iet-smt.2016.0210>.
- [116] L. Chua, If it's pinched it's a memristor, *Semicond. Sci. Technol.* 29 (2014) 104001. <https://doi.org/10.1088/0268-1242/29/10/104001>.
- [117] R.S. Williams, How we found the missing Memristor, *IEEE Spectr.* 45 (2008) 28–35. <https://doi.org/10.1109/mspec.2008.4687366>.
- [118] D.B. Strukov, G.S. Snider, D.R. Stewart, R.S. Williams, The missing memristor found, *Nature.* 453 (2008) 80–83. <https://doi.org/10.1038/nature06932>.
- [119] A.K. Sharma, *Advanced semiconductor memories : Architectures, designs, and applications*, Wiley, New Jersey, 2003.
- [120] Q.D. Ling, D.J. Liaw, C. Zhu, D.S.H. Chan, E.T. Kang, K.G. Neoh, Polymer electronic memories: Materials, devices and mechanisms, *Prog. Polym. Sci.* 33 (2008) 917–978. <https://doi.org/10.1016/j.progpolymsci.2008.08.001>.
- [121] F. Zahoor, F.A. Hussin, U.B. Isyaku, S. Gupta, F.A. Khanday, A. Chattopadhyay, H. Abbas, Resistive random access memory: Introduction to device mechanism, materials and application to neuromorphic computing, *Discov. Nano.* 18 (2023) 36. <https://doi.org/10.1186/s11671-023-03775-y>.
- [122] Aspinity analogML core is world's lowest power always-on listening system wake-up solution, Aspinity. (2019). <https://www.aspinity.com/>.
- [123] K.K. Parhi, N.K. Unnikrishnan, Brain-inspired computing: Models and architectures, *IEEE Open J. Circuits Syst.* 1 (2020) 185–204. <https://doi.org/10.1109/ojcas.2020.3032092>.
- [124] M. Lefkowitz, Professor's perceptron paved the way for AI – 60 years too soon, *Cornell Chron.* (2019). <https://news.cornell.edu/stories/2019/09/professors-perceptron-paved-way-ai-60-years-too-soon>.
- [125] F. Alibart, E. Zamanidoost, D.B. Strukov, Pattern classification by memristive crossbar circuits using ex situ and in situ training, *Nat. Commun.* 4 (2013) 2072. <https://doi.org/10.1038/ncomms3072>.
- [126] D.A. Laws, J. McClure, M. Riordan, 1960: Metal oxide semiconductor (MOS) transistor demonstrated, *Comput. Hist. Museum.* (2024). <https://www.computerhistory.org/siliconengine/metal-oxide-semiconductor-mos-transistor-demonstrated/>.
- [127] L. Xie, J. Shen, A. Mifsud, C. Wang, A. Alshaya, C. Papavassiliou, A wide dynamic range read-out system For resistive switching technology, in: 2022 IEEE Int. Symp. Circuits Syst. (ISCAS), Austin, TX, USA, 2022: pp. 2003–2007. <https://doi.org/10.1109/iscas48785.2022.9937616>.
- [128] C. Mead, M. Ismail, *Analog VLSI implementation of neural systems*, Kluwer Academic Publishers, Heidelberg, 1989.
- [129] M.B. Kennedy, Synaptic Signaling in Learning and Memory, *Cold Spring Harb. Perspect Biol.* 8 (2013) a016824.
- [130] M.C.W. van Rossum, G.Q. Bi, G.G. Turrigiano, Stable Hebbian learning from spike timing-dependent plasticity, *J. Neurosci.* 20 (2000) 8812–8821. <https://doi.org/10.1523/jneurosci.20-23-08812.2000>.
- [131] Y.R. Panthi, A. Pandey, A. Sturcova, D. Vyprachticky, S.H. Foulger, J. Pflieger, Emulating synaptic plasticity with a poly[N-(3-(9H-carbazol-9-yl)propyl)methacrylamide] memristor, *Mater. Adv.* 5 (2024) 6388–6398. <https://doi.org/10.1039/d4ma00399c>.
- [132] S. Munde, Neuromorphic computing market size, share, trends, growth & forecast - 2032, *Mark. Res. Futur.* (2020). <https://www.marketresearchfuture.com/reports/neuromorphic-computing-market-5110>.
- [133] G.H. Kim, J.H. Lee, Y. Ahn, W. Jeon, S.J. Song, J.Y. Seok, J.H. Yoon, K.J. Yoon, T.J. Park, C.S. Hwang, 32×32 crossbar array resistive memory composed of a stacked schottky diode

- and unipolar resistive memory, *Adv. Funct. Mater.* 23 (2013) 1440–1449. <https://doi.org/10.1002/adfm.201202170>.
- [134] D. Prime, S. Paul, Overview of organic memory devices, *Philos. Trans. R. Soc. A.* 367 (2009) 4141–4157. <https://doi.org/10.1098/rsta.2009.0165>.
- [135] W. Sun, B. Gao, M. Chi, Q. Xia, J.J. Yang, H. Qian, H. Wu, Understanding memristive switching via in situ characterization and device modeling, *Nat. Commun.* 10 (2019) 3453. <https://doi.org/10.1038/s41467-019-11411-6>.
- [136] E. von Hauff, The role of molecular structure and conformation in polymer electronics, in: *Semicond. Semimetals*, Elsevier Inc., New York, 2011: pp. 231–260. <https://doi.org/10.1016/B978-0-12-391060-8.00007-1>.
- [137] Y. Sun, L. Li, D. Wen, X. Bai, Bistable electrical switching and nonvolatile memory effect in mixed composite of oxadiazole acceptor and carbazole donor, *Org. Electron.* 25 (2015) 283–288. <https://doi.org/10.1016/j.orgel.2015.07.002>.
- [138] M.A. Zidan, J.P. Strachan, W.D. Lu, The future of electronics based on memristive systems, *Nat. Electron.* 1 (2018) 22–29. <https://doi.org/10.1038/s41928-017-0006-8>.
- [139] J. Godlewski, J. Kalinowski, Trapping effects on emission-limited current flow in narrow-band insulators, *Phys. Status Solidi.* 56 (1979) 293–303. <https://doi.org/10.1002/pssa.2210560132>.
- [140] D. He, H. Zhuang, H. Liu, H. Liu, H. Li, J. Lu, Adjustment of conformation change and charge trapping in ion-doped polymers to achieve ternary memory performance, *J. Mater. Chem. C.* 1 (2013) 7883–7889. <https://doi.org/10.1039/c3tc31759e>.
- [141] S.-L. Lim, Q. Ling, E.-Y.H. Teo, C.-X. Zhu, D.S.-H. Chan, E.-T. Kang, K.-G. Neoh, Conformation-induced electrical bistability in non-conjugated polymers with pendant carbazole moieties, *Chem. Mater.* 19 (2007) 5148–5157. <https://doi.org/10.1021/cm071520x>.
- [142] Y. Bandera, T.M. McFarlane, M.K. Burdette, M. Jurca, O. Klep, S.H. Foulger, Synthesis of n-alkyl methacrylate polymers with pendant carbazole moieties and their derivatives, *J. Polym. Sci. Part A Polym. Chem.* 57 (2019) 70–76. <https://doi.org/10.1002/pola.29285>.
- [143] W.-P. Lin, S.-J. Liu, T. Gong, Q. Zhao, W. Huang, Polymer-based resistive memory materials and devices, *Adv. Mater.* 26 (2014) 570–606. <https://doi.org/10.1002/adma.201302637>.
- [144] S.H. Foulger, Y. Bandera, B. Grant, J. Vilčáková, P. Sáha, Exploiting multiple percolation in two-terminal memristor to achieve a multitude of resistive states, *J. Mater. Chem. C.* 9 (2021) 8975–8986. <https://doi.org/10.1039/d1tc00987g>.
- [145] W. Tang, H. He, J. Shi, B. Cao, C. Yang, C. Fan, Poly(N-vinylcarbazole) (PVK) as a high-potential organic polymer cathode for dual-intercalation Na-ion batteries, *Org. Electron.* 75 (2019) 105386. <https://doi.org/10.1016/j.orgel.2019.105386>.
- [146] Q.-D. Ling, D.-J. Liaw, C. Zhu, D.S.-H. Chan, E.-T. Kang, K.-G. Neoh, Polymer memories: Bistable electrical switching and device performance, *Prog. Polym. Sci.* 33 (2008) 917–978. <https://doi.org/10.1016/j.polymer.2007.06.025>.
- [147] C. Wang, Z. Si, X. Jiang, A. Malik, Y. Pan, S. Stathopoulos, A. Serb, S. Wang, T. Prodromakis, C. Papavassiliou, Multi-state memristors and their applications: An overview, *IEEE J. Emerg. Sel. Top. Circuits Syst.* 12 (2022) 723–734. <https://doi.org/10.1109/jetcas.2022.3223295>.
- [148] D.J. Wouters, E. Linn, *Fundamentals of memristors*, 2015.
- [149] B. Bin Cui, Z. Mao, Y. Chen, Y.W. Zhong, G. Yu, C. Zhan, J. Yao, Tuning of resistive memory switching in electropolymerized metallopolymeric films, *Chem. Sci.* 6 (2015) 1308–1315. <https://doi.org/10.1039/c4sc03345k>.
- [150] A. Pandey, A. Chernyshev, Y.R. Panthi, A. Sturcov, O. Kocková, S.H. Foulger, J., Vohlidal, J. Pflieger, Synapse-mimicking memristors based on 3, 6-di(tpy)-9- phenylcarbazole unimer and its copolymer with cobalt(II) ions, *Polymers (Basel).* 16 (2024) 542. <https://doi.org/10.3390/polym16040542>.
- [151] S. Goswami, A.J. Matula, S.P. Rath, S. Hedström, S. Saha, M. Annamalai, D. Sengupta, A. Patra, S. Ghosh, H. Jani, S. Sarkar, M.R. Motapothula, C.A. Nijhuis, J. Martin, S. Goswami, V.S. Batista, T. Venkatesan, Robust resistive memory devices using solution-processable metal-coordinated azo aromatics, *Nat. Mater.* 16 (2017) 1216–1224. <https://doi.org/10.1038/nmat5009>.
- [152] B. Cho, S. Song, Y. Ji, T.W. Kim, T. Lee, Organic resistive memory devices: Performance enhancement, integration, and advanced architectures, *Adv. Funct. Mater.* 21 (2011) 2806–2829. <https://doi.org/10.1002/adfm.201100686>.
- [153] S. Gao, C. Song, C. Chen, F. Zeng, F. Pan, Formation process of conducting filament in planar organic resistive memory, *Appl. Phys. Lett.* 102 (2013) 141606. <https://doi.org/10.1063/1.4802092>.
- [154] Y. Busby, S. Nau, S. Sax, E.J.W. List-Kratochvil, J. Novak, R. Banerjee, F. Schreiber, J.J.

- Pireaux, Direct observation of conductive filament formation in Alq₃ based organic resistive memories, *J. Appl. Phys.* 118 (2015) 075501. <https://doi.org/10.1063/1.4928622>.
- [155] Y. Busby, N. Crespo-Monteiro, M. Girleanu, M. Brinkmann, O. Ersen, J.J. Pireaux, 3D imaging of filaments in organic resistive memory devices, *Org. Electron.* 16 (2014) 40–45. <https://doi.org/10.1016/j.orgel.2014.10.039>.
- [156] M. Lanza, H.S.P. Wong, E. Pop, D. Ielmini, D. Strukov, B.C. Regan, L. Larcher, M.A. Villena, J.J. Yang, L. Goux, A. Belmonte, Y. Yang, F.M. Puglisi, J. Kang, B. Magyari-Köpe, E. Yalon, A. Kenyon, M. Buckwell, A. Mehonic, A. Shluger, H. Li, T.H. Hou, B. Hudec, D. Akinwande, R. Ge, S. Ambrogio, J.B. Roldan, E. Miranda, J. Suñe, K.L. Pey, X. Wu, N. Raghavan, E. Wu, W.D. Lu, G. Navarro, W. Zhang, H. Wu, R. Li, A. Holleitner, U. Wurstbauer, M.C. Lemme, M. Liu, S. Long, Q. Liu, H. Lv, A. Padovani, P. Pavan, I. Valov, X. Jing, T. Han, K. Zhu, S. Chen, F. Hui, Y. Shi, Recommended methods to study resistive switching devices, *Adv. Electron. Mater.* 5 (2019) 1800143. <https://doi.org/10.1002/aelm.201800143>.
- [157] G. Casula, P. Cosseddu, Y. Busby, J.J. Pireaux, M. Rosowski, B. Tkacz Szczesna, K. Soliwoda, G. Celichowski, J. Grobelny, J. Novák, R. Banerjee, F. Schreiber, A. Bonfiglio, Air-stable, non-volatile resistive memory based on hybrid organic/inorganic nanocomposites, *Org. Electron.* 18 (2015) 17–23. <https://doi.org/10.1016/j.orgel.2015.01.001>.
- [158] IEEE standard for test methods for the characterization of organic transistors and materials, 2008. <https://ieeexplore.ieee.org/servlet/opac?punumber=5982061> (accessed November 27, 2023).
- [159] S. Ghosh, S. Shankar, D.S. Philips, A. Ajayaghosh, Diketopyrrolopyrrole-based functional supramolecular polymers: Next-generation materials for optoelectronic applications, *Mater. Today Chem.* 16 (2020) 100242. <https://doi.org/10.1016/j.mtchem.2020.100242>.
- [160] B. Paruzel, J. Pflieger, J. Brus, M. Menšík, F. Piana, U. Acharya, Impact of hydrogen bonds limited dipolar disorder in high-k polymer gate dielectric on charge carrier transport in OFET, *Polymers (Basel)*. 12 (2020) 826. <https://doi.org/10.3390/polym12040826>.
- [161] M. Chen, B. Peng, H. Li, Single-crystal dielectrics for organic field-effect transistors, *J. Mater. Chem. C*. 10 (2022) 4985–4998. <https://doi.org/10.1039/d2tc00100d>.
- [162] H. Jiang, Z. Huang, G. Xue, H. Chen, H. Li, Electron transport at the interface of organic semiconductors and hydroxyl-containing dielectrics, *J. Mater. Chem. C*. 6 (2018) 12001–12005. <https://doi.org/10.1039/c8tc01343h>.
- [163] R. Zeis, C. Besnard, T. Siegrist, C. Schlockermann, X. Chi, C. Kloc, Field effect studies on rubrene and impurities of rubrene, *Chem. Mater.* 18 (2006) 244–248. https://doi.org/10.1021/CM0502626/SUPPL_FILE/CM0502626SI20050203_102938.CIF.
- [164] Y. Zhao, W. Wang, Z. He, B. Peng, C.A. Di, H. Li, High-performance and multifunctional organic field-effect transistors, *Chinese Chem. Lett.* 34 (2023) 108094. <https://doi.org/10.1016/j.ccllet.2022.108094>.
- [165] X. Mou, J. Tang, Y. Lyu, Q. Zhang, S. Yang, F. Xu, W. Liu, M. Xu, Y. Zhou, W. Sun, Y. Zhong, B. Gao, P. Yu, H. Qian, H. Wu, Analog memristive synapse based on topotactic phase transition for high-performance neuromorphic computing and neural network pruning, *Sci. Adv.* 7 (2021) eabh0648. <https://doi.org/10.1126/sciadv.abh0648>.
- [166] J. Pflieger, Y.R. Panthi, B. Paruzel, L. Kubáč, J. Černý, Přepisovatelný elektronický rezistivní paměťový element: CZ 32526 U1, 32526, 2019. https://old.starfos.tacr.cz/en/result/RIV%2F61389013%3A____%2F19%3A00500870.
- [167] Y.R. Panthi, A. Thottappali, P. Horáková, L. Kubáč, Photophysics of benzoxazole and dicyano functionalised diketopyrrolopyrrole derivatives : Insights into ultrafast processes and the triplet state, *ChemPhysChem*. 25 (2024) e202300872. <https://doi.org/doi.org/10.1002/cphc.202300872>.
- [168] L. Feng, W. Tang, J. Zhao, R. Yang, W. Hu, Q. Li, R. Wang, X. Guo, Unencapsulated air-stable organic field effect transistor by all solution processes for low power vapor sensing, *Sci. Rep.* 6 (2016) 20671. <https://doi.org/10.1038/srep20671>.
- [169] L. Rocard, A. Goujon, P. Hudhomme, Nitro-perylenediimide: An emerging building block for the synthesis of functional organic materials, *Molecules*. 25 (2020) 1402. <https://doi.org/10.3390/molecules25061402>.
- [170] A. Kovalenko, J. Honová, M. Vala, S. Luňák, L. Fekete, P. Horáková, L. Dokládálová, L. Kubáč, M. Weiter, Effect of the side chains and anode material on thermal stability and performance of bulk-heterojunction solar cells using DPP(TBFu)₂ derivatives as donor materials, *Int. J. Photoenergy*. 2015 (2015) 734917. <https://doi.org/10.1155/2015/734917>.
- [171] S. Ghosh, R. Raveendran, A. Sacki, S. Seki, M. Namboothiry, A. Ajayaghosh, Charge carrier polarity modulation in diketopyrrolopyrrole-based low band gap semiconductors by terminal

- functionalization, *ACS Appl. Mater. Interfaces*. 11 (2019) 1088–1095. <https://doi.org/10.1021/acsami.8b16714>.
- [172] S.W. Kim, S. Park, S. Lee, D. Kim, G. Lee, J. Son, K. Cho, S. Won Kim, S. Park, S. Lee, D. Kim, G. Lee, J. Son, K. Cho, S.W. Kim, S. Park, S. Lee, D. Kim, G. Lee, J. Son, K. Cho, Stretchable mesh-patterned organic semiconducting thin films on creased elastomeric substrates, *Adv. Funct. Mater.* 31 (2021) 1–8. <https://doi.org/10.1002/adfm.202010870>.
- [173] I.B. Kim, D. Khim, S.Y. Jang, J. Kim, B.K. Yu, Y.A. Kim, D.Y. Kim, D-A copolymer with high ambipolar mobilities based on dithienothiophene and diketopyrrolopyrrole for polymer solar cells and organic field-effect transistors, *Org. Electron.* 26 (2015) 251–259. <https://doi.org/10.1016/j.orgel.2015.07.003>.
- [174] F. Piana, B. Paruzel, J. Pflieger, Influence of curing agent on dielectric properties of crosslinked poly(vinylalcohol-co-vinylcyanoethoxy), *Chem. Pap.* 72 (2018) 1811–1821. <https://doi.org/10.1007/s11696-018-0460-4>.
- [175] A. Teichler, J. Perelaer, U.S. Schubert, Inkjet printing of organic electronics-comparison of deposition techniques and state-of-the-art developments, *J. Mater. Chem. C*. 1 (2013) 1910. <https://doi.org/10.1039/c2tc00255h>.
- [176] OFET-substrate for the characterization of organic semiconductor materials, n.d. <https://www.fraunhofer.de/en.html>.
- [177] Platinum OFET Test Chips | High Density | Ossila, Ossila. (n.d.). <https://www.ossila.com/products/prefabricated-platinum-ofet-test-chips>.
- [178] R. Berera, R. van Grondelle, J.T.M. Kennis, Ultrafast transient absorption spectroscopy: Principles and application to photosynthetic systems, *Photosynth. Res.* 101 (2009) 105–118. <https://doi.org/10.1007/s11120-009-9454-y>.
- [179] G. Lanzani, G. Cerullo, D. Polli, A. Gambetta, M. Zavelani-Rossi, C. Gadermaier, Photophysics of conjugated polymers: The contribution of ultrafast spectroscopy, *Phys. Status Solidi Appl. Res.* 201 (2004) 1116–1131. <https://doi.org/10.1002/pssa.200404337>.
- [180] J.J. Snellenburg, S. Laptенок, R. Seger, K.M. Mullen, I.H.M. van Stokkum, Glotaran: A java-based graphical user interface for the r package TIMP, *J. Stat. Softw.* 49 (2012) 1–22. <https://doi.org/10.18637/jss.v049.i03>.
- [181] P.T. Dong, J.X. Cheng, Pump-probe microscopy: Theory, instrumentation, and applications, *Spectroscopy*. 32 (2017) 24–36.
- [182] M. Rumetshofer, P. Heim, B. Thaler, W.E. Ernst, M. Koch, W. von der Linden, Analysis of femtosecond pump-probe photoelectron-photoion coincidence measurements applying Bayesian probability theory, *Phys. Rev. A*. 97 (2018) 062503. <https://doi.org/10.1103/PhysRevA.97.062503>.
- [183] I. Carmichael, G.L. Hug, Triplet-triplet absorption spectra of organic molecules in condensed phases, *J. Phys. Chem. Ref. Data*. 15 (1986) 1986. <https://doi.org/10.1063/1.555770>.
- [184] M. Fiaz, M.S. Beevers, Temperature dependence of static dielectric permittivity and dipole moments of poly(N-vinylcarbazole), *Polymer (Guildf)*. 37 (1996) 755–760. [https://doi.org/10.1016/0032-3861\(96\)87250-8](https://doi.org/10.1016/0032-3861(96)87250-8).
- [185] M. Wojdyr, Fityk: A general-purpose peak fitting program, *J. Appl. Crystallogr.* 43 (2010) 1126–1128. <https://doi.org/10.1107/s0021889810030499>.
- [186] W. Li, K.H. Hendriks, M.M. Wienk, R.A.J. Janssen, Diketopyrrolopyrrole polymers for organic solar cells, *Acc. Chem. Res.* 49 (2016) 78–85. <https://doi.org/10.1021/acs.accounts.5b00334>.
- [187] S.C.J. Meskers, R.A.J. Janssen, B.W.H. Saes, M. Lutz, M.M. Wienk, Tuning the optical characteristics of diketopyrrolopyrrole molecules in the solid state by alkyl side chains, *J. Phys. Chem. C*. 124 (2020) 25229–25238. <https://doi.org/10.1021/acs.jpcc.0c07334>.
- [188] M.A. Naik, N. Venkatramaiah, C. Kanimozhi, S. Patil, Influence of side-chain on structural order and photophysical properties in thiophene based diketopyrrolopyrroles: A systematic study, *J. Phys. Chem. C*. 116 (2012) 26128–26137. <https://doi.org/10.1021/jp306365q>.
- [189] P. Heinrichová, J. Pospíšil, S. Strítěský, M. Vala, M. Weiter, P. Toman, D. Rais, J. Pflieger, M. Vondráček, D. Šimek, L. Fekete, P. Horáková, L. Dokládlová, L. Kubáč, I. Kratochvílová, Diketopyrrolopyrrole-based organic solar cells functionality: The role of orbital energy and crystallinity, *J. Phys. Chem. C*. 123 (2019) 11447–11463. <https://doi.org/10.1021/acs.jpcc.9b01328>.
- [190] A. Tang, B. Xiao, Y. Wang, F. Gao, K. Tajima, H. Bin, Z.G. Zhang, Y. Li, Z. Wei, E. Zhou, Simultaneously achieved high open-circuit voltage and efficient charge generation by fine-tuning charge-transfer driving force in nonfullerene polymer solar cells, *Adv. Funct. Mater.* 28 (2018) 1704507. <https://doi.org/10.1002/adfm.201704507>.
- [191] Y.W. Soon, S. Shoaee, R.S. Ashraf, H. Bronstein, B.C. Schroeder, W. Zhang, Z. Fei, M.

- Heeney, I. McCulloch, J.R. Durrant, Material crystallinity as a determinant of triplet dynamics and oxygen quenching in donor polymers for organic photovoltaic devices, *Adv. Funct. Mater.* 24 (2014) 1474–1482. <https://doi.org/10.1002/adfm.201302612>.
- [192] M.B. Smith, J. Michl, Recent advances in singlet fission, *Annu. Rev. Phys. Chem.* 64 (2013) 361–386. <https://doi.org/10.1146/annurev-physchem-040412-110130>.
- [193] M. Gudem, M. Kowalewski, Triplet-triplet annihilation dynamics of naphthalene, *Chem. - A Eur. J.* 28 (2022) e202200781. <https://doi.org/10.1002/chem.202200781>.
- [194] X.K. Chen, D. Kim, J.L. Brédas, Thermally activated delayed fluorescence (TADF) path toward efficient electroluminescence in purely organic materials: Molecular level insight, *Acc. Chem. Res.* 51 (2018) 2215–2224. <https://doi.org/10.1021/acs.accounts.8b00174>.
- [195] O.P. Dimitriev, Dynamics of excitons in conjugated molecules and organic semiconductor systems, *Chem. Rev.* 122 (2022) 8487–8593. <https://doi.org/10.1021/acs.chemrev.1c00648>.
- [196] P.E. Hartnett, E.A. Margulies, C.M. Mauck, S.A. Miller, Y. Wu, Y.L. Wu, T.J. Marks, M.R. Wasielewski, Effects of crystal morphology on singlet exciton fission in diketopyrrolopyrrole thin films, *J. Phys. Chem. B.* 120 (2016) 1357–1366. <https://doi.org/10.1021/acs.jpcc.5b10565>.
- [197] S.S. Murali, J.K. Gallaher, C. Janiseck, E.J. Tay, I. Wagner, K.E. Thorn, A. Ilina, R.R. Tamming, J. Wang, C. Sester, J.J. Sutton, M.B. Price, K.C. Gordon, K. Chen, X. Zhan, J.M. Hodgkiss, P.A. Hume, Triplets with a twist: Ultrafast intersystem crossing in a series of electron acceptor materials driven by conformational disorder, *J. Am. Chem. Soc.* 145 (2023) 732–744. <https://doi.org/10.1021/jacs.2c12605>.
- [198] C.M. Mauck, Y.J. Bae, M. Chen, N. Powers-Riggs, Y.L. Wu, M.R. Wasielewski, Charge-transfer character in a covalent diketopyrrolopyrrole dimer: Implications for singlet fission, *ChemPhotoChem.* 2 (2018) 223–233. <https://doi.org/10.1002/cptc.201700135>.
- [199] I. Papadopoulos, M.J. Álvaro-Martins, D. Molina, P.M. McCosker, P.A. Keller, T. Clark, Á. Sastre-Santos, D.M. Guldi, Solvent-dependent singlet fission in diketopyrrolopyrrole dimers: A mediating charge transfer versus a trapping symmetry-breaking charge separation, *Adv. Energy Mater.* 10 (2020) 2001496. <https://doi.org/10.1002/aenm.202001496>.
- [200] M. Kirkus, L. Wang, S. Mothy, D. Beljonne, J. Cornil, R.A.J. Janssen, S.C.J. Meskers, Optical properties of oligothiophene substituted diketopyrrolopyrrole derivatives in the solid phase: Joint J- and H-type aggregation, *J. Phys. Chem. A.* 116 (2012) 7927–7936. <https://doi.org/10.1021/jp305097q>.
- [201] S.J. Bradley, M. Chi, J.M. White, C.R. Hall, L. Goerigk, T.A. Smith, K.P. Ghiggino, The role of conformational heterogeneity in the excited state dynamics of linked diketopyrrolopyrrole dimers, *Phys. Chem. Chem. Phys.* 23 (2021) 9357–9364. <https://doi.org/10.1039/d1cp00541c>.
- [202] G. Angulo, G. Grampp, A. Rosspeintner, Recalling the appropriate representation of electronic spectra, *Spectrochim. Acta - Part A Mol. Biomol. Spectrosc.* 65 (2006) 727–731. <https://doi.org/10.1016/j.saa.2006.01.007>.
- [203] H. Bürckstümmer, A. Weissenstein, D. Bialas, F. Würthner, Synthesis and characterization of optical and redox properties of bithiophene-functionalized diketopyrrolopyrrole chromophores, *J. Org. Chem.* 76 (2011) 2426–2432. <https://doi.org/10.1021/jo2003117>.
- [204] D.W. Polak, M.T. do Casal, J.M. Toldo, X. Hu, G. Amoroso, O. Pomeranc, M. Heeney, M. Barbatti, M.N.R. Ashfold, T.A.A. Oliver, Probing the electronic structure and photophysics of thiophene–diketopyrrolopyrrole derivatives in solution, *Phys. Chem. Chem. Phys.* 24 (2022) 20138–20151. <https://doi.org/10.1039/d2cp03238d>.
- [205] J.C. Dean, R. Zhang, R.K. Hallani, R.D. Pensack, S.N. Sanders, D.G. Oblinsky, S.R. Parkin, L.M. Campos, J.E. Anthony, G.D. Scholes, Photophysical characterization and time-resolved spectroscopy of a anthradithiophene dimer: Exploring the role of conformation in singlet fission, *Phys. Chem. Chem. Phys.* 19 (2017) 23162–23175. <https://doi.org/10.1039/c7cp03774k>.
- [206] M.P. Grubb, P.M. Coulter, H.J.B. Marroux, A.J. Orr-Ewing, M.N.R. Ashfold, Unravelling the mechanisms of vibrational relaxation in solution, *Chem. Sci.* 8 (2017) 3062–3069. <https://doi.org/10.1039/c6sc05234g>.
- [207] A.K. Le, J.A. Bender, S.T. Roberts, Slow singlet fission observed in a polycrystalline perylenediimide thin film, *J. Phys. Chem. Lett.* 7 (2016) 4922–4928. <https://doi.org/10.1021/acs.jpcclett.6b02320>.
- [208] M.W.B. Wilson, A. Rao, J. Clark, R.S.S. Kumar, D. Brida, G. Cerullo, R.H. Friend, Ultrafast dynamics of exciton fission in polycrystalline pentacene, *J. Am. Chem. Soc.* 133 (2011) 11830–11833. <https://doi.org/10.1021/ja201688h>.
- [209] M.L. Williams, I. Schlesinger, C.E. Ramirez, R.M. Jacobberger, P.J. Brown, R.M. Young, M.R. Wasielewski, Effect of crystallinity on endoergic singlet fission in perylenediimide single

- crystals and polycrystalline films, *J. Phys. Chem. C.* 126 (2022) 10287–10297. <https://doi.org/10.1021/acs.jpcc.2c02298>.
- [210] L.M. Lifshits, D.S. Budkina, V. Singh, S.M. Matveev, A.N. Tarnovsky, J.K. Klosterman, Solution-state photophysics of: N-carbazolyl benzoate esters: Dual emission and order of states in twisted push-pull chromophores, *Phys. Chem. Chem. Phys.* 18 (2016) 27671–27683. <https://doi.org/10.1039/c6cp04619c>.
- [211] S. Albert-Seifried, R.H. Friend, Measurement of thermal modulation of optical absorption in pump-probe spectroscopy of semiconducting polymers, *Appl. Phys. Lett.* 98 (2011) 223304. <https://doi.org/10.1063/1.3595340/121815>.
- [212] D. Venkateshvaran, M. Nikolka, A. Sadhanala, V. Lemaire, M. Zelazny, M. Kepa, M. Hurhangee, A.J. Kronemeijer, V. Pecunia, I. Nasrallah, I. Romanov, K. Broch, I. McCulloch, D. Emin, Y. Olivier, J. Cornil, D. Beljonne, H. Sirringhaus, Approaching disorder-free transport in high-mobility conjugated polymers, *Nature.* 515 (2014) 384–388. <https://doi.org/10.1038/nature13854>.
- [213] J. Lenz, F. del Giudice, F.R. Geisenhof, F. Winterer, R.T. Weitz, Vertical, electrolyte-gated organic transistors show continuous operation in the MA cm⁻² regime and artificial synaptic behaviour, *Nat. Nanotechnol.* 14 (2019) 579–585. <https://doi.org/10.1038/s41565-019-0407-0>.
- [214] X.J. She, D. Gustafsson, H. Sirringhaus, A vertical organic transistor architecture for fast nonvolatile memory, *Adv. Mater.* 29 (2017) 1604769. <https://doi.org/10.1002/adma.201604769>.
- [215] F.C. Whitmore, H.S. Mosher, R.R. Adams, R.B. Taylor, E.C. Chapin, C. Weisel, W. Yanko, Basically substituted aliphatic nitriles and their catalytic reduction to amines, *J. Am. Chem. Soc.* 66 (1944) 725–731. <https://doi.org/10.1021/ja01233a019>.
- [216] H. Li, Z. Wang, C. Song, Y. Wang, Z. Lin, J. Xiao, R. Chen, C. Zheng, W. Huang, Manipulating charge transport in a π -stacked polymer through silicon incorporation, *J. Mater. Chem. C.* 2 (2014) 6946–6953. <https://doi.org/10.1039/c4tc00486h>.
- [217] S. Nara, T. Komiya, Studies on the relationship between water-saturated state and crystallinity by the diffraction method for moistened potato starch, *Starch-Stärke.* 35 (1983) 407–410. <https://doi.org/10.1002/star.19830351202>.
- [218] P. de Sainte Claire, Molecular simulation of excimer fluorescence in polystyrene and poly(vinylcarbazole), *J. Phys. Chem. B.* 110 (2006) 7334–7343.
- [219] G.E. Johnson, Emission properties of vinylcarbazole polymers, *J. Chem. Phys.* 62 (1975) 4697–4709. <https://doi.org/10.1063/1.430418>.
- [220] S. Ito, K. Yamashita, M. Yamamoto, Y. Nishijima, Photophysical properties of poly[2-(9-carbazolyl)ethyl methacrylate] films: Energy migration and carrier generation in films having no excimer-forming site, *Chem. Phys. Lett.* 117 (1985) 171–175. [https://doi.org/10.1016/0009-2614\(85\)85229-5](https://doi.org/10.1016/0009-2614(85)85229-5).
- [221] E. Kozma, D. Kotowski, S. Luzzati, M. Catellani, F. Bertini, A. Famulari, G. Raos, Improving the efficiency of P3HT:perylene diimide solar cells via bay-substitution with fused aromatic rings, *RSC Adv.* 3 (2013) 9185–9188. <https://doi.org/10.1039/c3ra41574k>.
- [222] Y. Zhang, W. Liu, Y. Liu, C. Wang, G. Zhu, W. Song, Directly written DPP-DTT/SrTiO₃ organic/inorganic heterojunctions for anisotropic self-powered photodetectors, *J. Mater. Chem. C.* 9 (2021) 15654–15661. <https://doi.org/10.1039/d1tc03719f>.
- [223] M. Socol, N. Preda, C. Breazu, A. Costas, G. Petre, A. Stanculescu, G. Popescu-pelin, A. Mihailescu, G. Socol, Organic Thin films based on DPP-DTT:C60 blends deposited by MAPLE, *Nanomaterials.* 10 (2020) 2366. <https://doi.org/10.3390/nano10122366>.
- [224] B. Tian, L. Liu, M. Yan, J. Wang, Q. Zhao, N. Zhong, P. Xiang, L. Sun, H. Peng, H. Shen, T. Lin, B. Dkhil, X. Meng, J. Chu, X. Tang, C. Duan, A robust artificial synapse based on organic ferroelectric polymer, *Adv. Electron. Mater.* 5 (2019) 1800600. <https://doi.org/10.1002/aelm.201800600>.
- [225] Y. Chen, G. Liu, C. Wang, W. Zhang, R.-W. Li, L. Wang, Polymer memristor for information storage and neuromorphic applications, *Mater. Horiz.* 1 (2014) 489–506. <https://doi.org/10.1039/c4mh00067f>.
- [226] S.J. Martin, P.D. Grimwood, R.G.M. Morris, Synaptic plasticity and memory: An evaluation of the hypothesis, *Neurosci.* 23 (2000) 60456. <https://doi.org/10.1146/annurev.neuro.23.1.649>.
- [227] L.F. Abbott, S.B. Nelson, Synaptic plasticity: Taming the beast, *Nat. Neurosci.* 3 (2000) 1178–1183. <https://doi.org/10.1038/81453>.
- [228] T. Chang, S.-H. Jo, W. Lu, Short-term memory to long-term memory transition in a nanoscale memristor, *ACS Nano.* 5 (2011) 7669–7676. <https://doi.org/10.1021/nn202983n>.
- [229] Z. He, H. Shen, D. Ye, L. Xiang, W. Zhao, J. Ding, F. Zhang, C. an Di, D. Zhu, An organic

- transistor with light intensity-dependent active photoadaptation, *Nat. Electron.* 4 (2021) 522–529. <https://doi.org/10.1038/s41928-021-00615-8>.
- [230] P.-P. Lu, D.-S. Shang, C.-S. Yang, Y. Sun, An organic synaptic transistor with Nafion electrolyte, *J. Phys. D. Appl. Phys.* 53 (2020) 485102. <https://doi.org/10.1088/1361-6463/abad63>.
- [231] R.S. Zucker, W.G. Regehr, Short-term synaptic plasticity, *Annu. Rev. Physiol.* 64 (2002) 355–405. <https://doi.org/10.1146/annurev.physiol.64.092501.114547>.
- [232] Y. Li, Y. Zhong, J. Zhang, L. Xu, Q. Wang, H. Sun, H. Tong, X. Cheng, X. Miao, Activity-dependent synaptic plasticity of a chalcogenide electronic synapse for neuromorphic systems, *Sci. Rep.* 4 (2014) 4906. <https://doi.org/10.1038/srep04906>.
- [233] R.C. Froemke, Y. Dan, Spike-timing-dependent synaptic modification induced by natural spike trains, *Nature.* 416 (2002) 433–438. <https://doi.org/10.1038/416433a>.
- [234] J. Kolařík, M. Štol, Relaxation behaviour of poly(methacrylic acid) and its copolymers with 2-hydroxyethyl methacrylate, *Polym. J.* 5 (1973) 158–163. <https://doi.org/10.1295/polymj.5.158>.
- [235] T.M. McFarlane, B. Zdyrko, Y. Bandera, D. Worley, O. Klep, M. Jurča, C. Tonkin, S.H. Foulger, J. Vilčáková, P. Sáha, J. Pflieger, Design rules for carbazole derivatized: N -alkyl methacrylate polymeric memristors, *J. Mater. Chem. C.* 6 (2018) 2533–2545. <https://doi.org/10.1039/c7tc05001a>.
- [236] M. Cölle, M. Büchel, D.M. de Leeuw, Switching and filamentary conduction in non-volatile organic memories, *Org. Electron.* 7 (2006) 305–312. <https://doi.org/10.1016/j.orgel.2006.03.014>.
- [237] C.W. Chu, J. Ouyang, J.H. Tseng, Y. Yang, Organic donor-acceptor system exhibiting electrical bistability for use in memory devices, *Adv. Mater.* 17 (2005) 1440–1443. <https://doi.org/10.1002/adma.200500225>.
- [238] W.M.H. Sachtler, G.J.H. Dorgelo, A.A. Holscher, The work function of gold, *Surf. Sci.* 5 (1966) 221–229. [https://doi.org/10.1016/0039-6028\(66\)90083-5](https://doi.org/10.1016/0039-6028(66)90083-5).
- [239] A. Thomas, A.N. Resmi, A. Ganguly, K.B. Jinesh, Programmable electronic synapse and nonvolatile resistive switches using MoS₂ quantum dots, *Sci. Rep.* 10 (2020) 12450. <https://doi.org/10.1038/s41598-020-68822-5>.
- [240] J. Hao, R. Zou, R. Liao, L. Yang, Q. Liao, New method for shallow and deep trap distribution analysis in oil impregnated insulation paper based on the space charge detrapping, *Energies.* 11 (2018) 271–276. <https://doi.org/10.3390/en11020271>.
- [241] S. Yanmei, A. Chunpeng, L. Junguo, L. Lei, W. Dianzhong, B. Xuduo, The influence of thickness on memory characteristic based on nonvolatile tuning behavior in poly(N-vinylcarbazole) films, *Thin Solid Films.* 598 (2016) 293–298. <https://doi.org/10.1016/j.tsf.2015.12.029>.
- [242] T. Uryu, H. Ohkawa, R. Oshima, Synthesis and high hole mobility of isotactic poly(2-N-carbazolyethyl acrylate), *Macromolecules.* 20 (1987) 712–716. <https://doi.org/10.1021/ma00170a002>.
- [243] L.H. Xie, Q.D. Ling, X.Y. Hou, W. Huang, An effective Friedel-Crafts post- functionalization of poly(N-vinylcarbazole) to tune carrier transportation of supramolecular organic semiconductors based on π -stacked polymers for nonvolatile flash memory cell, *J. Am. Chem. Soc.* 130 (2008) 2120–2121. <https://doi.org/10.1021/ja076720o>.
- [244] Y. Wei, D. Gao, L. Li, S. Shang, Memory effect in polymer brushes containing pendant carbazole groups, *Polymer (Guildf).* 52 (2011) 1385–1390. <https://doi.org/10.1016/j.polymer.2011.01.044>.
- [245] J. Vandendriessche, P. Palmans, S. Toppet, N. Boens, F.C. De Sshryver, H. Masuhara, Configurational and conformational aspects in the excimer formation of bis(carbazoles), *J. Am. Chem. Soc.* 106 (1984) 8057–8064. <https://doi.org/10.1021/ja00338a009>.
- [246] G. Safoula, K. Napo, J.C. Bernède, S. Touihri, K. Alimi, Electrical conductivity of halogen doped poly(N-vinylcarbazole) thin films, *Eur. Polym. J.* 37 (2001) 843–849. [https://doi.org/10.1016/S0014-3057\(00\)00185-3](https://doi.org/10.1016/S0014-3057(00)00185-3).
- [247] Q. Chen, B.F. Bory, A. Kiazadeh, P.R.F. Rocha, H.L. Gomes, F. Verbakel, D.M. De Leeuw, S.C.J. Meskers, Opto-electronic characterization of electron traps upon forming polymer oxide memory diodes, *Appl. Phys. Lett.* 99 (2011) 083305. <https://doi.org/10.1063/1.3628301>.
- [248] L. Scalón, A. Leithold Neto, L.O. Araujo, S. Zaioncz, J.B. Floriano, A.G. MacEdo, C.M. Araujo, C.F.N. Marchiori, P.C. Rodrigues, Assessing the donor-acceptor nature and the electrochemical stability of a fluorene-diketopyrrolopyrrole-thiophene-based copolymer, *ACS Appl. Polym. Mater.* 3 (2021) 4223–4233. <https://doi.org/10.1021/acsapm.1c00651>.
- [249] Z. Yi, S. Wang, Y. Liu, Design of high-mobility diketopyrrolopyrrole-Based π -conjugated

- copolymers for organic thin-film transistors, *Adv. Mater.* 27 (2015) 3589–3606. <https://doi.org/10.1002/adma.201500401>.
- [250] J. Li, Y. Zhao, H.S. Tan, Y. Guo, C.A. Di, G. Yu, Y. Liu, M. Lin, S.H. Lim, Y. Zhou, H. Su, B.S. Ong, A stable solution-processed polymer semiconductor with record high-mobility for printed transistors, *Sci. Rep.* 2 (2012) 754. <https://doi.org/10.1038/srep00754>.
- [251] T. Menke, Molecular doping of organic semiconductors – A conductivity and seebeck study, 2013.
- [252] I. Salzmann, G. Heimel, M. Oehzelt, S. Winkler, N. Koch, Molecular electrical doping of organic semiconductors: Fundamental mechanisms and emerging dopant design rules, *Acc. Chem. Res.* 49 (2016) 370–378. <https://doi.org/10.1021/acs.accounts.5b00438>.
- [253] J. Li, I. Duchemin, O.M. Roscioni, P. Friederich, M. Anderson, E. Da Como, G. Kociok-Köhn, W. Wenzel, C. Zannoni, D. Beljonne, X. Blase, G. D’Avino, Host dependence of the electron affinity of molecular dopants, *Mater. Horizons.* 6 (2019) 107–114. <https://doi.org/10.1039/c8mh00921j>.
- [254] H.S. Tan, N. Mathews, T. Cahyadi, F.R. Zhu, S.G. Mhaisalkar, The effect of dielectric constant on device mobilities of high-performance, flexible organic field effect transistors, *Appl. Phys. Lett.* 94 (2009) 10–13. <https://doi.org/10.1063/1.3168523>.
- [255] S. Guo, Z. Wang, X. Chen, L. Li, J. Li, D. Ji, L. Li, W. Hu, Low-voltage polymer-dielectric-based organic field-effect transistors and applications, *Nano Sel.* 3 (2022) 20–38. <https://doi.org/10.1002/nano.202100051>.
- [256] F. Piana, J. Pflieger, R. Jambor, T. Řičica, J.M. Macak, High-k dielectric composites of poly(2-cyanoethyl vinyl ether) and barium titanate for flexible electronics, *J. Appl. Polym. Sci.* 134 (2017) 45236. <https://doi.org/10.1002/app.45236>.
- [257] Q. Zhang, T.S. Kale, E. Plunkett, W. Shi, B.J. Kirby, D.H. Reich, H.E. Katz, Highly contrasting static charging and bias stress effects in pentacene transistors with polystyrene heterostructures incorporating oxidizable N, N'-bis(4-methoxyphenyl)aniline side chains as gate dielectrics, *Macromolecules.* 51 (2018) 6011–6020. <https://doi.org/10.1021/acs.macromol.8b00596>.
- [258] W. Huang, W. Shi, S. Han, J. Yu, Hysteresis mechanism and control in pentacene organic field-effect transistors with polymer dielectric, *AIP Adv.* 3 (2013) 0521221. <https://doi.org/10.1063/1.4807660>.
- [259] M. Egginger, S. Bauer, R. Schwödiauer, H. Neugebauer, N.S. Sariciftci, Current versus gate voltage hysteresis in organic field effect transistors, *Monatsh Chem.* 140 (2009) 735–750. <https://doi.org/10.1007/s00706-009-0149-z>.
- [260] A. Nawaz, I.A. Hümmelgen, Z.A. Lampert, H.F. Haneef, S. Anand, M. Waldrip, O.D. Jurchescu, Tutorial: Organic field-effect transistors: Materials, structure and operation, *J. Appl. Phys.* 124 (2018) 071101. <https://doi.org/10.1063/1.5042255>.
- [261] A. Nawaz, I.A. Hümmelgen, Poly(vinyl alcohol) gate dielectric in organic field-effect transistors, *J. Mater. Sci. Mater. Electron.* 30 (2019) 5299–5326. <https://doi.org/10.1007/s10854-019-00873-5>.
- [262] M.D. Özeren, Á. Pekker, K. Kamarás, B. Botka, Evaluation of surface passivating solvents for single and mixed halide perovskites, *RSC Adv.* 12 (2022) 28853–28861. <https://doi.org/10.1039/d2ra04278a>.
- [263] Y. Yan, L.-B. Huang, Y. Zhou, S.-T. Han, L. Zhou, Q. Sun, J. Zhuang, H. Peng, H. Yan, V.A.L. Roy, Surface decoration on polymeric gate dielectrics for flexible organic field-effect transistors via hydroxylation and subsequent monolayer self-assembly, *ACS Appl. Mater. Interfaces.* 7 (2015) 23464–23471. <https://doi.org/10.1021/acsami.5b05363>.
- [264] G. Han, X. Wang, J. Zhang, G. Zhang, H. Yang, D. Hu, D. Sun, X. Wu, Y. Ye, H. Chen, T. Guo, Interface engineering with double-network dielectric structure for flexible organic thin film transistors, *Org. Electron.* 52 (2018) 213–221. <https://doi.org/10.1016/j.orgel.2017.10.031>.
- [265] C.D. Dimitrakopoulos, P.R.L. Malenfant, Organic thin film transistors for large area electronics, *Adv. Mater.* 14 (2002) 99–117. [https://doi.org/10.1002/1521-4095\(20020116\)14:2<99::aid-adma99>3.0.co;2-9](https://doi.org/10.1002/1521-4095(20020116)14:2<99::aid-adma99>3.0.co;2-9).
- [266] S.H. Kim, W.M. Yun, O.K. Kwon, K. Hong, C. Yang, W.S. Choi, C.E. Park, Hysteresis behaviour of low-voltage organic field-effect transistors employing high dielectric constant polymer gate dielectrics, *J. Phys. D. Appl. Phys.* 43 (2010) 465102. <https://doi.org/10.1088/0022-3727/43/46/465102>.

List of Abbreviations

AI	Artificial intelligence
AC	Alternating current
ANNs	Artificial neural networks
ATR-FTIR	Attenuated total reflectance Fourier-transform infrared
BDS	Broadband dielectric spectroscopy
BE	Bottom electrode
BGBC	Bottom-gate-bottom-contact
BGTC	Bottom-gate-top-contact
CEPVA	Poly(vinylalcohol-co-vinylcyanoethoxy)
CG	Control gate
Ci	Capacitance
CMOS	Complementary metal-oxide-semiconductor
CPU	Central processing unit
CT	Charge transport
D	Diffusion constant
DPP	Diketopyrrolopyrrole
DRAM	Dynamic random-access memory
E_c	Energy level of charge transporting level
E_a	Electron affinity
EPROM	Erasable programmable read-only memory
EEPROM	Electrically erasable programmable read-only memory
EPSC	Excitatory-post-synaptic current
ESA	Excited-state absorption
FG	Floating gate
FETs	Field-effect transistors
FRET	Förster resonance energy transfer
fs	femtosecond
FTIR	Fourier-transform infrared
GB	Gigabyte
GDOS	Gaussian density-of-states
G_{MAX}	Maximum conductance
G_{MIN}	Minimum conductance
GSB	Ground-state bleach
HDA	4,4' - (hexafluoroisopropylidene) diphthalic anhydride
HN	Havriliak-Negami
HR	High resistance
IC	Internal conversion
I_{CL}	Current compliance limit
IT	Information technology
IEEE	Institute of electrical and electronics engineers
I_{DS}	Drain current
IRF	Instrument response function
ISC	Inter-system crossing
ITO	Indium tin oxide
k	Boltzmann constant
LTP	Long-term potentiation
LTD	Long-term depression
LTM	Long-term memory/ memorization
LTF	Long-term forgetting
LR	Low resistance
LUMO	Lowest unoccupied molecular orbital
MIM	Metal-insulator-metal

M _w	Molecular weight
MOSFET	Metal-oxide-semiconductor field-effect transistor
MTR	Multiple trapping and release
N _c	Density of states at the transporting level
Nd:YAG laser	Neodymium-doped yttrium aluminum garnet laser
NDR	Negative differential resistance
NIR	Near-infrared
NMR	Nuclear magnetic resonance
OD	Optical density
OFETs	Organic field-effect transistors
OPVs	Organic photovoltaics
OSC	Organic semiconductors
PCaPMA	Poly(N-(3-(9H-carbazol-9-yl)propyl)methacrylamide)
PDI	Perylene diimide
PET	Polyethylene terephthalate
PETMS	Trimethoxy(2-phenylethyl)silane
PMT	Photomultiplier tube
PMF	Methylated poly(melamine-co-formaldehyde)
PMMA	Poly(methyl methacrylate-co-methyl methacrylate)
PVCa	Polyvinyl carbazole
PVP	Polyvinyl phenol
QCM	Quartz-crystal microbalance
QY	Quantum yield
RFID	Radio-frequency identification
ReRAMs	Resistive random-access memories
R _{ON}	Resistance in ON state
R _{OFF}	Resistance in OFF state
RS	Resistive switching
R-S	Richardson–Schottky
R2R	Roll-to-roll
SAM	Self-assembling monolayers
SCLC	Space charge-limited current
SCLC-F	Space charge-limited current (field-dependent)
SNNs	Spiking neuronal networks
SRAM	Static random-access memory
STM	Short-term memory
STF	Short-term forgetting
STDP	Spike-time-dependent plasticity
STP	Short-term potentiation
T	Temperature
TCSPC	Time-correlated single photon counting
TAS	Transient-absorption spectroscopy
TE	Top electrode
T _{FL}	Trap-field limit
TF	Thin-film
TIPS-pentacene	Tetra(isopropyl)silane substituted pentacene
V _G	Gate voltage
V _{DS}	Drain voltage
V _{th}	Threshold voltage
ω	Angular frequency
μ	Effective mobility
ε _r	Dielectric permittivity layer
ε ₀	Dielectric permittivity in a vacuum
Φ _B	Schottky barrier

List of Figures

Chapter 1: Introduction

Figure 1.1	Photographs of LG's smartphone, 18-inch rollable OLED and EPD displays, and rollable OPVs on a wind turbine tower	3
Figure 1.2	Photograph of OPVs & statistical growth of its working efficiency ...	5
Figure 1.3	Illustration of bond and orbital formation in an ethylene molecule	7
Figure 1.4	Chemical structure of thiophene-diketopyrrolopyrrole (TDPP) derivative indicating a donor (D) and an acceptor (A) moieties and its schematic representation formation of molecular orbitals	8
Figure 1.5	Schematic energy band diagram illustrating charge injection via F-N tunneling, RS thermionic emission, and PF emission structures	9
Figure 1.6	Schematics of DOS filling in the GDOS of the hopping states	10
Figure 1.7	Doping of OSCs with p-type and n-type semiconductor.....	11
Figure 1.8	Energy diagram of OSC containing localized states in band gap	14
Figure 1.9	Jablonski energy diagram illustrating different energy transitions	16
Figure 1.10	Schematic of Arrhenius plots showing relaxation behaviors and Nyquist plot for LCR circuit	20
Figure 1.11	Memristor representation and its pinched hysteresis in the I-V characteristics dependent on excitation frequency	22
Figure 1.12	Schematics of HP memristor model	23
Figure 1.13	Classification of electronic memories and schematics of Floating gate MOSFET and von-Neumann computing architecture	24
Figure 1.14	Schematics of the crossbar memory array and their mapping via matrix multiplication for computing	26
Figure 1.15	I-V curve of ITO PCaPMA Al device at different conduction regions & schematic of voltage-induced conformational change in molecule	28
Figure 1.16	Formation of ion-radical species and charge transfer complexes controlling the layer conductivity	29
Figure 1.17	Schematic representation of the formation and rupture of filaments ...	30
Figure 1.18	Schematics of OFET's BGBC and BGTC structure	32

Chapter 2: Materials and Method

Figure 2.1	Molecular structure of small molecules	35
Figure 2.2	Molecular structure of semiconducting polymers	36
Figure 2.3	Chemical structures dielectrics, crosslinkers, and silane	37
Figure 2.4	Schematic of various methods of thin film preparation	38
Figure 2.5	Schematics of a memristive device	39

Figure 2.6	Structures of OFETs	40
Figure 2.7	Schematic of SEC device and its measurement setup	41
Figure 2.8	Schematic illustration of pump-probe setup for TAS measurement	43
Figure 2.9	Schematic of TA spectrum	43

Chapter 3: Results and Discussion

Figure 3.1	Chemical structure of the TDPP derivatives	50
Figure 3.2	Steady-state absorption and fluorescence emission spectra and its decay in TDPP derivatives.....	51
Figure 3.3	Spectral evolution of R-BOX and R-TCN in ultrafast time regime	53
Figure 3.4	Comparison of temperature-dependence difference in steady-state absorption spectra and TA spectrum at longer time delay in TDPP thin film	55
Figure 3.5	Schematic of PCaPMA synthesis	58
Figure 3.6	UV-vis absorption and emission spectra of PCaPMA and PVCa.	59
Figure 3.7	Cyclic voltammogram (CV) of PCaPMA, PVCa, DPP-DTT, and PDI films cast on the ITO glass and the energy levels diagram of respective materials & electrodes used for device fabrication	60
Figure 3.8	Current-voltage (I–V) characteristics of ITO PCaPMA Al, ITO PVCa Al and ITO DPP-DTT: PDI composite Al device	61
Figure 3.9	The memory behaviour of ITO PCaPMA Al device with dynamic WRER, persistence, and volatility test.	62
Figure 3.10	Pulse-schematic and I–V characteristics in ITO PCaPMA Al, and ITO DPP-DTT: PDI composite Al device studied for synaptic weight modulation	63
Figure 3.11	Progression of STP and LTP in ITPO PCaPMA Al device	65
Figure 3.12	Illustration of potentiation/depression modulation via PPF/D & STDP	67
Figure 3.13	Dielectric impedance spectra of the loss modulus, M'' of PCaPMA showing α -, β - and γ - relaxations and Nyquist plot	69
Figure 3.14	Linear fitting of an I–V curve and photodetrapping of trapped charges in ITO PCaPMA Al device	71
Figure 3.15	UV-Vis-NIR spectra <i>in-situ</i> voltage spectra in ITO PCaPMA electrolyte ITO & ITO DPP:DTT electrolyte ITO	72
Figure 3.16	Output and transfer characteristics of pure DPP-DTT and pure PDI ...	73
Figure 3.17	OFET characteristics with PVP dielectrics cast by different methods ...	78
Figure 3.18	Optical image of printed OFET and its output characteristics	79
Figure 3.19	Crosslinkers-dependent hysteresis in OFET characteristics	80
Figure 3.20	Effect of dielectric surface passivation in OFET using PETMS	81

List of publications

1. **Y.R. Panthi**, A. Pandey, A. Šturcová, D. Výprachtický, S.H. Foulger, J. Pflieger, *Emulating Synaptic Plasticity with Poly[N-(3-(9H-carbazol-9-yl)propyl)methacrylamide] Memristor*, Mater. Adv. 5 (2024) 6388–6398 (2024).
<https://doi.org/10.1039/d4ma00399c>.
2. **Y.R. Panthi**, A. Thottappali, P. Horáková, L. Kubáč, *Photophysics of benzoxazole and dicyano functionalised diketopyrrolopyrrole derivatives: Insights into ultrafast processes and the triplet state*, ChemPhysChem. 25 (2024) e202300872.
<https://doi.org/doi.org/10.1002/cphc.202300872>
3. A. Pandey, A. Chernyshev, **Y.R. Panthi**, A. Sturcov, O. Kocková, S.H. Foulger, J., Vohlidal, J. Pflieger, *Synapse-mimicking memristors based on 3, 6-di(tpy)-9- phenylcarbazole unimer and its copolymer with cobalt(II) ions*, Polymers (Basel). 16 (2024) 542.
<https://doi.org/10.3390/polym16040542>
4. **Y.R. Panthi**, J. Pflieger, D. Výprachtický, A. Pandey, M.A. Thottappali, I. Šeděnková, M. Konefał, S.H. Foulger, *Rewritable resistive memory effect in poly[N-(3-(9H-carbazol-9-yl)propyl)-methacrylamide] memristor*, J. Mater. Chem. C. 11 (2023) 17093–17105.
<https://doi.org/10.1039/d3tc03394e>.
5. M. Guesmi, V. Kanclíř, T. Thoř, O. Taboubi, I. Šeděnková, **Y.R. Panthi**, J. Pflieger, K. Židek, I. Sed, Y.R. Panthi, J. Pflieger, K. Židek, *Study of defects in fused silica via a Franck-Condon analysis*, J. Lumin. 257 (2023) 119668.
<https://doi.org/10.1016/j.jlumin.2023.119668>
6. D. Rais, P. Toman, U. Acharya, **Y.R. Panthi**, M. Menšík, A. Zhigunov, M.A. Thottappali, J. Pflieger, M. Vala, A. Marková, S. Střiteský, M. Weiter, M. Cigánek, J. Krajčovič, K. Pauk, A. Imramovský, A. Zaykov, J. Michl, *Singlet Fission in thin solid films of bis(thienyl)diketopyrrolopyrroles*, Chempluschem. 1 (2020) 2689–2703.
<https://doi.org/10.1002/cplu.202000623>
7. P. Bober, Y. Li, U. Acharya, **Y.R. Panthi**, J. Pflieger, P. Humpolíček, M. Trchová, J. Stejskal, *Acid Blue dyes in polypyrrole synthesis: The control of polymer morphology at the nanoscale in the promotion of high conductivity and the reduction of cytotoxicity*, Synth. Met. 237 (2018) 40–49.
<https://doi.org/10.1016/j.synthmet.2018.01.010>

UŽITNÝ VZOR

J. Pflieger; **Y.R. Panthi**, Y.; B. Paruzel; L. Kubáč; J. Černý; *Přepisovatelný elektronický rezistivní paměťový element*, CZ 32526 U1, 2019.

List of contributions to international conferences

1. Panthi, Y. R., Pandey, A., Výprachtický, D., Pflieger, J., *Resistive memory effect and synapse-mimicking functionality of poly[N-(3-(9H-carbazol-9-yl)propyl) methacrylamide] memristor*, Poster, Summer School and Workshop on Organic Electronics and Neuromorphic Systems. Tarragona, Spain, 17.-21.6.2024
2. Panthi, Y. R., Pflieger, J., Pandey, A., Horáková, P. *Electronic memory effect and synaptic plasticity on diketopyrrolopyrrole-thiophene-based thin films*, poster 16th International Conference on Organic Electronics (ICOE2023), Madrid, Spain, 3.-7.7.2023
3. Panthi, Y. R., Pandey, A., Paruzel, B., Kubáč, L., Pflieger, J., *Electronic memory effect and synaptic plasticity in thin films of diketopyrrolopyrrole-thiophene-based polymer doped with organic acceptor*, poster, 11th International Conference on Nanostructured Polymers and Nanocomposites (ECNP), s.89, Lodz University of Technology, Lodž, Poland, 28.-31.8.2023.
4. Panthi, Y. R., Pflieger, J., Výprachtický, D., Pandey, A., Thottappali, M., Šeděnková, I. *Memristive behavior of polymethacrylamide with carbazole side groups*, Poster, European Polymer Federation (EPF) OPEL-Tu123, European Polymer Congress, Prague, Czech Republic, 26.6.-1.7.2022,
5. Panthi, Y. R., Pflieger, J., Výprachtický, D., Rais, D., Thottappali, M., Pandey, A., Foulger S., H. *Rewritable electrical memory effect in poly[N-(3-(9H-carbazole-9-yl) methacrylamide]*, Poster, s. 29, Annual Student Conference, Week of Doctoral Students (WDS), Charles University, Faculty of Mathematics and Physics., Prague, CR, 15.-17.6.2021 (online)
6. Panthi, Y. R., Pflieger, J., Paruzel, B., *Electronic memory based on conjugated polymers molecularly doped with organic acceptors* Oral, s. 81 Polymers for Sustainable Global Development (POLY-CHAR 2019)". Nepal Polymer Institute Kathmandu, Nepál, 19.-23.5.2019,
7. Panthi, Y. R., Pflieger, J., Paruzel, B. *Resistive random-access memory based on conjugated polymers molecularly doped with organic acceptors*, Oral, L-11, Workshop "Career in Polymers XI", Institute of Macromolecular Chemistry, CAS, Prague, CR, 28.-29.6.2019
8. Panthi, Y. R., Pflieger, J., Paruzel, B., Acharya, U., Šlouf, M., Piana, F., *Influence of polymer dielectrics on OFET performance*, Oral, L-7 Career in Polymers IX, Institute of Macromolecular Chemistry CAS, Prague, CR, 28.-29.6.2017



Lodz University
of Technology



Springer Open

30.08.2023, Lodz

YOUNG SCIENTISTS' AWARD

The Scientific Committee of the 11th ECNP International Conference on Nanostructured Polymers and Nanocomposites presents **2nd place** of the Young Scientists' Award for the best poster communication to

Yadu Ram Panthi

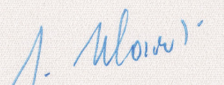
Institute of Macromolecular Chemistry CAS, Prague, Czech Republic

for the work entitled:

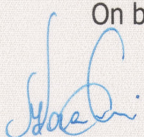
*Electronic Memory Effect and Synaptic Plasticity in Thin Films
of Diketopyrrolopyrrole-thiophene-based Polymer Doped
with Organic Acceptor*

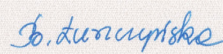
The financial award is sponsored by *Functional Composite Materials (FCM)*
Springer Nature Switzerland AG.

On behalf of the Scientific Committee


Prof. Jacek Ulański

On behalf of the Organizing Committee


Prof. Marcin Kozanecki


Prof. Beata Łuszczynska

11th ECNP International Conference on Nanostructured Polymers and Nanocomposites
August 28-31, 2023, Lodz, Poland

Attachments

A.1

Y.R. Panthi, A. Thottappali, P. Horáková, L. Kubáč, *Photophysics of benzoxazole and dicyano functionalised diketopyrrolopyrrole derivatives : Insights into ultrafast processes and the triplet state*, ChemPhysChem. 25 (2024) e202300872.
<https://doi.org/doi.org/10.1002/cphc.202300872>

A.2

Y.R. Panthi, J. Pflieger, D. Výprachtický, A. Pandey, M.A. Thottappali, I. Šeděnková, M. Konefał, S.H. Foulger, *Rewritable resistive memory effect in poly[N-(3-(9H-carbazol-9-yl)propyl)-methacrylamide] memristor*, J. Mater. Chem. C. 11 (2023) 17093–17105.
<https://doi.org/10.1039/d3tc03394e>.

A.3

Y.R. Panthi, A. Pandey, A. Šturcová, D. Výprachtický, S.H. Foulger, J. Pflieger, *Emulating Synaptic Plasticity with Poly[N-(3-(9H-carbazol-9-yl)propyl)methacrylamide] Memristor*, Mater. Adv. (2024). Mater. Adv. 5 (2024) 6388–6398 (2024).
<https://doi.org/10.1039/d4ma00399c>.

A.4

Pflieger, J.; **Panthi, Y. R.**; Paruzel, B.; Kubáč, L.; Černý, J.; Přepisovatelný elektronický rezistivní paměťový element, UŽITNÝ VZOR CZ 32526 U1, 2019.

